



**Alcino Rafael Leal
Barbosa**

**Desenvolvimento de um modelo computacional do
crânio humano
Development of a computational model of the
human skull**



**Alcino Rafael Leal
Barbosa**

**Desenvolvimento de um modelo computacional do
crânio humano
Development of a computational model of the
human skull**

Dissertação apresentada à Universidade de Aveiro para cumprimento dos requisitos necessários à obtenção do grau de Mestre em Engenharia Mecânica, realizada sob orientação científica de Fábio António Oliveira Fernandes, investigador na Universidade de Aveiro e de Ricardo José Alves de Sousa, Professor Auxiliar com Agregação do Departamento de Engenharia Mecânica da Universidade de Aveiro.

Esta dissertação teve o apoio dos projetos:

UIDB/00481/2020 e UIDP/00481/2020 -
FCT - Fundação para a Ciência e a
Tecnologia; e

CENTRO-01-0145-FEDER-022083 -
Programa Operacional Regional do
Centro (Centro2020), através do
Portugal 2020 e do Fundo Europeu de
Desenvolvimento Regional

O júri / The jury

Presidente / President

Prof. Doutor Joaquim Alexandre Mendes de Pinho da Cruz
Professor Auxiliar da Universidade de Aveiro

Vogais / Committee

Prof. Doutor Renato Manuel Natal Jorge
Professor Catedrático da Faculdade de Engenharia da Universidade do Porto

Doutor Fábio António Oliveira Fernandes
Investigador Júnior da Universidade de Aveiro (orientador)

Agradecimentos / Acknowledgements

O alcançar desta etapa na minha vida não teria sido possível sem a colaboração, auxílio, carinho e dedicação por parte de várias pessoas ao longo de todo o percurso da minha formação. Por esta mesma razão, não quero deixar passar esta oportunidade para agradecer a todos aqueles que, direta ou indiretamente, contribuíram para o meu sucesso e a minha chegada até aqui. Agradeço a todos os professores que tanto me ensinaram no decorrer da minha Licenciatura e também do Mestrado, nomeadamente ao Doutor Fábio António Oliveira Fernandes e ao Doutor Ricardo José Alves de Sousa. Agradeço também ao Professor Mariuz Ptak da Politechnika Wroclawska por ter disponibilizado o acesso ao Hypermesh, programa indispensável para a realização deste trabalho.

E por último, agradeço a todos os meus familiares e amigos que me admiram, me apoiam e acreditaram sempre nas minhas capacidades. Por serem as pessoas fantásticas que são, o meu muito obrigado.

palavras-chave

Método dos Elementos Finitos, Crânio, Trabecular, Cortical, Suturas.

resumo

A principal causa de mortalidade de crianças e adultos, entre 5 e 29 anos, são os acidentes de trânsito. Para melhor compreender os mecanismos que os causam ou desenvolver mecanismos de prevenção e detecção, foram desenvolvidos vários modelos de elementos finitos da cabeça humana, como o YEAHM desenvolvido por membros da Universidade de Aveiro. Por esse motivo, o objetivo desta dissertação é a melhoria do YEAHM, em particular o crânio, com diferenciação entre diferentes tipos de tecidos ósseos, com base na geometria externa original, mas segmentando-a com suturas, diploë e osso cortical, e validá-lo como ferramenta para prever fraturas cranianas. Diversas validações são realizadas, comparando os resultados da simulação com os resultados experimentais disponíveis na literatura em três níveis: i) validação local do material; ii) Lesão contusa isolada do crânio; iii) Estruturas crânio-intracranianas acopladas submetidas a três impactos em diferentes velocidades, simulando quedas. Acelerações, forças de impacto e padrões de fratura são usados para validar o modelo do crânio.

keywords

Finite Element Method, Skull, Trabecular, Cortical, Sutures.

abstract

The leading cause of mortality for both children and adults, between the ages of 5 and 29 years old, is road traffic accidents. To better understand the mechanisms that cause them or to develop prevention and detection mechanisms, several finite element models of the human head have been developed, with the YEAHM developed by members of the university of Aveiro. For this reason, the purpose of this dissertation is to improve the YEAHM, in particular the skull, with differentiation between different types of bone tissues, based on the original external geometry, but segmenting it with sutures, diploë and cortical bone, and validating it as a tool to predict cranial fractures. Several validations are performed, comparing the results of the simulation with the experimental results available in the literature at three levels: i) local validation of the material; ii) Isolated skull blunt trauma; iii) Coupled cranio-intracranial structures subjected to three impacts at different speeds, simulating falls. Accelerations, impact forces and fracture patterns are used to validate the skull model.

Contents

List of Tables	iii
List of Figures	v
Acronyms	ix
Symbology.....	xi
Introduction.....	1
1.1 Motivation	1
1.2 Objectives	2
1.3 Reading Guide.....	2
State of the Art	3
2.1 Human Head Anatomy.....	3
2.1.1 Meninges	3
2.1.2 Bridging Veins.....	4
2.1.3 Cerebrospinal Fluid.....	5
2.1.4 Brain	5
2.1.5 Skull	6
2.2 Head Injuries.....	14
2.2.1 Skull Injuries	15
2.2.2 Brain Injuries	17
2.2.3 Head Injury Criteria.....	19
2.3 Skull fracture mechanics	20
2.3.1 Sandwich structures and cranial bone	20
2.3.2 Fractures and Cranial Sutures	21
2.4 Finite elements head models (FEHM)	23
2.4.1 History of finite elements head models.....	23
2.4.2 Comparison between different types of solid elements.....	29
2.4.3 Experimental investigations of the human skull bone behaviour	30
2.4.4 Mesh Density: Computation cost vs Mesh convergence	37
2.4.5 YEt Another Head Model (YEAHM).....	38
Methodology.....	41
3.1 Geometrical Model of the Skull	41
3.2 Material Modelling of the Skull.....	48
3.2.1 Trabecular bone material model	48

3.2.2	Quasi-brittle material model (cortical and sutures)	49
3.3	Validation methodology	51
3.3.1	Validation of the Trabecular Bone.....	51
3.3.2	Validation of Skull.....	53
3.4	YEAHM model + New Skull model.....	55
<i>Simulations and Results.....</i>		57
4.1	Validation and discussion.....	57
4.1.1	Trabecular experiments – local material validation	57
4.1.2	Skull Vertex impact simulation results.....	61
4.1.3	Skull lateral impact simulation	63
4.1.4	Huang’s experiment - Fracture simulation.....	69
<i>Conclusions and Future Works</i>		71
5.1	Conclusion.....	71
5.1.1	Future Works.....	71
<i>References</i>		73

List of Tables

Table 1. Mechanical properties of cranial sutures.....	9
Table 2. Data for suture average width in the five sutures [19].....	9
Table 3. Mechanical properties of cortical and trabecular bone taken from the literature.	10
Table 4. Pearson correlation (r) and p-value between trabecular thickness and age, height or weight [37].	11
Table 5. Pearson correlation between trabecular layer thickness and total skull thickness [37]. ...	12
Table 6. AIS-classified head and face injuries. Adapted from Schmitt [40].....	16
Table 7. Tolerance limits for skull fracture. Adapted from Tse et al. [14] and Schmitt [40].	20
Table 8. Skull model differences between FE head models.	28
Table 9. Skull material model differences for different FE head models.	28
Table 10. Computation and real-time results for frictionless contact and compressive load tests, performed by Tadepalli et al. [100].	30
Table 11. Experimental Data Base from Katholieke Universiteit Leuven [102].....	32
Table 12. Description of the twelve unembalmed human cadavers [67].	35
Table 13. Physical data of the 12 unembalmed cadaver heads with respective mean values [67].	36
Table 14. Comparison of computation cost and convergence of different mesh densities [101]. ...	37
Table 15. Properties of the material used to model the brain. Adapted from Fernandes [3].	39
Table 16. Properties of the material used to model the CSF. Adapted from Fernandes [3].	39
Table 17. Properties of the material used to model the skull. Adapted from Fernandes [3].	39
Table 18. Properties of the material used to model the bridge veins / superior sagittal sinus. Adapted from Costa [104].	39
Table 19. The elastic behaviour values chosen to both cortical bone and cranial sutures.....	49
Table 20. Micro CT study results from Boruah et.al [93].	52
Table 21. Model thickness measurements in different skull locations.....	58

List of Figures

Figure 1. Major injuries from work-related injuries in Europe [2].....	1
Figure 2. Illustration of the main layers of the meninges [6].	3
Figure 3. Representation of cerebrospinal fluid and its normal circulation [11].	5
Figure 4. Representation of the various constituent parts of the brain [13].	6
Figure 5. Representation of the various bones of the human skull [16].....	7
Figure 6. Representation of the viscerocranium/facial bones of the human head [17].	7
Figure 7. Illustration of the main cranial sutures [20].....	8
Figure 8. CT cross-section of the frontal bone of a 56-year-old male skull [28].....	10
Figure 9. Variants of the various types of models used by Chamrad et al. [36].....	12
Figure 10. Average bone changes for the whole skull for females (top) and males (bottom) from age 20 to 100 years. Thickness values represent the averaged predicted OT, IT, and full thicknesses from the regression equations. OT=outer table; IT=inner table [28].....	14
Figure 11. Representation of different types of possible head injuries.....	15
Figure 12. Three types of facial fractures classified according to LeFort. Adapted from Schmitt [40].	16
Figure 13. Illustration of the different cranial fractures that may arise (linear and depressed) [43].	17
Figure 14. Coup and counter coup contusions. Adapted from Kleiven [50].	18
Figure 15. Possible focal brain injuries. Adapted from Porth et al. [52].	19
Figure 16. Layered beam element and deformations - a: layered beam element; b: membrane deformation; c: bending deformation; d: shearing deformation [76].	21
Figure 17. Distribution of maximum principal stress and fracture pattern on outer and inner layers for cranial sutures with Young's modulus within the range of 50–500 MPa and for a skull without cranial sutures (at 5 ms after the impact) [21].	22
Figure 18. Representation of a finite element model. Adapted from [77]	23
Figure 19. Finite element head model developed by Hosey [69]. A: sagittal section; B: Coronal section [14].	24
Figure 20. Various versions of WSUHIM. (A) 1 st version by Ruan et al. (1993); enhanced versions by (B) Zhou et al. (1995) followed by (C) Zhang et al. (2001); (D) latest version has been reviewed by King et al. (2003) [14].	25
Figure 21. The Strasbourg University Finite Element Head Model (SUFEHM). Adapted from [93].	26
Figure 22. Kungliga Tekniska Högskolan (KTH) FEHM. (A) skull model; (B) brain model with 11 pairs of bridge veins; (C) sagittal cross-section of the head and neck model; (D) anatomical structures modelled [14].	26
Figure 23. The SIMon head model. (A) Coronal cross-sectional view; (B) View illustrating the model without internal brain tissues; (C) Revised version of SIMon FEHM [14].	27
Figure 24. Illustration of the brain injury model at the University of Dublin (UCDBTM). (A) the skull; (B) the brain; (C) partial cut-view illustrating the intracranial content [14].	27
Figure 25. Results and recommendations outlined schematically, adapted from Wang et al. [99].	29
Figure 26. Frontal impact test setup by Verschueren et al. [92].	31

Figure 27. Left Image: Specimen no. 8 showing typical linear fracture pattern after being impacted at intermediate velocity; Right Image: Specimen no. 17 showing multiple fractures after being impacted at high velocity [102].	31
Figure 28. Instrumented impactor from Huang et al. experiment [101].	33
Figure 29. Strain gage locations relative to the impact site from Huang et al. [101] experiment.	33
Figure 30. Comparisons of depressed skull fracture pattern from the 35m/s experiment and the corresponding FE simulation [101].	34
Figure 31. Comparisons of fracture pattern from a cross-section view of the FE model with a CT image in the corresponding position (axial plane) [101].	35
Figure 32. Schematics of the specimen orientation in the fixation device and the external load (shown by dark arrow) applied, (a) Vertex, (b) 45° right lateral (parietal), (c) 78° right lateral (temporal), (d) 45° rearward (occipital), and (e) 45° forward (frontal) regions [67].	36
Figure 33. Comparison of head response for different mesh densities and peak impact force [101].	37
Figure 34. Illustration of the method used to create the YEAHM model. Adapted from Fernandes [3].	38
Figure 35. Constitution of the YEAHM model. On the left shows a section showing the skull (blue), CSF (red) and brain (green) and on the right shows the bridge veins (yellow) with the brain.	39
Figure 36. Pressure gradients obtained while using C3D4 elements (left) and C3D10M elements (right). Adapted from Fernandes et al. [3].	40
Figure 37. Skull model surface (STL version).	42
Figure 38. Separation of the original model into surfaces. On the left, the external surface of the skull and on the right, the internal surface of the skull.	42
Figure 39. Transformation of the STL meshes into solid iges in FreeCAD software. On the left figures the meshes can be seen and on the right figures their respective solid parts.	43
Figure 40. Obtaining the trabecular bone from Solidworks. On the left, an axial sectional view shows various parts of the assembly and on the right, the visualization of the trabecular bone.	43
Figure 41. Visualization of all the filled holes to create the part of the final trabecular bone.	44
Figure 42. Visualization of the initial component created in HyperMesh for the trabecular bone.	45
Figure 43. Sagittal, coronal and axial cross-sections of the model with 1.5 mm cortical layers and with a core of trabecular bone.	46
Figure 44. Problematic elements found. On the left, the elements with bad Jacobian highlighted in white and on the right, the elements with intersections highlighted in blue.	46
Figure 45. Reference images took from the 3D atlas utilized to create the cranial sutures [107].	47
Figure 46. Visualization of the final complete model in Abaqus with trabecular bone, cortical bone (1.5 mm) and cranial sutures.	48
Figure 47. Stress-strain behaviour of trabecular bone under compression loading [108].	48
Figure 48. Definition of A: brittle, B: quasi-brittle, and C: ductile behaviour - strain softening and strain hardening under uniaxial tensile loading [29].	49
Figure 49. Post-failure stress-strain curve for both cortical and sutures tissues.	50
Figure 50. Shear retention model values for both cortical and sutures tissues.	50
Figure 51. Harvest locations marked on the skull (1 up to 10). Also shown are the reference features and location measurement scheme [108].	51
Figure 52. Cores being drilled out of the calvarium using a vertical drill [108].	52

Figure 53. A cylindrical-shaped sandwich sample with trabecular bone in the core, and cortical bone in the tables (inner table on top) [108].	52
Figure 54. Skull core compression test setup [108].	53
Figure 55. Schematics of the specimen orientation in the fixation device and the external load (shown by dark arrow) [67].	54
Figure 56. Schematic of Yoganandan's et.al [109] test setup.	55
Figure 57. Representation of the Skull + Brain+ CSF + BVs & SSS final assembly. Cut views in the 3 main planes, from left to right: sagittal, frontal and transverse planes.	56
Figure 58. Locations of the samples in the FEHM, numbered and highlighted in grey.	58
Figure 59. Element type and mesh density results with the 3 comparable location results.	59
Figure 60. Differences between a model with damage, without damage and with unloading.	60
Figure 61. Visualization of the boundary conditions of the simulation from Yoganandan's [67] study. Left figure: sagittal view. Right figure: frontal view.	61
Figure 62. Comparison between the 1 mm and 1.5 mm cortical thickness results and the experiment, using the same material model.	62
Figure 63. Comparison between element types for the cortical bone and sutures.	62
Figure 64. Results of the simulation compared with the experiment results.	63
Figure 65. Stress-strain curve of the neoprene's compression uniaxial test [112].	63
Figure 66. Contra-Lateral experiment acceleration response expressed as mean \pm one standard deviation at 6 m/s impact velocity with simulation results.	64
Figure 67. Anterior experiment acceleration response expressed as mean \pm one standard deviation at 6 m/s impact velocity with simulation results.	64
Figure 68. Posterior experiment acceleration response expressed as mean \pm one standard deviation at 6 m/s impact velocity with simulation results.	65
Figure 69. Contra-Lateral experiment acceleration response expressed as mean \pm one standard deviation at 4.9 m/s impact velocity with simulation results.	65
Figure 70. Anterior experiment acceleration response expressed as mean \pm one standard deviation at 4.9 m/s impact velocity with simulation results.	66
Figure 71. Posterior experiment acceleration response expressed as mean \pm one standard deviation at 4.9 m/s impact velocity with simulation results.	66
Figure 72. Contra-Lateral experiment acceleration response expressed as mean \pm one standard deviation at 3.5 m/s impact velocity with simulation results.	67
Figure 73. Anterior experiment acceleration response expressed as mean \pm one standard deviation at 3.5 m/s impact velocity with simulation results.	67
Figure 74. Posterior experiment acceleration response expressed as mean \pm one standard deviation at 3.5 m/s impact velocity with simulation results.	68
Figure 75. Comparison between the anterior experiment acceleration results, and the C3D8R and C3D8I results.	68
Figure 76. Comparison between the posterior experiment acceleration results, and the C3D8R and C3D8I results.	69
Figure 77. Huang's simulation assembly on Abaqus.	70
Figure 78. Comparisons of depressed skull fracture pattern obtained with YEAHM and in both Huang's experiment and simulation.	70

Acronyms

BV	Bridging Veins
CAD	Computer-Aided Design
CSF	Cerebrospinal Fluid
CT	Computed Tomography
DAI	Diffuse Axonal Injury
EDH	Epidural Hematoma
FEHM	Finite Element Head Model
FEM	Finite Element Model
GSI	Gadd Severity Index
HIC	Head Injury Criterion
HIP	Head Impact Power
ICH	Intracranial Hematoma
ICP	Intracranial Pressure
IGES	Initial Graphics Exchange Specification
KTH	Kungliga Tekniska Högskolan
PMHS	Post-mortem human subjects
PWr	Politechnika Wroclawska
SDH	Subdural Hematoma
SIMon	Simulated Injury Monitor
SSS	Superior Sagittal Sinus
STL	Stereolithography
TBI	Traumatic Brain Injury
UCDBTM	University College Dublin Brain Trauma Model
WSTC	Wayne State Tolerance Curve
WHO	World Health Organization
WSUHIM	Wayne State University Head Injury Model
YEAHM	YEt Another Head Model

Symbology

ρ	Specific mass
E	Young's modulus
r	Pearson's correlation coefficient
p	p-value for Pearson correction
ν	Poisson's ratio
μ	Shear modulus
g	Relaxation's coefficient
τ	Relaxation's time
C_{10}, C_{01}	Material parameters
D_1, α_1	Material parameters
K	Bulk modulus
fb_0/fc_0	Biaxial Load Ratio
T_u	Ultimate Shear Stress
σ_t^I	Post Failure Stress
G_c	Cracked shear modulus
ω	Shear retention factor
ϵ_{nn}^{ck}	Strain after cracking
ϵ	Green-Lagrangian Strain
σ	Cauchy Stress

Chapter 1

Introduction

1.1 Motivation

One of the leading causes of mortality in the world is road traffic accidents, creating approximately 1.35 million deaths, the leading cause in children and young people between 5 and 29 years old [1]. More than half of these deaths are suffered by vulnerable users (such as pedestrians, cyclists and motorcyclists), in particular those living in developing countries. From those, head injuries are also one of the main injuries caused by work accidents, as can be seen in Figure 1.

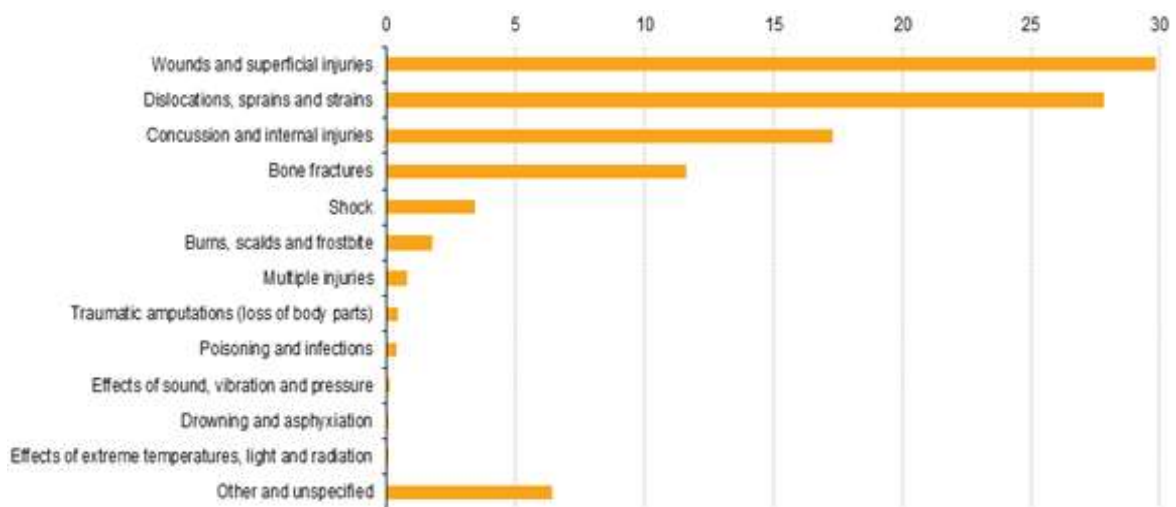


Figure 1. Major injuries from work-related injuries in Europe [2].

In order to reduce the risk of fatal injuries, it is therefore important to study the head thoroughly, as it contains a vital organ, the brain. One way to study this subject, without harming humans or animals or destroying materials and equipment, resorts to simulations through the finite element method. which consists of a numerical procedure to determine approximate solutions of physical or mathematical problems. The use of the method requires a precise representation of complex geometries and inclusion of material properties for these same geometries.

This work goes on to further detail an existing model, the YEt Another Head Model (YEAHM), developed and validated by Fernandes et al. [3]. Since this model does not differentiate the types of bones belonging to the skull, modelling it as a linear-elastic homogenous solid, the present work will focus on a subdivision of the skull bone tissue to make the model more realistic and then validate the model with this new configuration.

1.2 Objectives

The work elaborated in this dissertation aims, as the main objective, to create and integrate a detailed 3D model of the skull, resulting in a more accurate Finite Element Head Model (FEHM) for additional impact simulations and a better understanding of how injuries occur during an accident or a sports-related impact. For this purpose, the main objective was subdivided as follows:

- Creation of a geometric skull model that distinguishes between cortical bone tissue, trabecular bone tissue and cranial sutures;
- Modelling of skull bone materials using existing models, with the implementation of damage models;
- Validation of the new model developed at different levels: i) local material validation; ii) isolated skull blunt trauma; Coupled skull-intracranial structures subjected to different impact energies, simulating falls and impacts by objects (comparing accelerations, impact forces and fracture patterns).

1.3 Reading Guide

The dissertation is organized in five chapters. In order to help the reader moving through the content of each chapter, a short description can be read here.

- [Chapter 1](#) – Introduction
This chapter is intended to present the reader with a short introduction of the topic addressed in this dissertation. Summarising the reasons that led to the accomplishment of this work, the objectives and also its structure.
- [Chapter 2](#) – State of the Art
This chapter presents the current, most relevant literature to the topics in question, such as the anatomy of the adult head and the mechanical properties and craniometry of the human adult skull.
- [Chapter 3](#) – Methodology
After studying the literature previously presented, this chapter presents the methods used for the creation and validation of the model.
- [Chapter 4](#) – Simulations and Results
In this chapter, the reader will find the results obtained in the simulations and their comparison and discussion with the experimental results found in the literature.
- [Chapter 5](#) – Conclusion and Future Works
At last, this chapter presents the conclusions found, possible limitations and future work.

Chapter 2

State of the Art

2.1 Human Head Anatomy

The head is one of the most important, if not the most important, parts of the body, because in it lies the brain that controls all body movement and because it controls 4 of the 5 senses humans have: sight, smell, taste and hearing. Therefore, head injuries are a very important health problem. To better protect the head in various events such as accidents, sports or falls, the mechanisms and tolerances underlying the injury need to be investigated. Worldwide, many investigations have been conducted using cadaver heads, animal heads, physical head models and in vitro models. These experiments, together with the development of computational techniques, subsequently led to the development of numerical head models [4].

With this state of the art, it is intended to describe the anatomy of the adult human head and to identify the types of existing lesions. Moreover, it is intended from previous studies to identify the criteria that allowed the quantification of these same lesions.

2.1.1 Meninges

The brain, like the spinal cord, is surrounded by 3 layers of membranes: a hard outer layer called the dura mater, a delicate intermediate layer called the arachnoid, and an inner layer firmly attached to the brain surface called the pia mater [5]. Because arachnoid follows the contours of the dura mater and the pia mater follows the contours of the brain surface, a space is formed between these two layers called the subarachnoid space, this space contains cerebrospinal fluid (CSF) and blood vessels.

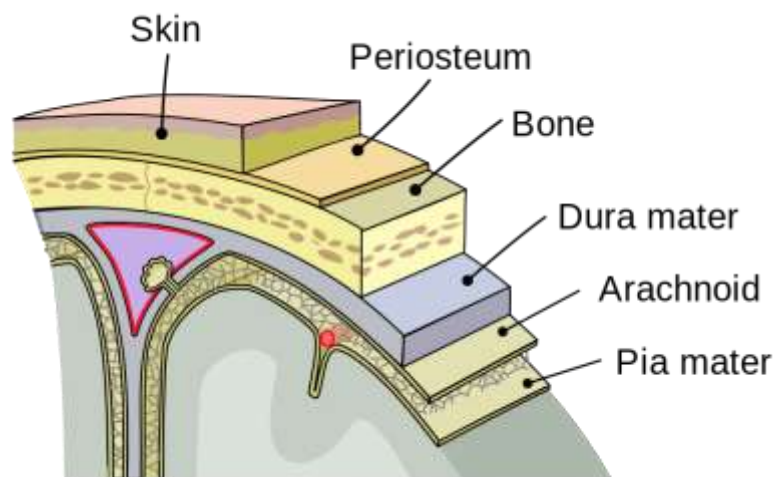


Figure 2. Illustration of the main layers of the meninges [6].

2.1.1.1 Dura mater

The dura mater is the thickest, toughest and the most peripheral membrane of the meninges, it is directly attached to the skull surface and the inner surface of the vertebral canal walls (where the spinal cord is located). It has a fibrous structure and usually, with age, the thickness of the dura mater changes from 0.3 to 0.8mm [7].

2.1.1.2 Arachnoid

The arachnoid has its name because it is separate and at the same time attached to the pia mater. It is the thin, elastic middle meningeal membrane, the structure of which forms a net consisting of trabeculae similar to that of a "cobweb". Pia mater and arachnoid meninges are often described as a single membrane under the name pia-arachnoid. Both the membrane that is supported by the trabeculae and the trabeculae themselves are made up of delicate collagen fibres accompanied by some elastic fibres.

2.1.1.3 Pia mater

The pia mater is the most internal membrane of the meninges, closely adhering to the surface of the brain and spinal cord, whose contours and depressions follow to the bottom of the brain grooves. Its main function is to give resistance to the nervous organs since the nervous tissue is of very soft consistency. The pia mater follows the vessels that penetrate the nervous tissue from the subarachnoid space, forming the outer wall of the perivascular spaces. These perivascular spaces contain cerebrospinal fluid.

2.1.2 Bridging Veins

The bridging veins (BV) have the function of draining venous blood from the cerebral cortex to the superior sagittal sinus (SSS) through the subdural space. Oka et al. [8] found that the direction of flow through the bridge veins contains high variability. Brockmann et al. [9] defined five categories that prove this same variability:

- Along the flow direction of the SSS (anterograde);
- Perpendicular;
- Opposite to the direction of flow of the SSS (retrograde);
- Hooked, that is, changes direction shortly before entering the sinus;
- Gaps, for example, enlarged venous spaces.

Han et al. [10] found out that due to the various flow orientations in the SSS, movement of the brain relatively to the skull will result in tensile and shear loads in some bridge veins, allowing them to possibly rupture and leading to the appearance of lesions.

2.1.3 Cerebrospinal Fluid

Cerebrospinal fluid, also called CSF, is a colourless fluid that fills and surrounds the brain and spinal cord providing a mechanical barrier against shock. It is located at the level of the central nervous system, where it occupies the subarachnoid space, the ependymal canal and the cerebral ventricles. Cerebrospinal fluid supports the brain and provides lubrication between the surrounding bones and the brain and spinal cord. The fluid helps maintain pressure within the skull at a constant level. An increase in blood or brain tissue volume results in a corresponding decrease in fluid. On the other hand, if there is a decrease in the volume of matter within the skull, such as in brain atrophies, the CSF compensates with an increase in its volume. The fluid also carries metabolic waste, antibodies and chemicals products away from the brain and spinal cord into the bloodstream. CSF is slightly alkaline and consists of about 99 % water.

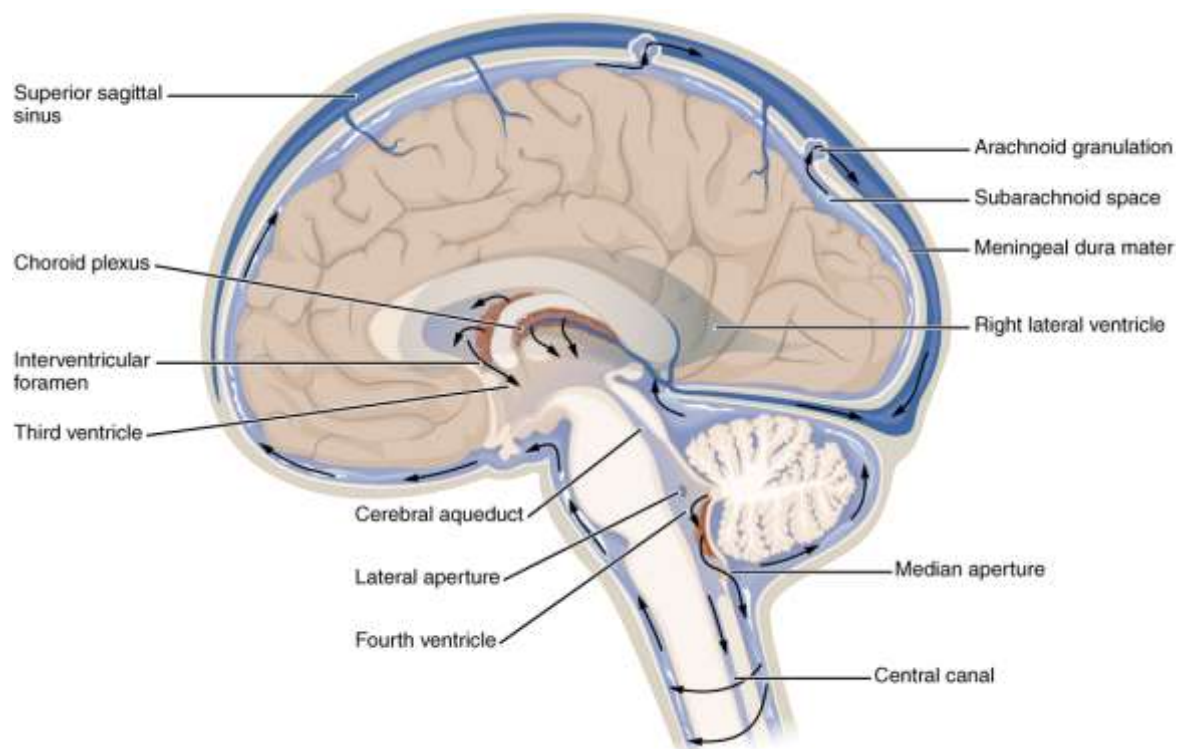


Figure 3. Representation of cerebrospinal fluid and its normal circulation [11].

2.1.4 Brain

The human head of a medium-sized adult weighs about 4.50 - 5.00 kg, of which only the brain constitutes approximately one-third of its mass (1.60 kg in men; 1.45 kg in women) [12]. The human brain is often called the most important organ in the head and with the spinal cord makes up the central nervous system. The brain is comfortably seated in the rigid skull and bathed in cerebrospinal fluid. Because the density of the brain and cerebrospinal fluid is very similar, the brain does not sink or float in the cerebrospinal fluid [12].

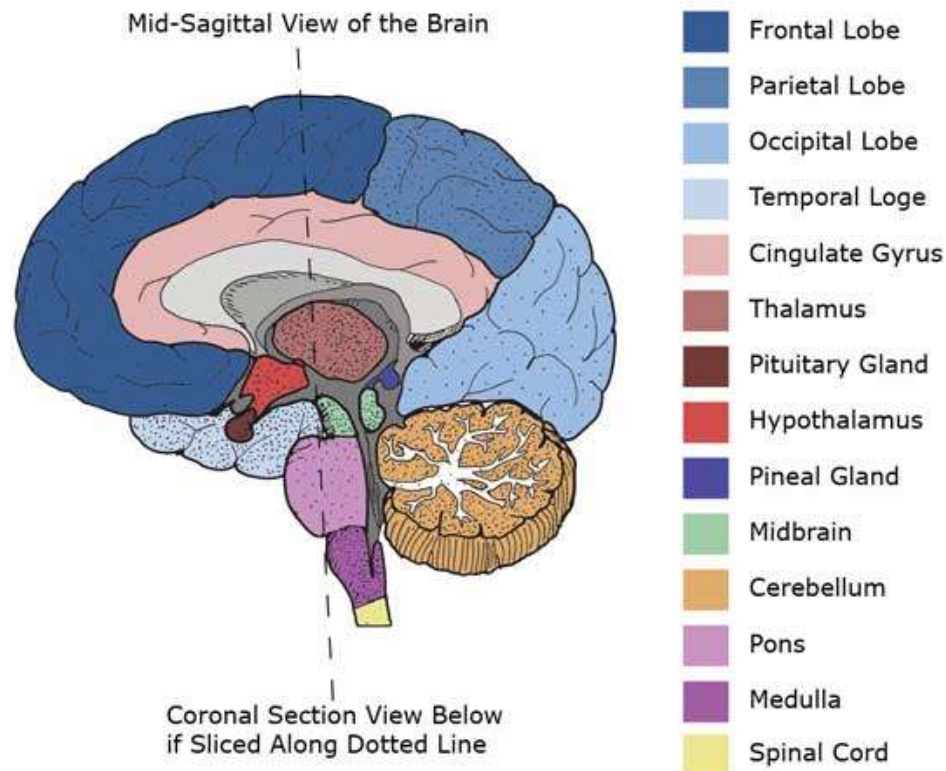


Figure 4. Representation of the various constituent parts of the brain [13].

This organ can be divided into the cerebrum, brainstem and cerebellum. The outer region of the hemispheres, the cerebral cortex, is the grey matter, consisting of cortical layers of neurons. Each hemisphere can be divided into four lobes (frontal, parietal, temporal and occipital). The brainstem grasps and leaves the brain at the beginning of the midbrain. The brainstem includes the midbrain, the bridge, and the medulla. Behind the brain stem is the cerebellum. The cerebellum is divided into an anterior lobe, a posterior lobe and the nodular floccule lobe. The cerebellum rests on the back of the cranial cavity, lying under the occipital lobes [5].

2.1.5 Skull

The human skull consists of approximately 22 isolated bones (8 cranial bones and 14 facial bones), which are mostly connected by ossified joints, the so-called sutures. The cranial bones consist of unpaired frontal, occipital, ethmoidal and sphenoid bones, as well as paired parietal and temporal bones, while facial bones are composed of unpaired vomer and mandible, as well as paired lacrimal, nasal, palatine, inferior, maxillary pairs and zygomatic bones [14]. The most important bones to simulate fracture and consequent damage to the brain and/or veins are the cranial bones since their main function is to protect all organs within the cranial cavity from external impacts. Several studies have revealed that a lot of mechanical responses are influenced by the type and arrangement of bone tissue [15].

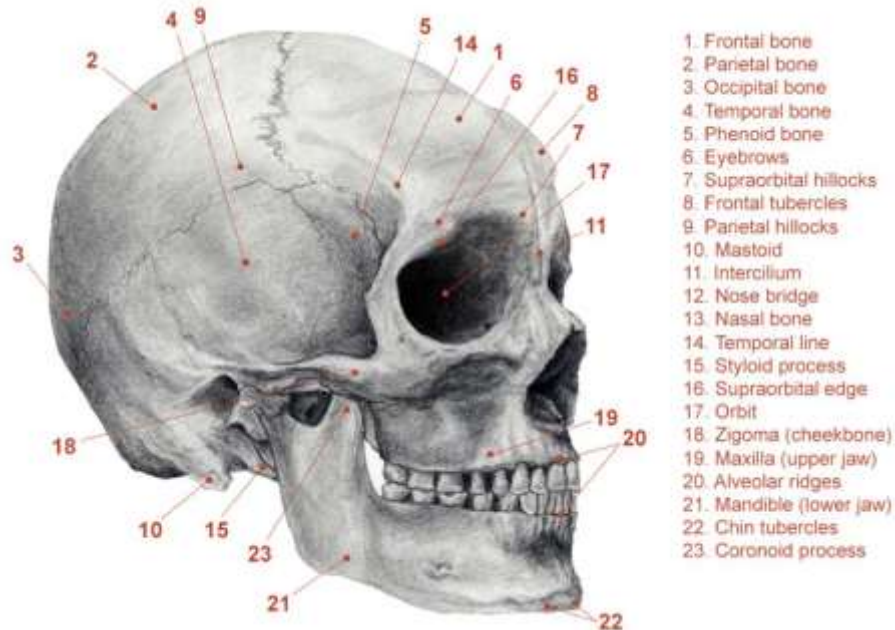


Figure 5. Representation of the various bones of the human skull [16].

2.1.5.1 Facial Bones

Viscerocranium or facial bones support the soft tissues of the face. The viscerocranium consists of 14 individual bones that fuse during the individual human growth. However, the hyoid bone, the ethmoid bone and the sphenoid bones (Figure 6) are sometimes included in the viscerocranium.

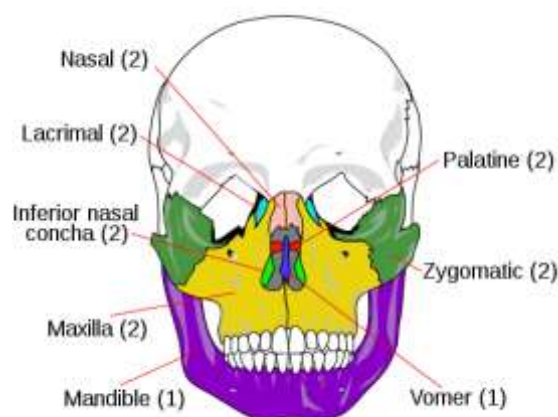


Figure 6. Representation of the viscerocranium/facial bones of the human head [17].

The two zygomatic bones form the cheeks and contribute to the orbits and articulate with the frontal, temporal, maxillary and sphenoid bones. The two lacrimal bones form the medial wall of the orbit and articulate with the frontal, ethmoid, inferior, and maxillary nasal shells. The lacrimal

bones are the two smallest bones located on the face. The two thin nasal bones located on the midline of the face merge to form the nose bridge and also articulate with the frontal, ethmoid and maxillary bones. The inferior nasal conchae are located within the nasal cavity. The bones of the jaw fuse into the midline and form the upper jaw. The palatine bones fuse into the midline to form the palatine, located at the back of the nasal cavity that forms the roof of the mouth and the floor of the orbit. The joint between the jaw and the temporal bones of the skull forms the only un-straped joint in the skull.

Facial bone resembles a sandwich structure containing cancellous and cortical layers except in the nasal bone where the cancellous layer is not well developed. The cortical layer of the bone in the face other than the mandible is generally thinner than the inner and outer tables of the skull, says Zhang et al. [18]. A study performed by Asmaa Maloul [19] revealed that cortical bone thickness for the facial bones averaged from 0.35 (nasal bone) to 2.48mm (zygomatic arch).

2.1.5.2 Sutures

Sutures allow bones to move during the birth and growth process. They act as flexible joints which allow the bones to grow evenly as the brain grows and the skull expands. The result is a symmetrical-shaped head. Some sutures extend to the forehead, while others extend to the sides and back of the skull.

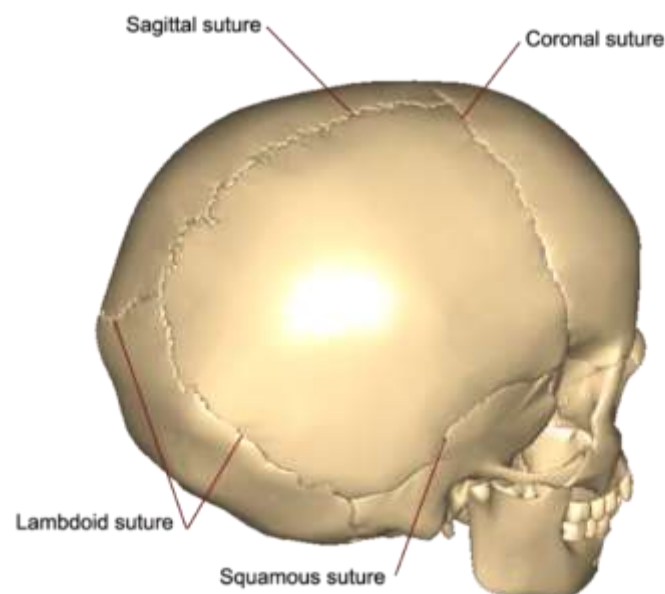


Figure 7. Illustration of the main cranial sutures [20].

All skull bones are connected by suture joints – the cranial sutures are composed mainly of collagen. There are 13 sutures in the human skull, 4 of which are considered the main ones: the coronal suture, the sagittal suture, the squamous suture and the lambdoid suture, as shown in Figure 7. The literature lacks a consensus on the mechanical properties of cranial sutures. This is due to their

different spatial distribution of collagen fibres, which results in different geometries and mechanical properties [21] and also because these properties vary a lot with the age of the specimen. Table 1 shows a resume of the different properties for cranial sutures found in the literature.

ρ (t/mm ³)	E (MPa)	ν (-)	Age of specimens	Reference
-	3638	-	71 years	[22]
-	1000	-	6 years	[23]
2.10E-09	50	0.3	Infants	[24]
	100			[25]
	200			[26] [27]
	300			[27]
	400			
	500			

Table 1. Mechanical properties of cranial sutures.

A study performed by Asmaa Maloul [19], where the zygomaticotemporal (19x13x3mm), zygomaticomaxillary (6x13x8mm), frontozygomatic (6x13x8mm), coronal (1x14x7mm) and sagittal (16x17x5mm) sutures were extracted from a preserved cadaveric head (seventh decade of age), revealed that sutures width averaged from 0.286 to 0.443mm, as shown in Table 2.

Suture	Suture average width (mm)
Sagittal	0.367
Coronal	0.286
Frontozygomatic	0.443
Zygomaticotemporal	0.240
Zygomaticomaxillary	0.361

Table 2. Data for suture average width in the five sutures [19].

2.1.5.3 Bone tissue and its properties

Bone is a calcified tissue that forms the majority of the skeleton. There are two types of bones, compact (cortical) and spongy (trabecular or diaphyse), as shown by Figure 8. Compact bone is a dense bone that forms the outer layer of all bones and surrounds the cancellous bone. There are also 5 types of bones classified by their shape. Long bones are tubular (femur), short bones are cuboid (wrist bones) and flat bones consisting of two compact bones separated by a cancellous bone (skull), irregularly shaped bones, and sesamoid bones that develop in tendons [5].

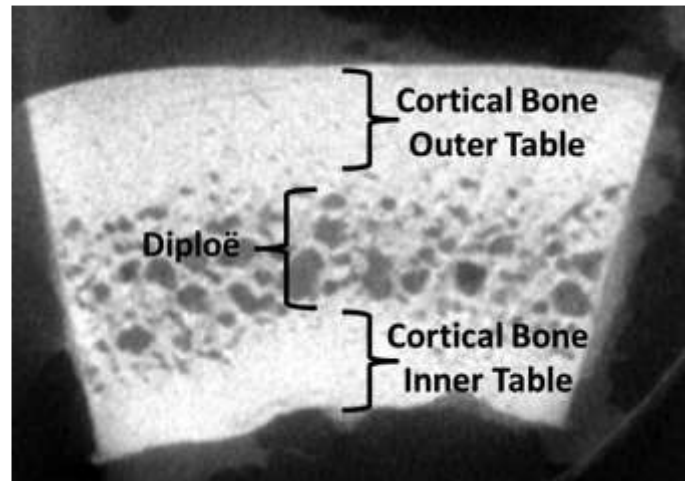


Figure 8. CT cross-section of the frontal bone of a 56-year-old male skull [28].

Under displacement-controlled uniaxial stress, the initial fracture behaviours are classified into three types: brittle, ductile, and a combination of both called quasi-brittle. The brittle behaviour is characterized by the complete loss of tension when the material reaches its limit of elastic deformation. The quasi-brittle behaviour shows the gradual decrease of stress after yield stress or elastic limit of the material [29]. Ductile behaviour shows a gradual increase in tension until the breaking point of the material. Bone tissue is not a completely rigid material; It is neither ductile nor fragile, but a combination of both, quasi-brittle. The mineral part is more unstable/brittle and the organic part (collagen) is more ductile [30].

In order to be able to differentiate the structure of the skull bone tissue and to obtain more reliable and realistic simulations, an extensive bibliographic review of the mechanical properties of the cortical and trabecular bones is presented in Table 3.

Tissue	ρ (kg/m ³)	E (MPa)	ν	Reference
Cortical	1800	15000	0.21	[31]
	1900	15000	0.21	[32] [33]
	2100	6000	0.25	[18]
	2000	15000	0.22	[34]
	1900	15000	0.21	[35]
Trabecular	1500	4500	0.01	[31]
	1500	4600	0.05	[32] [33]
	1000	560	0.3	[18]
	1300	1000	0.24	[34]
	1500	4665	0.05	[35]

Table 3. Mechanical properties of cortical and trabecular bone taken from the literature.

2.1.5.4 Skull's dimensions

The skull is made up of trabecular and cortical bones. In order to create the most reliable model possible, the thickness of both bones was studied. In the case of volume models with a homogeneous distribution of material properties, the role of trabecular bone should be considered for the solution regarding the exchange between the difficulty of constructing the model and the demand for reliable results [36].

Studies done by Lynnerup [37] revealed that statistically speaking, neither trabecular skull thickness nor total skull thickness is significantly associated with an individual's gender, weight or height, this results were found with the use of both the Peraon correlation and p-value. In these studies, 64 individuals were biopsied at the Forensic Medicine at the University of Copenhagen, 43 men (age range 16 – 90 years old) and 21 women (age range 23 - 84 years old). No statistically significant differences were found between men and women for trabecular thickness, except for frontal bone biopsies where men have significantly greater trabecular thickness. There was no correlation between trabecular thickness and age, height or weight, as shown in Table 4. The Pearson correlation coefficient is used to measure the strength of a linear association between two variables, where the value $r = 1$ means a perfect positive correlation and the value $r = -1$ means a perfect negataive correlation. The p-value or probability value is the probability of obtaining test results at least as extreme as the results actually observed during the test, assuming that the null hypothesis,a default position that there is no relationship between two measured phenomena or no association among groups, is correct. Researchers investigating a hypothesized relationship will set a p-value in advance of the empirical study. Usually, values of either 0.01 or 0.05 are used. If the data from the study results in a p-value of less than that specified in advance, the researcher will claim that their study is significant and it enables them to reject the null hypothesis and conclude that a relationship really exists [38].

		Age		Height		Weight	
		r	p-value	r	p-value	r	p-value
Frontal	male	0.207	1.000	-0.172	1.000	-0.062	1.000
	female	0.254	1.000	0.187	1.000	0.270	1.000
Occipital	male	0.293	0.470	-0.280	0.556	-0.132	1.000
	female	0.398	0.610	-0.107	1.000	-0.209	1.000
Right Euryon	male	0.062	1.000	-0.062	1.000	-0.018	1.000
	female	0.265	1.000	-0.222	1.000	-0.221	1.000
Left Euryon	male	0.117	1.000	-0.030	1.000	-0.082	1.000
	female	0.233	1.000	-0.233	1.000	-0.175	1.000

Table 4. Pearson correlation (r) and p-value between trabecular thickness and age, height or weight [37].

The most important finding in this study was the existence of a statistically significant correlation between trabecular layer thickness and total skull thickness, which can be seen in Table 5. As several correlations approach 1 and the total skull thickness only depends on the cortical and trabecular thickness, if only one constant thickness is used for the cortical and the total skull

thickness depends only on the trabecular thickness it can minimise the difficulty of constructing the skull, even though it does not fully represent reality.

	Male		Female	
	r	p-value	r	p-value
Frontal trab. Vs total	0.759	0.000	0.729	0.038
Occipital trab. Vs total	0.584	0.008	0.771	0.013
Right euryon trab. Vs total	0.915	0.000	0.845	0.001
Left euryon trab. Vs total	0.871	0.000	0.451	1.000

Table 5. Pearson correlation between trabecular layer thickness and total skull thickness [37].

A study made by Chamrad et al. [36], tried to bring together different computational models of skulls, often used in literature, so that they could analyse and compare them. In that study they analysed 4 types of models illustrated by Figure 9.:

- a shell model (C), created only from the outer surface (consisting only of cortical bone tissue) with a constant thickness of 10mm;
- a solid element model (A) (consisting only of cortical bone tissue);
- a solid element model (B) including cortical and trabecular bone tissue;
- two models (D) that combine shell cortical bone elements and solid trabecular bone elements (one of which is 1mm (D1) thick and the other 2mm (D2) thick);

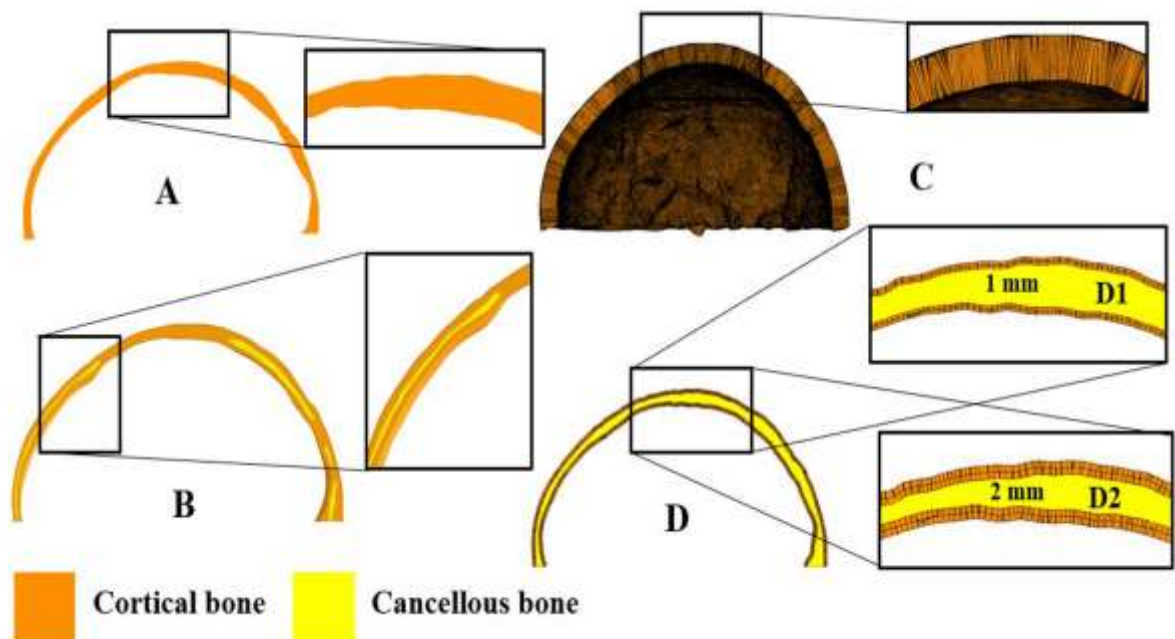


Figure 9. Variants of the various types of models used by Chamrad et al. [36].

Of these different types of models Chamrad et al. [36] observed that from the point of view of model creation, computational models A and C took the same amount of time. Both models D (D1 and D2) took longer to create than models A due to the nature of the FE meshes. The longest modelling process was associated with computational model B because it consisted of two volumes, which were segmented separately but took into account cancellous bone geometry and material properties. Chamrad et al. [36] also found that solid models (A1, A2 and B) were used very frequently throughout the literature.

In the literature, it was found that in studies focused on mechanical interactions with the skull all of the referred models were used, except model C. Model C is the most rigid resulting in the values of the analysed parameters being very far from reality. Model A is geometrically closer to reality because its thickness is not constant, like model C, but since it does not consider trabecular bone it also gives very rigid results. On the other hand, models D1 and D2 consist of cortical bone tissue in shell elements with solid trabecular bone tissue within the entire skull bone, which is far from reality as well [36].

Model D with 2mm thickness of cortical tissue (D2) has been used in many studies, but Chamrad et al. [36] observed that the thickness of cortical bone tissue is smaller than that value, favouring the use of model D1 instead of model D2.

This leads to conclude, based on this study, that to reconcile the time required for the creation of the model and the fidelity to its reality, the geometric model to be created that best fits this work goals combines both model B and model D. Instead of segmenting 2 volumes (B) a single volume representing the cancellous bone would be done followed by an extrusion of elements (D) forming a layer of solid cortical bone elements with a constant thickness.

Another study performed by Lillie et al. [28], where a total of 123 clinical head computer tomography (CT) scans were collected from the Wake Forest Baptist Health Picture Archiving and Communication System (PACS) Radiology database where ages of the subjects scanned ranged from 20 to 99 years with approximately one scan collected per year increment for both males (60 scans) and females (63 scans) revealed interesting data regarding the thickness of both cortical and trabecular bones. As can be seen in Figure 10, the optimal thickness to use for both cortical layers would be around 1mm and 2mm.

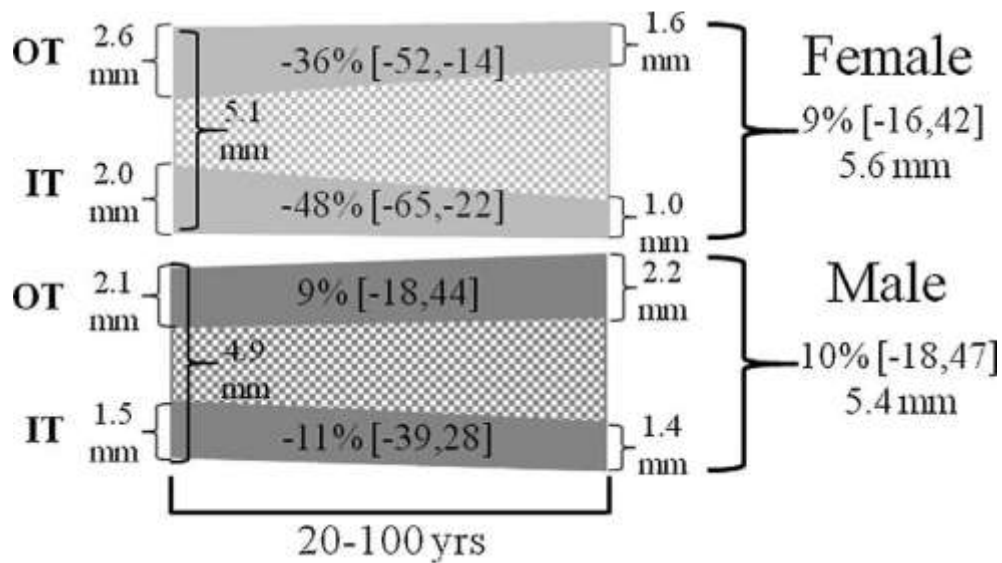


Figure 10. Average bone changes for the whole skull for females (top) and males (bottom) from age 20 to 100 years. Thickness values represent the averaged predicted OT, IT, and full thicknesses from the regression equations. OT=outer table; IT=inner table [28].

2.2 Head Injuries

After an accident, various types of injuries can occur and affect the patient's life, especially those that affect the brain. Currently, major efforts are being made to study the mechanisms of injury in order to better predict and prevent them. The general motivation for this type of study is that brain injuries cause a high mortality rate, as mentioned in Chapter 1 of this dissertation.

In the medical literature, there are two types of head injury-related terminologies that are used interchangeably: "Head injury" and "Brain injury" [39]. Given that brain damage can occur without skull fracture, in this dissertation the term "Brain Injury" or TBI (Traumatic brain injury) will be used as a subgroup of "Head Injuries".

The World Health Organization [1] defines two groups for the diagnosis of injuries. One for skull fractures called extracranial injuries and one for brain injuries called intracranial injuries. As the name suggests, extracranial lesions are those that occur outside the skull and affect bones and facial structures such as the nose and ears, with skull fractures being the most common. As for intracranial injuries, they affect the structures located inside the skull where there is a variety of possible brain damage, such as concussions, bruises and haemorrhages. All intracranial injuries fall into the TBI category, which groups the damage caused by high-energy mechanical loads such as impacts, explosions, and sudden accelerations or decelerations that directly affect the brain [14].

Based on their occurrence, head injuries can be classified as primary injuries that result from the initial trauma and where bruises and lacerations are inserted; and as secondary injuries that are generated due to complications or evolution of the initial injuries and may lead to altered cerebral blood flow, insufficient intracranial oxygen known as hypoxia, infections, intracranial haemorrhages, ischemia (insufficient blood flow) and increased intracranial pressure (ICP) [14].

There is yet another classification of head trauma focused on the severity of the injury and where two groups can be identified as followed: penetrating TBIs are those with open injuries and closed TBIs that occur when the skull and dura remain intact but there is some damage sustained through the brain [14].

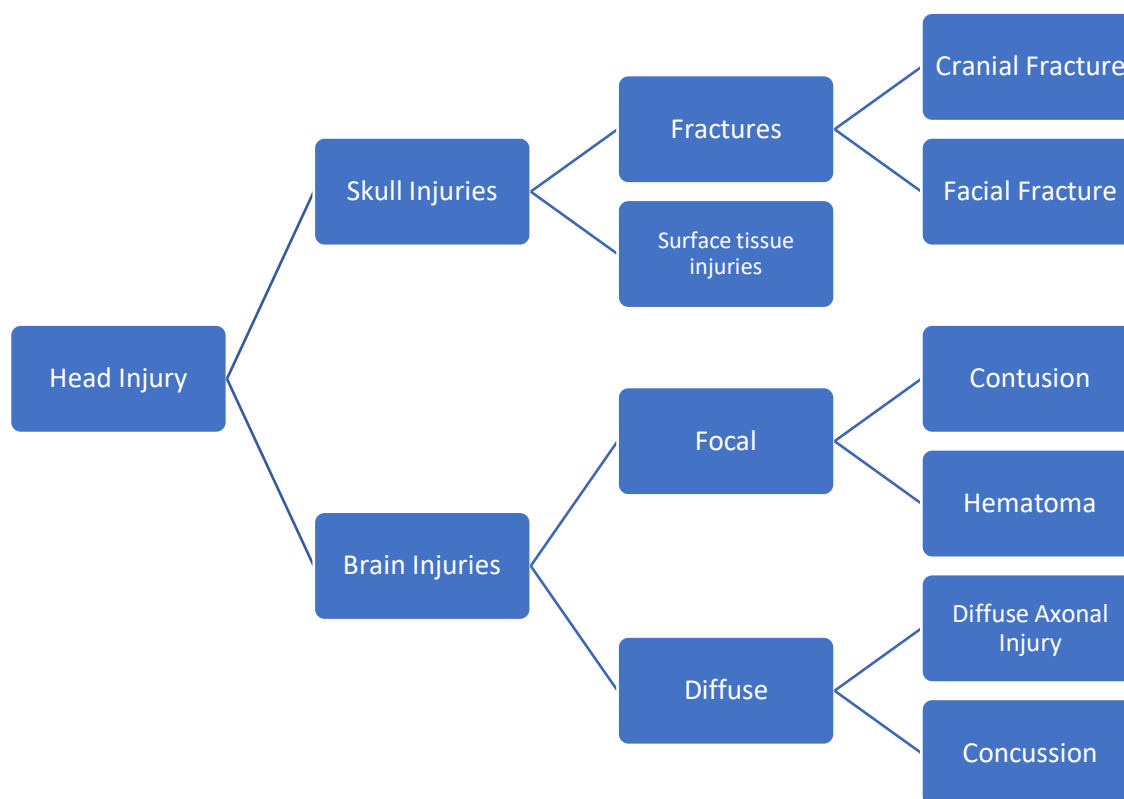


Figure 11. Representation of different types of possible head injuries.

2.2.1 Skull Injuries

2.2.1.1 Facial Fractures

Fractures to the face and mouth usually include fractures of the nose (nasal), cheekbones (zygoma), involve the eyes (orbit) and upper (maxilla) and lower jaws (mandible). They are rated with the Abbreviated Injury Scale (AIS) which is an anatomical-based coding system created by the Association for the Advancement of Automotive Medicine to classify and describe the severity of injuries, which grades from 1 to 6 according to their severity, as shown by Table 6 and Figure 12.

AIS code	Description
1	Scalp: abrasion, superficial laceration Face: nose fracture
2	Scalp: major avulsion Vault fracture: simple, undisplaced Mandible fracture: open, displaced Maxilla fracture: LeFort I and II

3	Basilar fracture Maxilla fracture: LeFort III Total scalp loss Single contusion cerebellum
4	Vault fracture: complex, open with torn dura, exposed or loss of brain tissue, small epidural or subdural hematoma
5	Major penetration injury (>2cm) Brain stem compression Large epidural or subdural hematoma Diffuse axonal injury (DAI) with coma >24 hours
6	Massive destruction of both cranium and brain (crush injury)

Table 6. AIS-classified head and face injuries. Adapted from Schmitt [40]

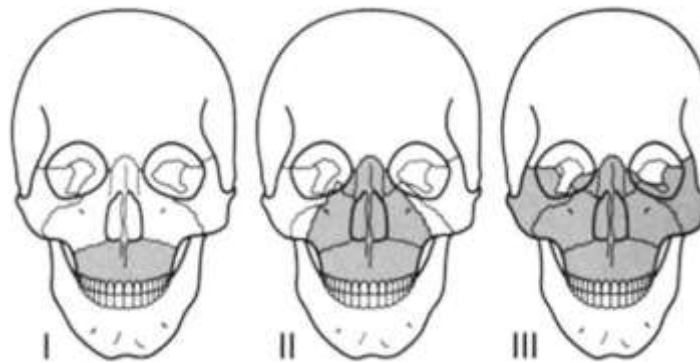


Figure 12. Three types of facial fractures classified according to LeFort. Adapted from Schmitt [40].

2.2.1.2 Cranial Fractures

A cranial fracture occurs when cranial bone breaks. There are many types of cranial fractures, but only one major cause: an impact or a blow to the head that is strong enough to break the bone. The type of cranial fracture depends on the force of the blow, the location of the impact on the skull, and the shape of the object that impacts the head. It has been observed that some patients with cranial fractures did not show evidence of brain damage, which leads to the assumption that the impact energy is dissipated by the fracture and skull bones, protecting the brain from injury [41]. Despite this fact, the incidence of intracranial hematomas was higher among patients with cranial fractures [42]. A cranial fracture can be divided into these main types:

- **Closed fracture:** Also called a simple fracture, the skin that covers the fracture area is not broken or cut.
- **Open fracture:** Also known as a compound fracture, an open fracture occurs when the skin is broken and the bone emerges.
- **Depressed fracture:** refers to a fracture that causes the skull to retract or extend into the brain cavity.
- **Basal fracture:** occurs on the floor of the skull: the areas around the eyes, ears, nose or upper neck near the spine.

- **Linear fracture:** straight-line fracture in the skull bone.

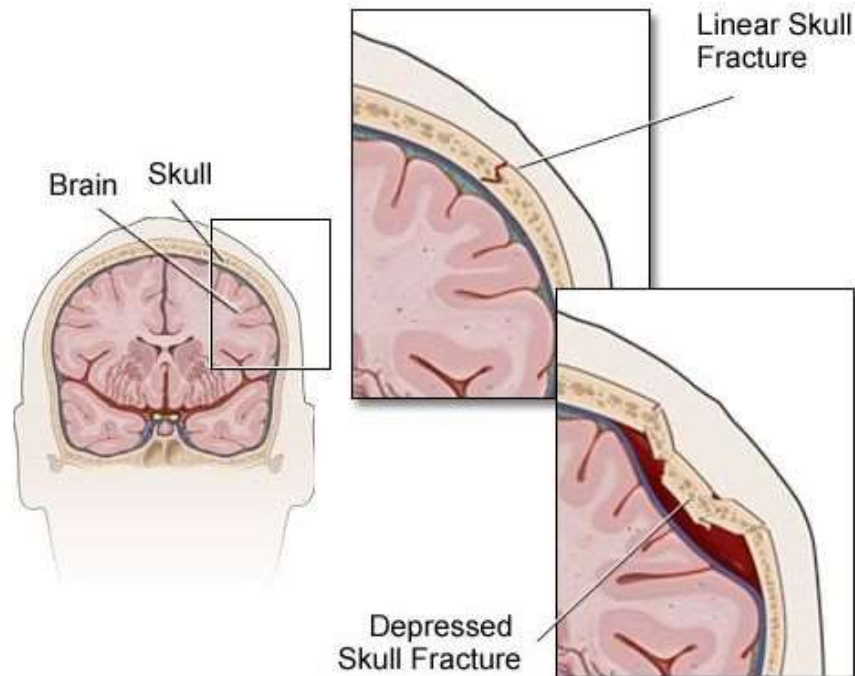


Figure 13. Illustration of the different cranial fractures that may arise (linear and depressed) [43].

2.2.2 Brain Injuries

2.2.2.1 Focal Brain Injuries

As the name suggests, focal brain injuries affect a specific area of the brain and can occur due to direct brain contact with skull fragments or relative movement between the brain and the skull. This movement can be caused by a linear or rotational acceleration of the skull and damage occurs when the brain comes into contact with the irregular geometry of the skull's internal surface, especially in the frontal and temporal areas [44]. These are the types of injuries considered to be the most dangerous that can occur in an accident because in all deaths associated with head injuries, two-thirds are linked to focal brain injuries [45]. Focal brain injuries can be characterized as:

- **Contusion:** results from local movement of brain tissue within the skull [46] and may also occur at the site of depressed cranial fractures [47]. There are usually two distinct types of contusions: blow and backstroke. In coup injuries, the injury occurs at the impact site, while in the countercoup, the injury occurs at the opposite site of the impact, as shown in Figure 14. Coups and countercoups are contact injuries [48] [49], caused by compressive forces or tensile forces.

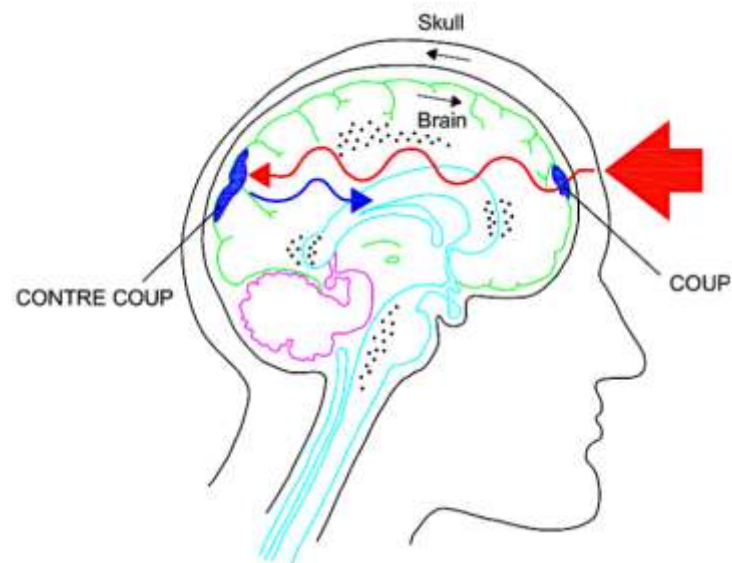


Figure 14. Coup and counter coup contusions. Adapted from Kleiven [50].

- **Hematoma:** there are mainly 3 types of hematomas: epidural (EDH), subdural (SDH) and intracerebral (ICH).
 - EDH is caused by trauma or a skull fracture that causes ruptures of the meningeal arteries and removes the dura from bone rather than actual brain damage [45]. The temporoparietal regions represent the highest percentage (73%) of coagulated EDH, followed by the anterior cranial fossa protecting the frontal lobe (11%) and the sagittal regions located along the with cerebral scythe (9%) [51].
 - SDH occurs due to ruptured bridge veins and subdural space [52] [41]. It is caused by depressed skull fractures, with the bones penetrating the interior and rupturing the veins and subdural space.
 - Together with diffuse axonal Injury (DAI), SDH is responsible for more deaths from head injuries than all other combined injuries. In some studies incidence rates reach 30% of mortality rates and in others they can reach 50%, as in the Swedish population [53].
 - ICHs are located in the brain parenchyma and are a well-defined homogeneous cluster of blood created by a ruptured blood vessel at the time of Injury [51]. Unlike the injuries discussed above, ICH occurs not in the interior of the brain.

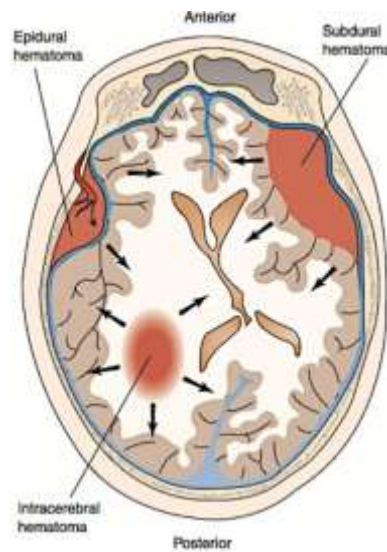


Figure 15. Possible focal brain injuries. Adapted from Porth et al. [52].

2.2.2.2 Diffuse Brain Injuries

Diffuse brain injuries are characterized by extensive brain dysfunction and the absence of macroscopic structural damage, making it difficult to detect in medical images [45]. They can occur without impact forces directly applied on the head, as they are created by inertial forces [54]. Patients who suffer minor head trauma may still have minor diffuse brain damage 100 days after the accident [41]. There are 2 types of diffuse injuries: Diffuse Axonal Injury (DAI) and Concussion.

- **Diffuse Axonal Injury:** results from the rupture of brain cells called axons located in the cerebral hemispheres and subcortical white matter [50]. It involves a loss of consciousness ranging from 24 hours to weeks after impact, severe motor and memory deficits and post-traumatic amnesia that can also last for weeks [50]. It mainly affects the cerebral hemispheres, corpus callosum, brainstem and cerebellum.
- **Concussion:** is characterized by a slight increase in intracranial pressure [55] and for transient loss of consciousness or even posttraumatic amnesia of varying duration in severe cases. Mild concussions, which are the most common diffuse injuries that can occur due to a head impact, with symptoms such as disorientation and confusion, and mild concussions can lead to a loss of consciousness up to 24 hours after the impact.

2.2.3 Head Injury Criteria

Current standards used by the automotive and sports industries for predicting head injuries are the Gadd Severity Index (GSI) [56] and the Head Injury Criterion (HIC) [57], although there are some controversies about these indices [58] since both depend only on the linear acceleration of the head's centre of gravity, leaving aside the angular acceleration [59]. Also, these indices, which are based on Wayne State Tolerance Curve (WSTC) data (the curve that describes the relationship between linear head acceleration, duration of acceleration and onset of concussion) are derived from frontal impacts only, disregarding injuries from other directions [60]. Further studies [61] [62]

proposed another injury criterion entitled Head Impact Power (HIP), which combined the translational and rotational accelerations of the head. Alongside head kinematics, there are many other proposals for injury tolerance limits to other biomechanical proposals found in the literature [14]. Table 7 will show a summary of the proposed limits in the literature for skull fracture.

Parameter	Localization	Limit	Reference
Von Mises's Stress (MPa)	Skull	34.47-103.42	McElhaney et al. (1970) [63]
		153	Schaller et al. (2012) [64]
Linear acceleration (g)	Skull	> 80g	Got et al. (1978) [65]
Energy of Deformation (J)	Frontal	1.59 - 2	Gurdjian et al. (1958) [66]
	Occipital	0.91	
	Skull	14.1 – 68.5	Yoganandan et al. (1995) [67]
		> 2.2	Baumgartner et al. (2005) [68]
Peak Force (kN)	Skull	4.5 – 14.1	Yoganandan et al. (1995) [67]
	Frontal	4.2	Nahum et al. (1968) [69]
		5.5	Hodgson et al. (1971) [70]
		6.2	Advani et al. (1975) [71]
		4.7	Allsop et al. (1988) [72]
	Lateral	3.6	Nahum et al. (1968) [69]
		2.0	Schneider et al. (1972) [73]
		5.2	Allsop et al. (1991) [74]
	Occipital	12.5	Advani et al. (1982) [75]

Table 7. Tolerance limits for skull fracture. Adapted from Tse et al. [14] and Schmitt [40].

2.3 Skull fracture mechanics

To better understand traumatic head injury, mechanical and mathematical models of the human head are being developed. Essential to the development of these models is the study of the mechanical behaviour of the materials and structures which constitute the human head. The main building component of the bone tissue is mineralized collagen fibril (ossein) [21]. The collagen fibres in the outer and inner table (cortical bone) are arranged hierarchically. On the contrary, in the trabecular bone, collagen fibrils are oriented irregularly, and the structure is spongy. The position of fibres in the bone affects its mechanical properties.

2.3.1 Sandwich structures and cranial bone

The bones of the skull are generally layered with compact inner and outer tables separated by a porous diploë layer. When a layered panel is transversely loaded, four types of deformation lead to transverse deflection: membrane deformation, bending deformation, shear deformation, and local core compression and puncture of the skull [76].

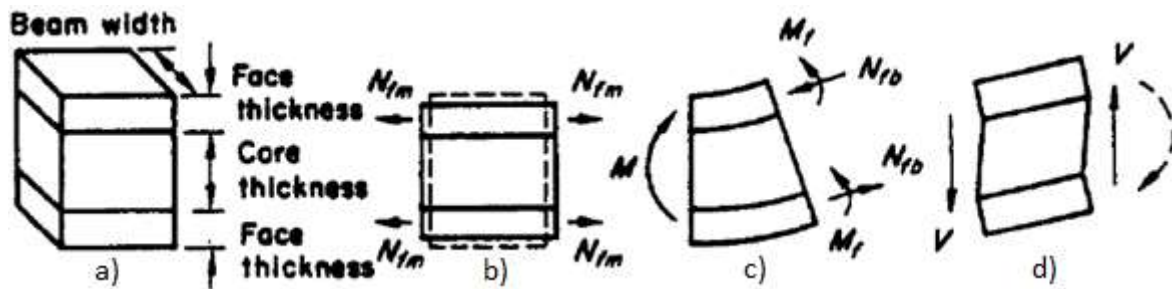


Figure 16. Layered beam element and deformations - a: layered beam element; b: membrane deformation; c: bending deformation; d: shearing deformation [76].

2.3.1.1 Membrane deformation

Membrane deformation is a stretching or compression of the layered structure in the plane of the panel and is resisted by normal stresses which are evenly distributed across transversely. Membrane deformation leads to resultant forces (N_{fm}) in the faces which are equal in magnitude and in the same direction (Figure 16.b) [76]. Because the beam core is much less stiff than the faces, forces developed in the core due to membrane deformation are usually insignificant.

2.3.1.2 Bending deformation

Bending deformation causes a change in the curvature of a layered panel and is resisted by a normal stress distribution which changes from tensile in one face to compressive in the other face. Bending of a layered beam leads to resultant forces in the faces (N_{fb}) and moments (M_f) in each face (Figure 16.c) [76]. Again, forces developed in the relatively low-stiffness core are insignificant when compared to the forces in the faces.

2.3.1.3 Shearing deformation

Shearing deformation in a layered panel is due primarily to deformation of the relatively low-stiffness core material and can be a significant part of the total deformation of a layered structure. For a layered beam, transverse shear leads to the deformation shown in Figure 16.d [76]. The presence of transverse shear deformation as a significant part of the deformation of a sandwich structure is a complicating factor when compared with single-layered structures in which shear deformation is often not significant. Likewise, the presence of significant shear deformation in layered cranial bone could complicate modelling and analysis of the skull.

2.3.2 Fractures and Cranial Sutures

Despite the efforts made to understand the global functionality and mechanics of the head, little attention has been paid to the understanding of the biomechanical features of the skull and the cranial sutures, especially in the context of sutures under dynamic loading conditions. To try to fill that gap of knowledge, Ptak et al. [21] investigated how dynamic loading affects the mechanics of cranial sutures and surrounding bones. For that end Ptak et al. [21] simulated a case based on a real-world car accident with a vulnerable road user (cyclist). First, they created a skull model where external and internal surfaces (cortical bone) were assigned with the same thickness of 1mm and meshed with *penta* finite elements and the trabecular layer meshed with *tetra* finite elements. A

total of six skull models were analysed, varying the stiffness of cranial sutures, which response was further compared to a model without sutures as shown in Figure 17.

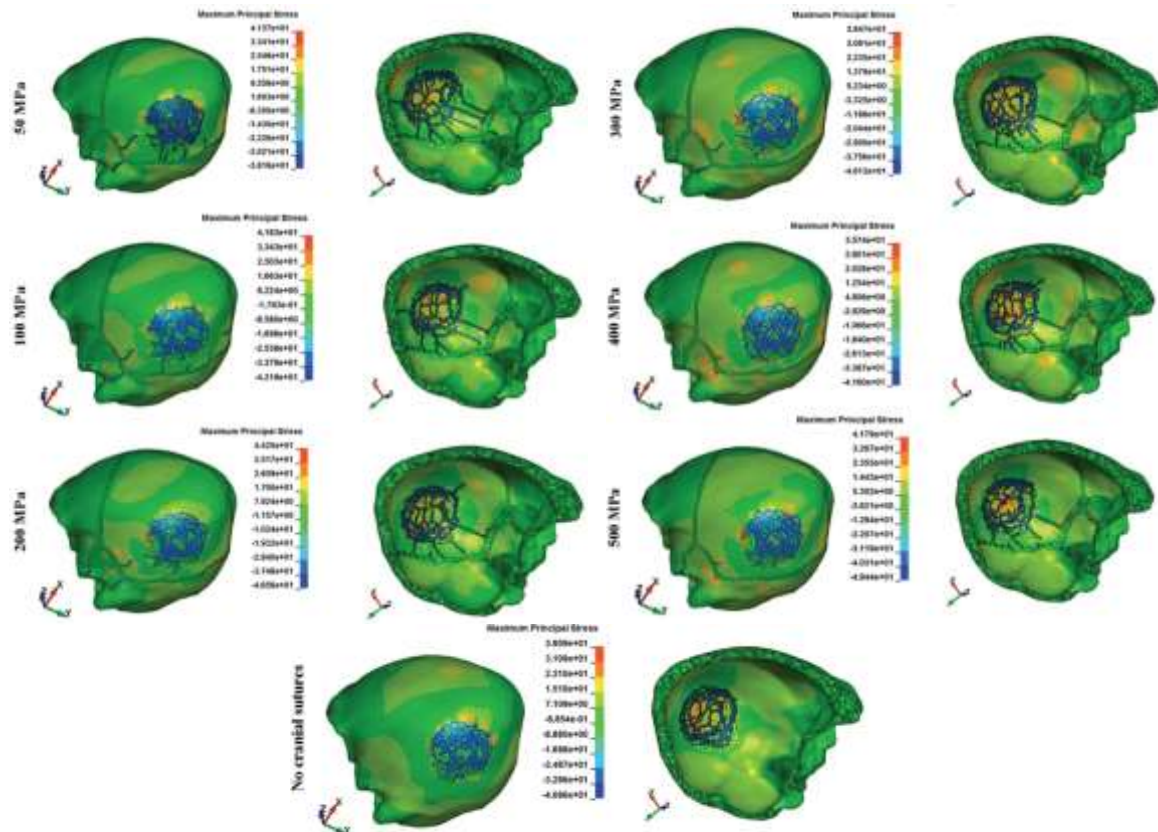


Figure 17. Distribution of maximum principal stress and fracture pattern on outer and inner layers for cranial sutures with Young's modulus within the range of 50–500 MPa and for a skull without cranial sutures (at 5 ms after the impact) [21].

The results of Ptank et al. [21] research have shown that the stiffness of cranial sutures plays an important role in the stress distribution and energy absorption. The angle between the direction of the fracture and the tangent line to the sutures in the starting point of the crack is tending towards 90°. The reason given is that since the suture Young's modulus is lower than the bones, the increased capability to deform means also that the suture is not able to prevent the skull bone from bending. As a result, the fracture occurs at the tensile side of the bone perpendicular to the suture. Even though most of the eroded finite elements occurred in the outer layer, which is subjected to the direct contact with the vehicle frontend, many of the long cracks occurred on the inner layer.

Ptak et al. [21] showed that fracture initiates in the inner cortical layer, which might be connected to different ultimate stresses for tension and compression. In fact, the ultimate tensile stress of cortical bone is lower than the ultimate compressible stress. This leads to a crack initiating in a notch on the tensile side of the bent bone, which leads to the observed behaviour of an initial cracking on the inner layer, followed by the outer cortical layer. Thus, it is possible to conclude that

the modelling of cranial sutures is vital for a realistic model when it comes to simulation of skull fractures.

2.4 Finite elements head models (FEHM)

Since the 1940s, there have been several attempts to model the human head analytically. However, due to mathematical difficulties in formulating and obtaining the analytical solution, these models of mathematical or analytical heads could only be represented by regular circular or ellipsoidal geometries, simple boundary conditions and homogeneous properties of the material. On the other hand, numerical approaches such as finite element model (FEM) greatly simplify analytical problems by using approximations to the analytical formulation or solution, making it more adaptable to digital computing techniques, and faster accepting various forms of calculation tolerance [14].

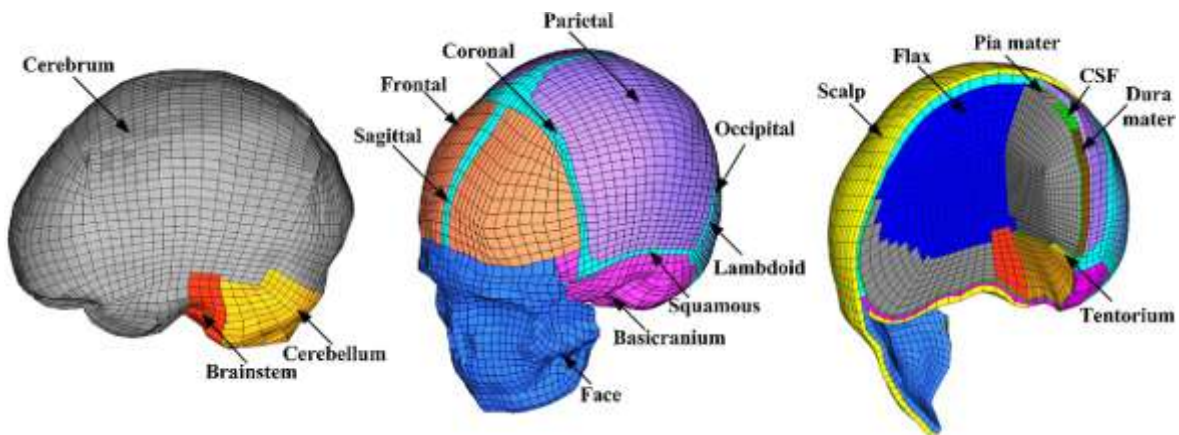


Figure 18. Representation of a finite element model. Adapted from [77]

2.4.1 History of finite elements head models

The first attempt to model the behaviour of the human head response through FEM was made by Hardy and Marcal [78], who constructed a two-dimensional (2D) FEHM, which consisted of only the skull that was later enhanced by Shugar [79] by adding an elastic, fluid-filled brain that is assumed to be firmly attached to the skull. 2D plane deformation models, representing various cross-sections of the head, were the only means to simulate impacted head deformations due to the lack of computational resources in the 1970s. The first three-dimensional (3D) FEHMs were generally simplified using regular geometries (spherical or ellipsoidal solid or shell) [80] [81]. For example, Chan [82] modelled the human head as a spherical shell and a prolate ellipsoid, while Khalil and Hubbard [81] used an ellipsoid shell for the skull and a zero viscosity fluid as intracranial content.

These geometrically simplified models considered the anatomical and material characteristics of only one of the two main structures, namely the skull or the brain. A 3D model that represented the basic anatomy of the skull and brain was developed by Hosey [83] in 1981. His model was considered the most comprehensive head and neck model in the 1980s [84], did not only include the anatomy of the head, brain and neck but also took into account the inertial and material properties of the head and neck. In Figure 19, a representation of the model can be seen. The foregoing FEHMs,

which are generally considered unrealistic today, represented a first step in the theoretical analysis of the biomechanics of head injuries. Only in the 1990s, it was possible to develop a more realistic and comprehensive 3D FEHM based on the actual geometry of the human head.

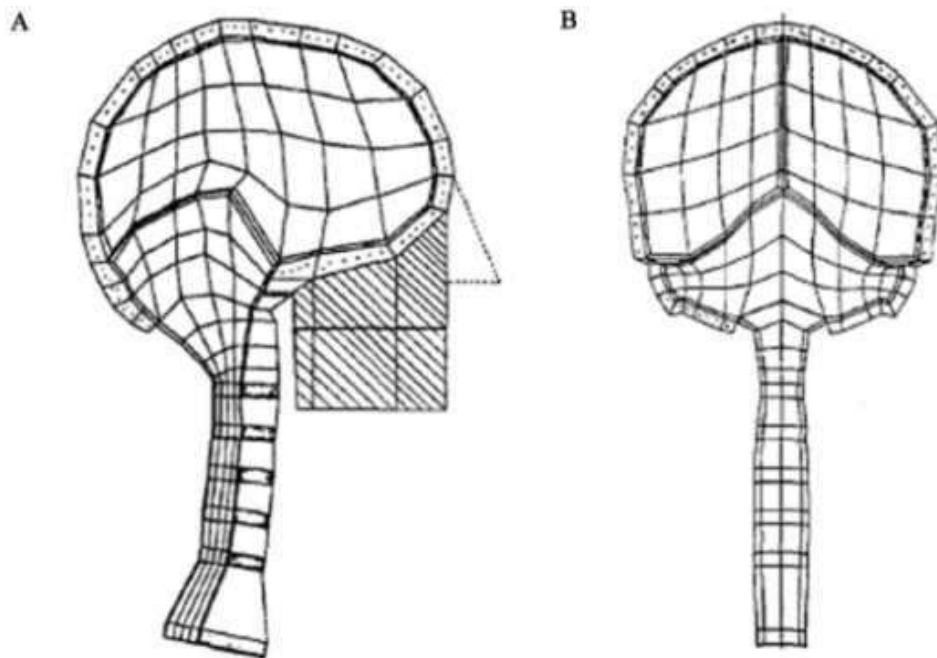


Figure 19. Finite element head model developed by Hosey [69]. A: sagittal section; B: Coronal section [14].

Ruan et al. [85] built a detailed FEHM simulating the detailed anatomy of the skull and brain (Figure 20). This FEHM was the first version (1993-1997) of the well-known Wayne State University Brain Injury Model (WSUHIM) containing 7351 elements. The skull, brain and CSF were developed with eight-node hexahedron elements, while the scalp, dura mater and brain scythe were constructed with four-node shell elements. WSUHIM was further enhanced by Zhou et al. [86] in 1995 with 22995 elements. The model was later revised and refined by Zhang et al. [87] in 2001 to introduce a sliding interface between the skull and the brain.

In 2003, King et al. [88] completely revised the previous version of WSUHIM and built a much more refined head model. The fully revised model simulated most of the essential anatomical features of a 50th percentile male head, including the scalp, dura mater, cerebral scythe, tentorium, pia mater, CSF, cerebral hemispheres with distinctive white and grey matters, cerebellum, ventricles, brain-stem and skull with outer table, diplöe, inner table and facial bones. This latest revised version of WSUHIM contained 314500 elements.

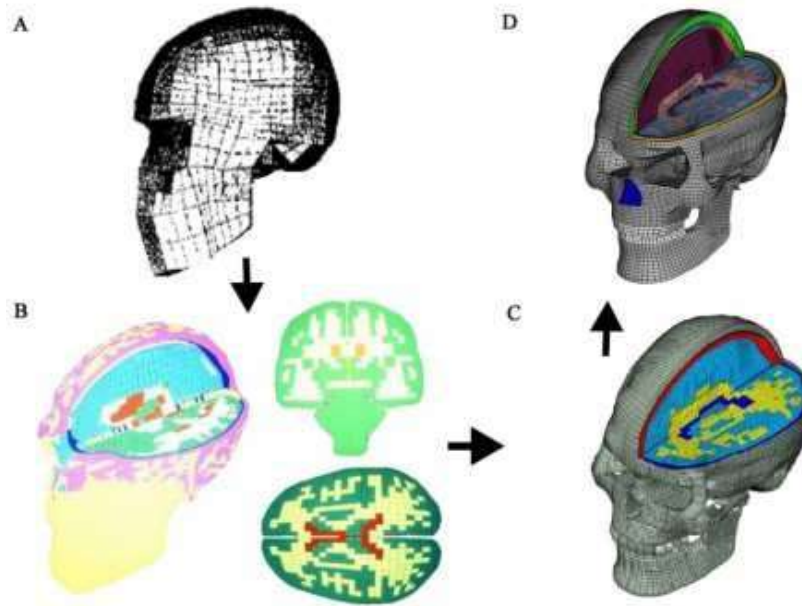


Figure 20. Various versions of WSUHIM. (A) 1st version by Ruan et al. (1993); enhanced versions by (B) Zhou et al. (1995) followed by (C) Zhang et al. (2001); (D) latest version has been reviewed by King et al. (2003) [14].

Another representative FEHM is the Strasbourg University Finite Element Head Model (SUFEHM), which includes almost all mechanically relevant parts of the head, e.g. the scalp, skull, brain, CSF, tentorium and falx (Figure 21). It was developed under the Radioss code by Willinger et al. [89] and validated against Nahum's [90], Trosseille's [91], Yoganandan's [67] and Verschueren's [92] cadaveric experiments. The falx cerebri and the tentorium of the cerebellum are meshed with shell elements. The skull is modelled as a constant thickness three-layered composite with shell elements. The other features are represented by brick elements. This FEHM is continuous and represents an average adult human head. The brain/skull interface was modelled to represent every anatomical component that is included in that space: membranes (dura, arachnoid and pia), cerebral spinal fluid and vessels. The tentorium separates the brain and cerebellum and the falx cerebri divides both hemispheres. One layer of brick elements simulating the cerebral spinal fluid surrounds these membranes. The skin was modelled by one layer of brick elements and surrounds the skull and the facial bone. Overall, the SUFEHM consists of 13208 elements.

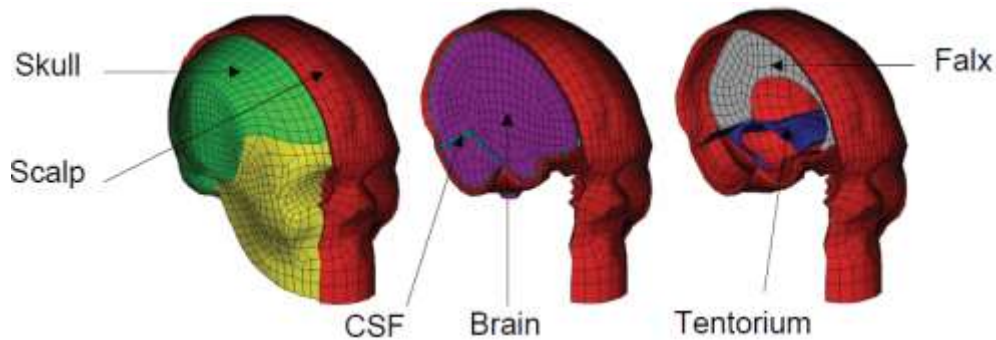


Figure 21. The Strasbourg University Finite Element Head Model (SUFEHM). Adapted from [93].

In 2002, Kleiven and Hardy [94] proposed a detailed and parameterized model of an adult FEHM, known as Kungliga Tekniska Högskolan (KTH) FEHM (Figure 22), which included scalp, skull, brain, meninges, CSF, eleven pairs of bridge veins and simplified neck. The KTH FEHM contained 18400 elements and was modelled with isotropic, homogeneous, nonlinear and viscoelastic material properties based on the work of Mendis et al. [95]. In their model, the inner and outer surfaces of the skull are scaled independently, and the width, length, height, and thickness of the skull can be adjusted. The model was comprised of 19350 nodes, 11454 eight-node brick elements, 6940 four-node shell and membrane elements, and 22 two-node truss elements.

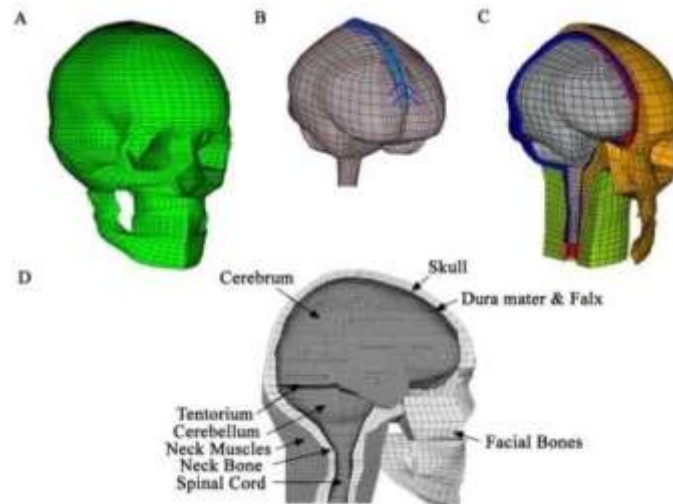


Figure 22. Kungliga Tekniska Högskolan (KTH) FEHM. (A) skull model; (B) brain model with 11 pairs of bridge veins; (C) sagittal cross-section of the head and neck model; (D) anatomical structures modelled [14].

Takhounts and Eppinger [96], in 2003 proposed the “Simulated Injury Monitor” (SIMon) FEHM. The SIMon FEHM consists of the rigid skull, the dura-CSF layer, the brain, the falx cerebri, and the bridging veins. The SIMon FEHM consists of 42500 nodes and 45875 elements, of which 5153 are shell elements (3790 rigid ones), 14 are beam elements, and 40708 are solid elements. Of the solid elements, 49% belong to the nondeformable rigid skull, as shown in Figure 23.

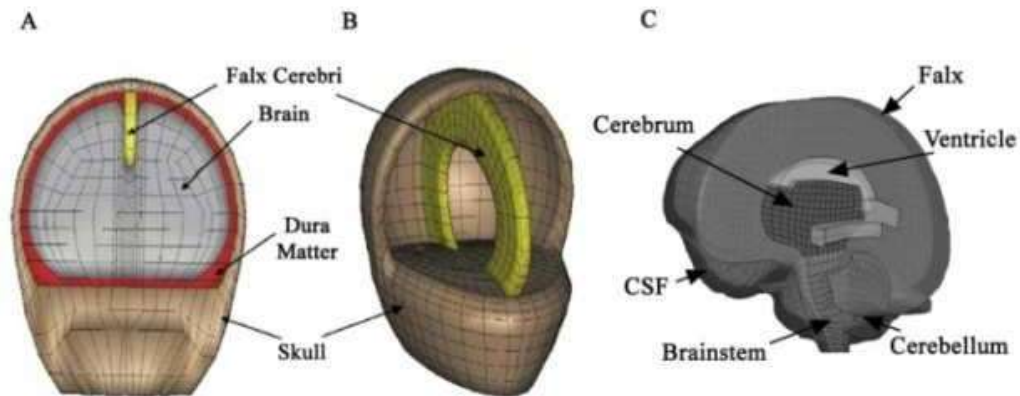


Figure 23. The SIMon head model. (A) Coronal cross-sectional view; (B) View illustrating the model without internal brain tissues; (C) Revised version of SIMon FEHM [14].

Meanwhile, in the same year, Horgan and Gilchrist [97] constructed the University College Dublin Brain Trauma Model (UCDBTM) to simulate the transient occurrences of simple pedestrian accidents, this skull-brain complex included a scalp, a three-layered skull, dura mater, CSF, pia mater, cerebral scythe, tentorium, cerebral hemispheres, cerebellum and brainstem (Figure 24). Two models of a 3-layered skull with variable thickness were created, consisting of outer and inner tables and *diplöe*. For the first, the scalp was modelled using shell elements, cortical and trabecular bone with brick elements of varying skull thickness, the dura with membrane elements, CSF with brick elements, pia with membrane elements, falx and tentorium with shell elements and the cerebrum, cerebellum and brain stem with brick elements [97]. The second model is similar apart from the skull being modelled using a composite shell element, and the scalp being modelled with brick elements. The models were validated by simulating the cadaveric head impact experiments of Nahum et al. [90] and by directly comparing the predicted pressure-time histories against those obtained experimentally.

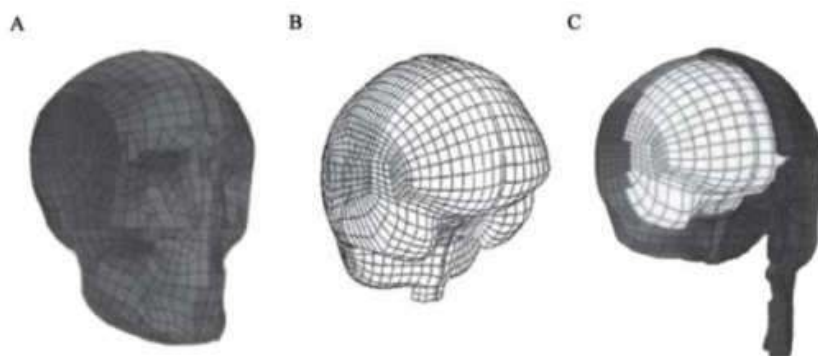


Figure 24. Illustration of the brain injury model at the University of Dublin (UCDBTM). (A) the skull; (B) the brain; (C) partial cut-view illustrating the intracranial content [14].

Both Table 8 and Table 9 summarise the variety of characteristics for the skull models of the models previously presented.

FEHM	Material property	Element type	N of elements of whole model	Structure	Interactions Skull-Brain	Type of validation	Experiment used to validate
SUFEHM	Elastic Plastic Brittle	shell	13208	3 layered skull	CSF modelled as solid element	local (frontal skull fracture)	Verschueren et al. [92]; Yoganandan et al. [98]
WSUHIM	Elastic Plastic	Solid (trabecular bone)	314500	3 layered skull	Sliding w/o separation; Tied interface	global (intracranial pressure)	Nahum et al. [90]
		shell (cortical bone)					
KTHFEHM	-	-	19350	3 layered skull	Tied interface between skull and dura; sliding interface between meninges and brain	global (intracranial pressure)	Nahum et al. [90]
SIMon FEHM	Rigid	solid	45875	Single part	Tied interface	global (intracranial pressure)	Nahum et al. [90]; Trosseille et al. [91]
UCDBTM	-	1 with shell and another with solid	50000	3 layered skull	Tied interface	global (intracranial pressure)	Nahum et al. [90]

Table 8. Skull model differences between FE head models.

	SUFEHM		WSUHIM		KTHFEHM		SIMon FEHM	UCDBTM	
Bone type	cortical	trabecular	cortical	trabecular	cortical	trabecular	whole skull	cortical	trabecular
E (MPa)	12000	1000	6000	560	15000	1000	6900	15000	1000
ν	0.21	0.05	0.25	0.3	0.22	0.24	0.3	0.22	0.24
ρ (kg/mm ³)	1.90E-06	1.50E-06	2.10E-06	1.00E-06	2.00E-06	1.30E-06	3.52E-05	2.00E-06	1.30E-06
T_u (MPa)	100	32.4	-	-	-	-	-	-	-
thickness (mm)	2	3	1	variable	variable		variable	-	-

Table 9. Skull material model differences for different FE head models.

2.4.2 Comparison between different types of solid elements

To better choose the element type that will be used in the skull model, some studies available in the literature were reviewed. From those, the studies of Wang et al. [99] and Tadepalli et al. [100] were the particular ones chosen because both compare the element types considered to be used in this model, hexahedral and tetrahedral elements.

2.4.2.1 Wang et al. [99] study

This study presented some analytical results and some test results for different mechanical problems, which were then simulated using finite element analysis with tetrahedral and hexahedral shaped elements. The comparison was done for linear static problems, modal analyses and nonlinear analyses involving large deflections, contact and plasticity. From this, as can be seen in Figure 25, Wang et al. [99] concluded that:

- Avoid linear tetrahedral elements. These are excessively stiff.
- Quadratic tetrahedral elements are very good, but computationally expensive.
- Linear hexahedral elements are sensible to the corner angle. The users should be careful to avoid large angles in stress concentration regions. Extra shape functions or the enhanced strain formulation should be activated for bending dominated problems.
- Quadratic hexahedral elements are very robust, but computationally expensive.
- For thin-walled structure the limit element edge/thickness ratio to use tetrahedra is about 2000.

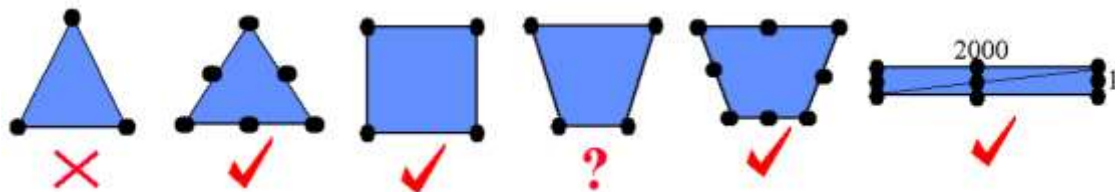


Figure 25. Results and recommendations outlined schematically, adapted from Wang et al. [99].

2.4.2.2 Tadepalli et al. [100] study

In this study, various FE simulations were performed to study the effect of element type on the relative prediction of contact pressure and contact shear stress distributions, and solution time. Tadepalli et al. [100] used simulations to examine the advantages and disadvantages of tetrahedral and hexahedral elements under compression and shear loading, material incompressibility, and frictional contact conditions, which were commonly seen in foot and footwear biomechanics. Bone, floor, soft tissues and insole were modelled.

From this study, Tadepalli et al. [100] concluded that hexahedral elements consistently predicted reasonable contact pressures and contact shear stresses regardless of loading conditions, material incompressibility, contact, friction, and footwear condition (barefoot or with insole) while having a reduced CPU and wall clock time, compared with the tetrahedral elements (Table 10). However, the results from models with linear tetrahedral elements indicated that these elements should only

be used under frictionless contact conditions or when the material incompressibility condition can be relaxed. It was clear from their results that a model solved on Abaqus using linear tetrahedral elements to simulate barefoot conditions resulted in very poor shear stress predictions. From Table 10 it can also be seen that quadratic tetrahedral take substantially more time comparatively to both linear hexahedral and tetrahedral elements, making a strong case for the use of linear hexahedral elements in this dissertation skull model.

Element Type	No. of elements	No. of nodes	CPU time (s)	Wall clock time (s)
Linear hexahedral (C3D8H)	33120	37235	5408.7	597
Linear tetrahedral (C3D4H)	106261	20206	6598.5	790
Quadratic tetrahedral (C3D10I)	39732	60858	26081	2239

Table 10. Computation and real-time results for frictionless contact and compressive load tests, performed by Tadepalli et al. [100].

2.4.3 Experimental investigations of the human skull bone behaviour

Due to the frequent occurrence of skull fractures from unintended head impacts, there is an immediate need to develop injury assessment tools for evaluating the risk of skull fracture under the high-speed projectile impacts. Skull fracture tolerance has been shown to be dependent on impactor characteristics such as size and shape, as well as subject-specific anatomy [101]. Accurate strain data collected at the fracture location has historically been difficult to measure, which has led to the use of finite element models.

In order to incorporate an accurate representation of skull fractures in FEHMs, experiments of skull impacts are necessary to simulate and validate the skull models. In this section, head impact tests aimed for skull fracture investigations will be presented as possible experiments usable to validate this dissertation skull model.

2.4.3.1 Verschueren's experiment for frontal skull fracture

The test setup consists of two pendulums, mounted over a steel bar that is fixed to the wall at one end and supported by steel structure at the other (Figure 26). The first pendulum on the left is made of steel, it has a mass of 14.3 kg, a length of 148 cm and is used to strike the blow. The second pendulum is made of aluminium with a mass of 9.6 kg and a length of 128 cm. The steel pendulum with a flat-surfaced cylindrical aluminium impactor with a diameter of 70 mm is instrumented to measure the impact force [92]. Frontal head impacts were conducted on 18 unembalmed post-mortem human subjects, within 5 days after decease [102]. Table 11 summarizes the experimental database of post-mortem human heads. The CT data enabled the evaluation of bone and scalp thickness at the impact site.

The tests have been performed at three ranges of impact velocity: low (3.60 ± 0.23 m/s), intermediate (5.21 ± 0.04 m/s), and high (6.95 ± 0.04 m/s). Seven specimens (1, 4-8, and 10) were initially tested

at low impact velocity in which fracture was observed in only two specimens 1 and 6. The rest of the specimens were tested at medium velocity, all specimens were eventually fractured. The fracture pattern was typically linear in the low and medium impact velocity. The fracture initiated at the impact point with an extension towards the orbital rims [102]. The fracture for higher velocity impacts was more complex. However, the linear fracture line towards the orbital rim has been reported to be visible in all the cases, as shown in Figure 27. Additionally, in the experimental results published by Delye et al. [102], specimens 2, 6 and 12-14 produced no result due to technical problems.

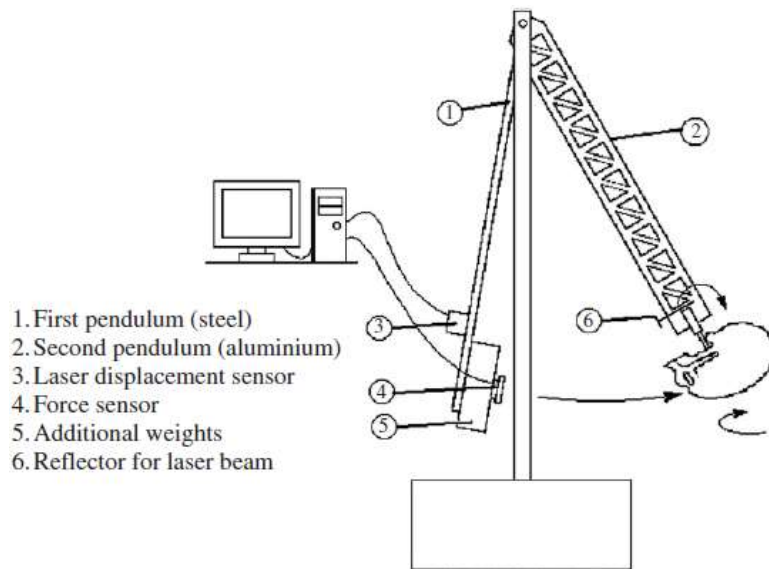


Figure 26. Frontal impact test setup by Verschueren et al. [92].



Figure 27. Left Image: Specimen no. 8 showing typical linear fracture pattern after being impacted at intermediate velocity; Right Image: Specimen no. 17 showing multiple fractures after being impacted at high velocity [102].

Specimen ID	Age (years)	Weight (kg)	Bone density impact site (mg/cm ³)	Bone thickness impact site (mm)	Scalp thickness impact site (mm)
1	73	3.6	1209	7.19	4.47
2	64	4.9	962	6.32	2.24
3	91	3.34	1043	10.64	3.27
4	82	3.22	1061	6.59	3.12
5	87	3.651	1166	6.8	4.79
6	76	3.72	1107	5.94	3.43
7	72	3.04	1097	13	3.35
8	73	3.615	1075	11.13	2.48
9	81	3.99	1098	7.34	2.25
10	79	3.83	1112	6.2	3.37
11	80	3.2	1146	4.88	2.36
12	90	3.125	1106	8.75	3.5
13	95	3.335	1069	7.44	3.38
14	93	2.72	1015	9.29	2.41
15	90	2.655	935	9.78	1.51
16	84	3.9	696	10.75	4.64
17	62	4.18	1037	8.67	3.8
18	88	2.99	1120	5.42	2.66

Table 11. Experimental Data Base from Katholieke Universiteit Leuven [102].

2.4.3.2 Huang's study for temporoparietal skull fracture

The overall goal of Huang et al. [101] was to provide improved accuracy head response and bone strain data from temporoparietal head impacts to post-mortem human subjects (PMHS) to develop biomechanically-based FE models for predicting localized depressed, comminuted skull fracture (when the bone is broken into more than two pieces). With the secondary goal of investigating the ability of FE models to accurately predict the fracture patterns observed in PMHS [101].

Experimental Setup

An unembalmed post-mortem human cephalic specimen was acquired from the International Institute for the Advancement of Medicine (Jessup, PA). A nine-accelerometer array using the 3-2-2-2 arrangement was mounted to the frontal bone to measure linear and rotational head accelerations. An Endevco model 7270-20,000g accelerometer was mounted to the rear aspect of a rigid 38.1 mm projectile to measure the impactor's acceleration and from which impact force was calculated using the projectile mass (0.10 kg) and applying Newton's Second Law (Figure 28).

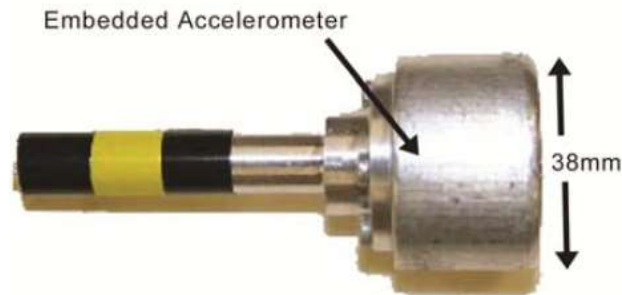


Figure 28. Instrumented impactor from Huang et al. experiment [101].

Rectangular Rosette-style strain gages (Vishay Micro-measurements, Malvern, PA) were utilized to collect bone strain data near the impact site and served to assist in identifying the time of fracture during the loading event. Three locations surrounding the impact site were chosen (Figure 29).

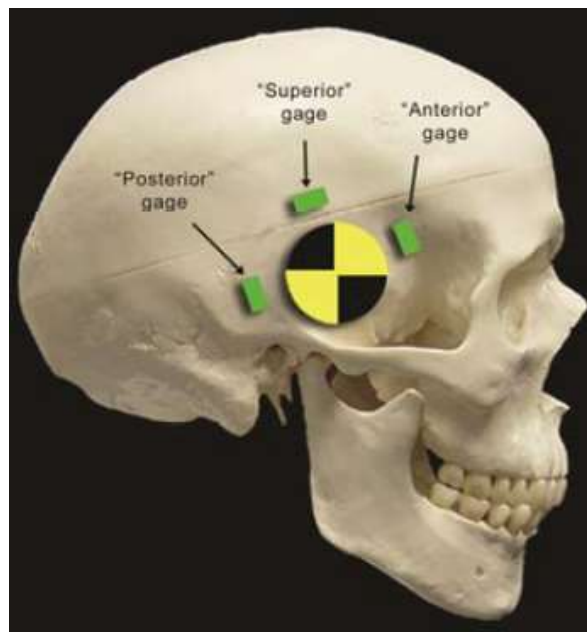


Figure 29. Strain gage locations relative to the impact site from Huang et al. [101] experiment.

The impact point was determined by first experimentally locating the head centre-of-gravity and then adjusting the impact point to allow enough clearance between the impactor and the zygomatic arch and the zygomatic region of the frontal bone. This resulted in a targeted impact point 25 mm anterior to the external acoustic meatus and 35 mm superior to the Frankfurt Plane. The specimen was then inverted and hung from an adjustable, lightweight suspension system. The impactor was aligned such that the impactor face struck the specimen normal to the skin surface. Two impact conditions were performed: Condition A was performed at a target velocity target of 20 m/s to the right side while Condition B was targeted for an impact velocity of 35 m/s to the left side [101].

FE mesh creation

After performing the experiments, Huang et al. [101] used a systematic approach to develop a subject-specific human head FE model using the following steps:

1. Anatomical reconstruction of CT images and geometry extraction;
2. Geometry refinement. The surfaces of each anatomical part were smoothed, which led to the generation of IGES surfaces;
3. Finite element mesh generation. FE meshes of each anatomical part were created from the IGES surfaces.

Results of the Huang's study

Having into account that the stress threshold for skull fracture was dictated by matching the fracture results of the 35 m/s impact while maintaining a “no fracture” result from the 20 m/s impact test, Huang et al. [101] observed that for the 35 m/s PMHS test, due to the localized impact, a depressed fracture was generated measuring 43 mm in superior-inferior direction and 67 mm in the anterior-posterior direction. The FE simulation produced a similar depressed fracture measuring 42 mm in both directions using a failure stress of 150 MPa to emulate fracture propagation shown in Figure 30. Figure 31 shows a cross-sectional view of the FE model at the depressed fracture location and compares it with the CT image at the corresponding position from the PMHS.

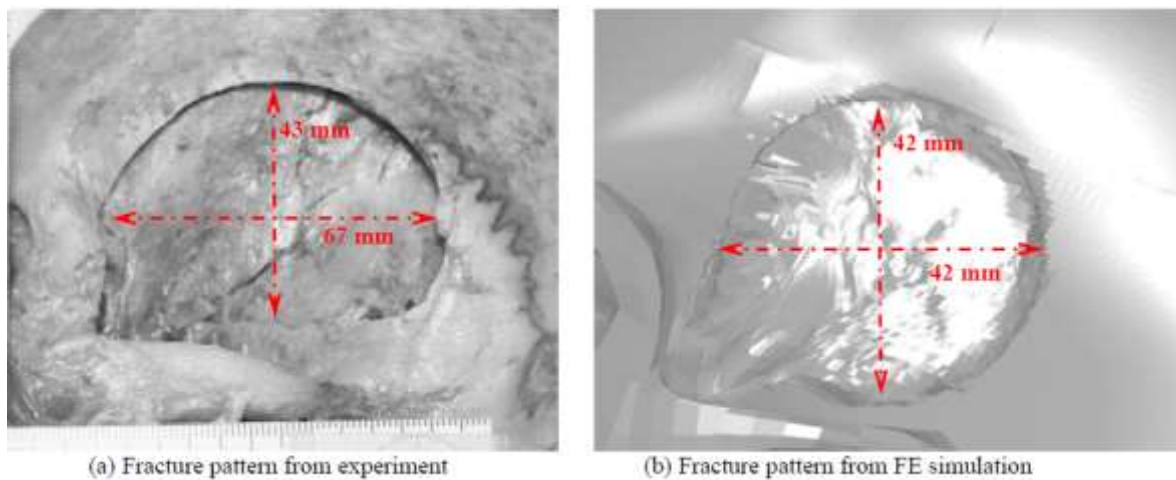


Figure 30. Comparisons of depressed skull fracture pattern from the 35m/s experiment and the corresponding FE simulation [101].

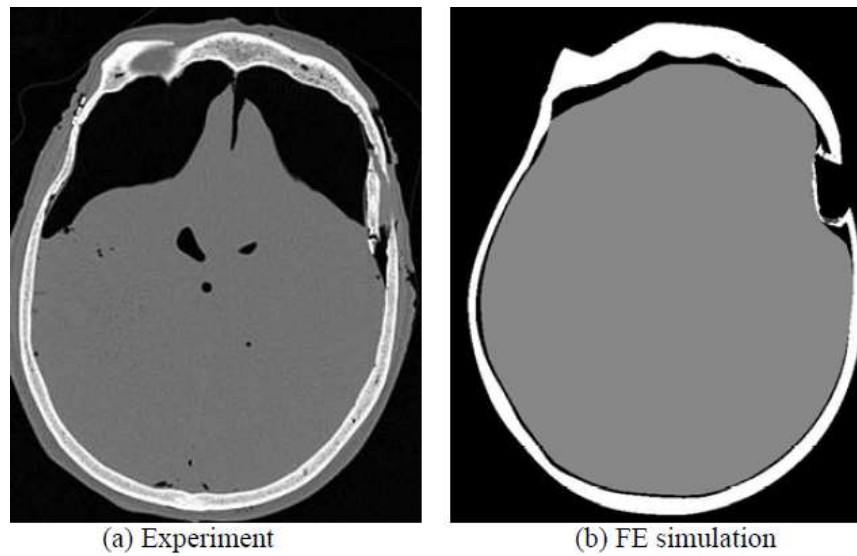


Figure 31. Comparisons of fracture pattern from a cross-section view of the FE model with a CT image in the corresponding position (axial plane) [101].

2.4.3.3 Yoganandan's Skull Fracture Study

Yoganandan's study was conducted in order to determine the biomechanics of the human head under quasistatic and dynamic loads at different strain rates. Twelve unembalmed intact human cadaver heads were tested to failure using an electrohydraulic testing device [67].

ID	Sex	Age	Height (cm)	Weight (kg)	Impact Site
1	M	65	173	50	Vertex
2	M	75	185	68	45° right lateral
3	F	63	168	77	45° right lateral
4	F	76	157	102	45° right lateral
5	M	70	183	86	45° frontal
6	F	74	165	73	45° rear
7	M	65	185	95	Vertex
8	F	67	165	68	45° frontal
9	F	50	168	84	Vertex
10	F	61	162	61	35° rear
11	M	---	---	----	Vertex
12	F	78	160	36	Vertex

Table 12. Description of the twelve unembalmed human cadavers [67].

Unembalmed human cadavers were used in the study. The age, height, and weight ranged from 50 to 76 years, 1.6 to 1.8 m, and 50 to 102 kg, respectively. There were five males and seven females (Table 12). Physical measurements such as the nasion-occiput distance and the maximum circumference of the head were obtained. Table 13 includes the craniometric data for each specimen along with the mean values.

ID	Lateral-lateral (cm)	Antero-posterior (cm)	Nasion-occiput (cm)	Inferior-superior (cm)	Circumference (cm)	Skin thickness at impact site (cm)	Weight (kg)
1	15.2	20	19.4	15.9	58.4	0.6	3.98
2	15.9	19.1	18.7	16.2	61	0.9	4.09
3	16.2	20	19.8	16.2	57.2	0.8	4.29
4	14.3	18.6	18.4	13.5	54.9	0.7	3.21
5	16.2	19.7	19.1	15.6	59.4	0.7	4.72
6	14.6	28.7	16.5	16.2	52.7	0.6	----
7	15.6	18.7	21.6	16.8	57.8	0.8	4.12
8	14	19.1	17.5	15.9	54.6	0.5	3.21
9	15.9	18.1	17.5	15.9	57.2	1	3.41
10	14	18.4	17.1	14.9	54	0.8	3.34
11	14.6	19.1	19.4	14.3	54.6	0.5	3.52
12	14.7	16.5	17	14.5	49.5	0.5	2.81

Mean	15.1	18.8	18.5	15.5	55.9	0.7	3.7
SE	(±0.2)	(±0.3)	(±0.4)	(±0.3)	(±0.9)	(±0.1)	(±0.17)

Table 13. Physical data of the 12 unembalmed cadaver heads with respective mean values [67].

The specimens were prepared with a fixation device to achieve rigid boundary conditions at the distal end. A jig was designed for this purpose. It consisted of a rigid platform onto which a U-shaped heavy-duty bracket was mounted. The jig was used to rigidly fix the screws into the auditory meatus of the specimen. This fixation device permitted the preparation to receive direct contact, static or dynamic loads at the following anatomical sites: vertex, parietal, temporal, frontal, and occiput.

The specimens were loaded once to failure at quasi-static or at dynamic rates. Failure was identified as the level at which a further increase in piston excursion resulted in a decrease of the force. Dynamic tests were conducted by applying the load through the piston at constant velocities ranging from 7.1 to 8.0 m/s. Figure 32 includes a schematic of the five loading sites on the specimen showing the orientation and the force vector.

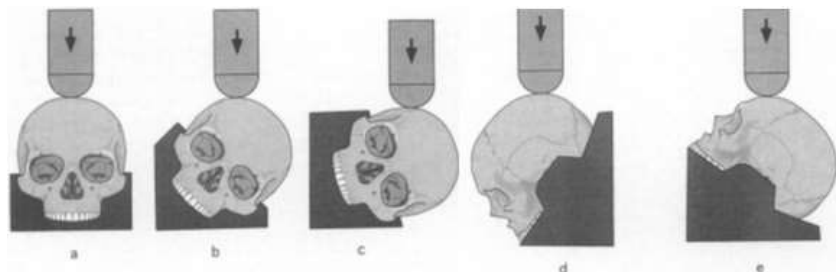


Figure 32. Schematics of the specimen orientation in the fixation device and the external load (shown by dark arrow) applied, (a) Vertex, (b) 45° right lateral (parietal), (c) 78° right lateral (temporal), (d) 45° rearward (occipital), and (e) 45° forward (frontal) regions [67].

2.4.4 Mesh Density: Computation cost vs Mesh convergence

In terms of the creation of the skull mesh part, the number of elements/mesh density of the part must be considered in order to obtain the lowest computation cost/time possible without jeopardizing the final results of those simulations. Huang et al. [101] compared the influence of different mesh densities for temporoparietal skull impacts simulations. Four mesh densities were considered in the study.

Mesh	Representative element size (mm)	No. of elements in the skull	Computation time (min)	Peak Impact force (N)
1	2.95	52010	50	3600
2	1.59	82506	127	3635
3	0.97	263197	476	3635
4	0.73	421681	1076	3619

Table 14. Comparison of computation cost and convergence of different mesh densities [101].

As can be seen from both Table 14 and Figure 33, with the increase of mesh density, the numerical accuracy increased but with a penalty of increased CPU time. The peak impact force increased from 3600 N to 3619 N (0.5% relative increase) when mesh size is decreased from 2.95 mm to 0.73 mm.

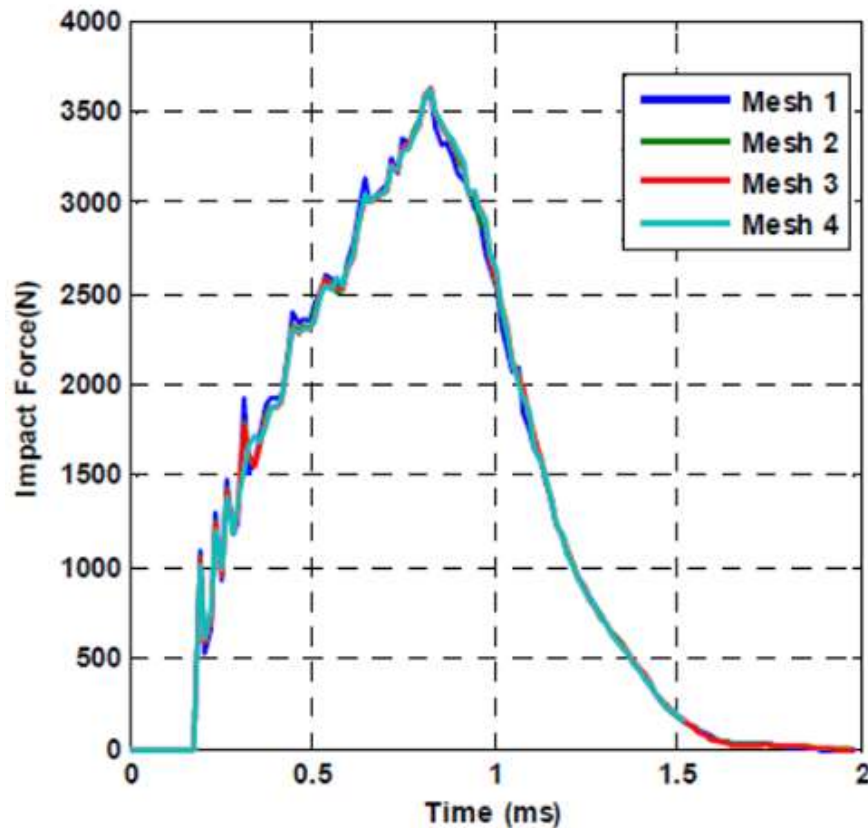


Figure 33. Comparison of head response for different mesh densities and peak impact force [101].

2.4.5 YEt Another Head Model (YEAHM)

YEAHM, developed by Fernandes et al. [3] containing a skull, brain and CSF, was further enhanced by Migueis [103] and Costa [104], adding the bridging veins. This is the base model used in this dissertation. This model contains several features, for instance, the sulci and gyri cerebral structures, an accurate representation of the brain geometry. Another characteristic is the type of interactions between parts. In most models, the skull and the brain are over-constrained, sharing nodes on the interface. This assumption is not realistic since there are relative movements between brain and skull, which is usually the cause of injuries, such as ruptured bridging veins or damage to the gyri, leading to SDH and contusion respectively. This model was developed using medical imaging, based on CT scans for the construction of bony structures and magnetic resonances for soft tissues.

In order to accurately generate skull geometry, 460 slices at 1.5 mm intervals images obtained from computed tomography were used. Brain geometry was generated from segmentation of magnetic resonance data and the same technique was used for the skull. Magnetic resonance data consisted of 181 weighted slices at 1mm intervals from a 65-year-old male human head. The following Figure 34 summarizes the process employed to develop the model.

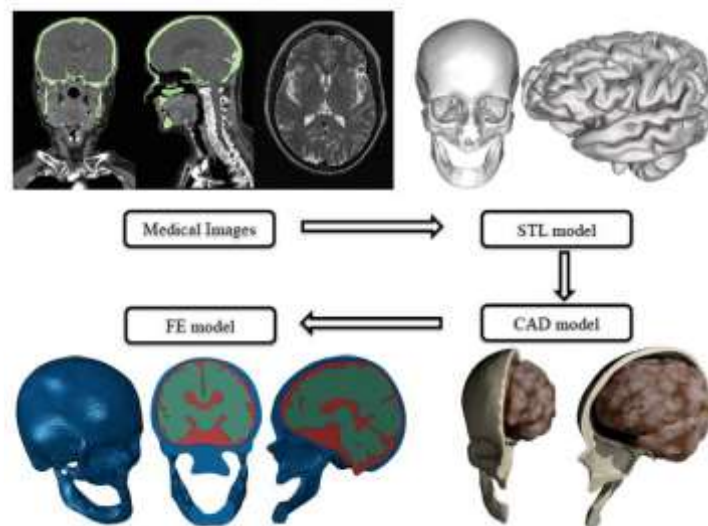


Figure 34. Illustration of the method used to create the YEAHM model. Adapted from Fernandes [3].

2.4.5.1 Characteristics of the YEAHM

The head model contains the skull, brain, CSF and bridging veins (BV) with the superior sagittal sinus (SSS). This base model that served as the basis for this dissertation is a homogeneous model, without any distinction between the various types of bone that make it up, like the cortical bone, the diploe and the sutures, that will be added in this dissertation. Figure 35 shows the different constituents of the base model used in the dissertation, showing the skull (blue), CSF (red), brain (green) and the bridge veins (yellow).

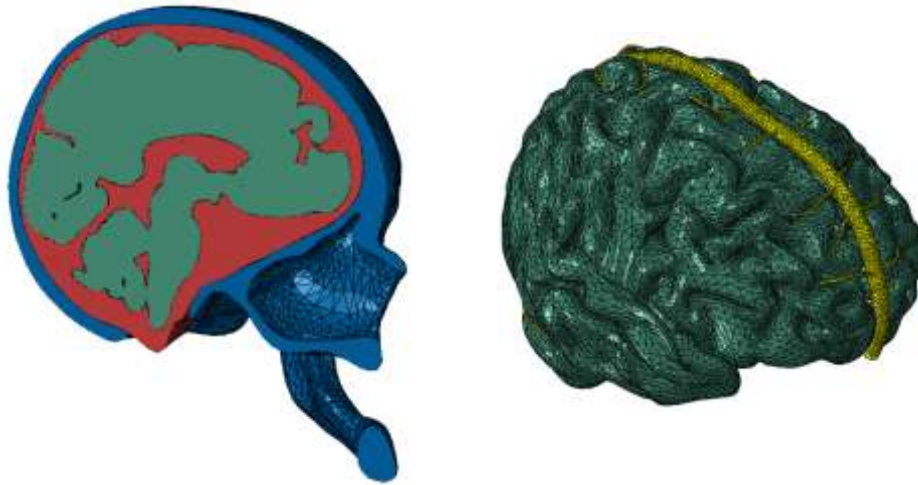


Figure 35. Constitution of the YEAHM model. On the left shows a section showing the skull (blue), CSF (red) and brain (green) and on the right shows the bridge veins (yellow) with the brain.

2.4.5.2 Material Model

The model of material adopted for the brain was a hyper-viscoelastic model (Table 15), while CSF (and all its simplified constituents) was defined as hyperelastic material (Table 16). The SSS and BVs were modelled with an elastoplastic law (Table 18). The only linear material employed was for the skull, modelling it as an elastic material model (Table 16), a very simplified material model without damage that doesn't contain differentiation between the different bone tissues of the skull.

ρ (kg/m ³)	μ (MPa)	α_1	D_1 (MPa ⁻¹)	g_1	g_2	τ_1 (s)	τ_2 (s)
1040	0.012	5.0507	0.04	0.5837	0.2387	0.02571	0.0257

Table 15. Properties of the material used to model the brain. Adapted from Fernandes [3].

ρ (kg/m ³)	C_{10}	C_{01}	D_1 (MPa ⁻¹)
1000	0.9	1	0.9

Table 16. Properties of the material used to model the CSF. Adapted from Fernandes [3].

ρ (kg/m ³)	E (MPa)	ν
1800	6000	0.21

Table 17. Properties of the material used to model the skull. Adapted from Fernandes [3].

E (MPa)	ν	Fracture Strain	Stress Triaxiality	Strain rate (s ⁻¹)	Displacement at fracture
25.72	0.45	0.31875	0.33	135.86	0.05

Table 18. Properties of the material used to model the bridge veins / superior sagittal sinus. Adapted from Costa [104].

2.4.5.3 Boundary conditions

The YEAHM features finite-sliding formulation interactions and kinematic contact between the CSF and the brain and between the CSF and the skull, with a coefficient of friction of 0.2 for tangential behaviour [105].

2.4.5.4 Mesh in YEAHM

Overall, a total of 1033976 elements compose the model, of which 836328 elements for the brain, 57257 elements for the skull, 98032 for the CSF and 42359 elements for the SSS + BV set [104]. Second-order C3D10M elements were used in detriment of the standard C3D4 tetrahedral elements. This type of element uses a condensed matrix formulation for dynamic analysis. These elements work well in contact situations, are more robust than C3D4 in situations of volumetric retention. When hourglass control is chosen (M), they usually do not propagate. This phenomenon can be observed in Figure 36, where it is possible to verify the sudden change of pressure values from element to element in a given region (*checkerboard pattern*), which points to the occurrence of volumetric retention. In addition, this type of element has four integration points instead of a single point that the first-order elements have, which provides a more detailed description of the stress and strain field which gives a better damage/rupture rating in the body under analysis [103].

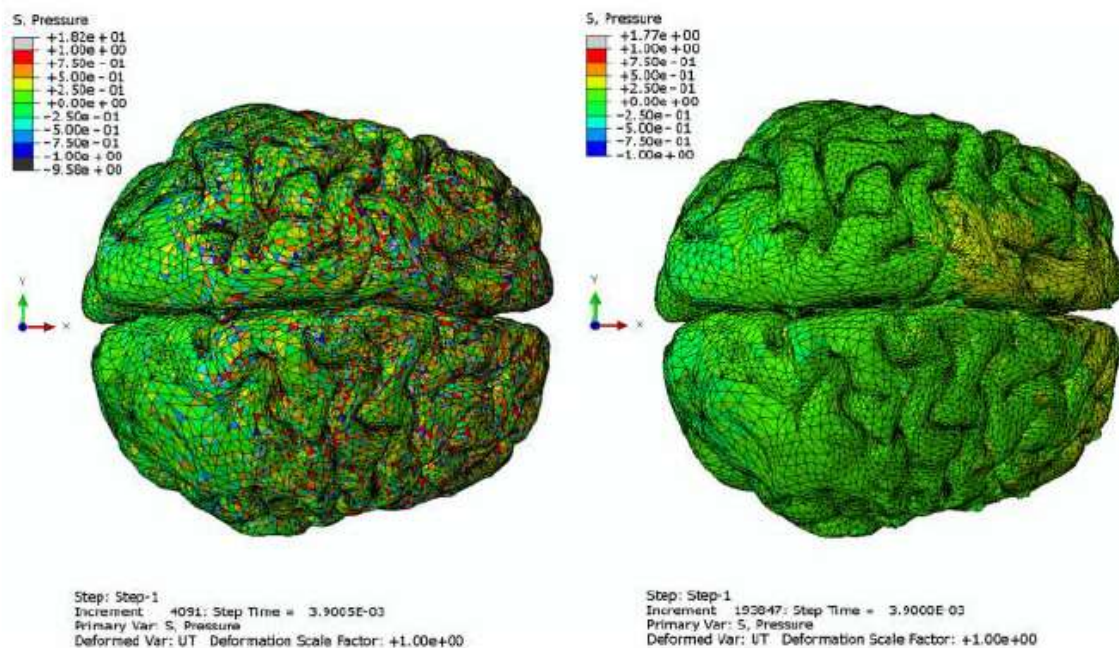


Figure 36. Pressure gradients obtained while using C3D4 elements (left) and C3D10M elements (right). Adapted from Fernandes et al. [3].

Chapter 3

Methodology

3.1 Geometrical Model of the Skull

As mentioned in the previous chapters, this work will use the latest YEAHM model, created by Fernandes et al. [3] and updated/improved over the years by students from the Mechanical Engineering Department of the University of Aveiro. This model contains the brain, the skull made of a single type of material, the CSF and the BVs and the SSS. The objective of this section will be to inform the reader as to how the segmentation of the skull, in its different bone tissues to create a more realistic model, was achieved.

After extensive research of the current literature on skull modelling, it was concluded that a geometrical model in which there was a separation between different bone tissues, respectively the cortical, trabecular and cranial sutures, with a cortical layer with a constant thickness would be the most appropriate to be made for this dissertation [36]. The primary reason is that this type of model has the best balance between reliable results and difficulty/cost of model creation. Within this type of models, it was also found that the best elements to utilize in the model are solid linear hexahedral elements, the reasons behind were that while the literature said can both linear/quadratic hexahedral and quadratic tetrahedral elements can be used, linear hexahedral elements have the advantages of needing fewer nodes while giving the same accurate results as quadratic tetrahedral ones [100], reducing the computation cost of the simulation performed afterwards by the model. There are mainly two reasons for the use of solid elements instead of shell for the cortical bone:

1. Construction of the model: with solids it is possible to quickly make adjustments to the model, adapt zones more easily than in the case of shells, also this way creates a better connection between sections because it would happen between elements of the same type.
2. Solids also have the advantages of handling double contact better and have a more accurate description of the stress gradient over the thickness, contrary to shells based on plane stress assumptions.

To this end, several methods have been tried, arriving at the end method that is presented below.

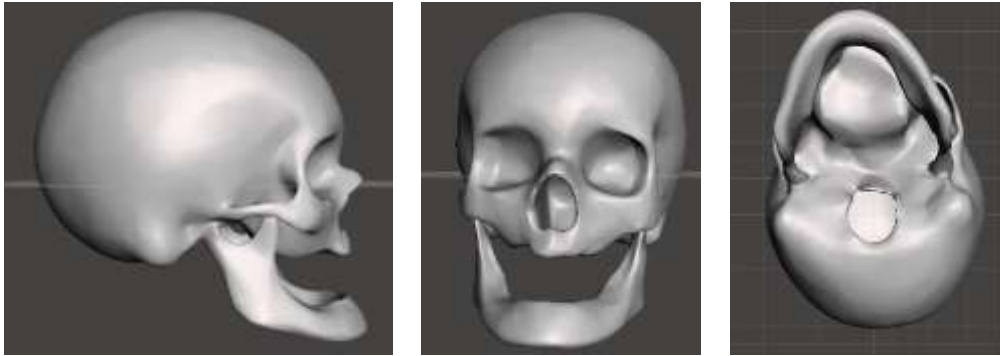


Figure 37. Skull model surface (STL version).

Firstly, the IGES file containing the skull model was transformed into a STL file (Figure 37) so that it can be worked on MeshMixer (Autodesk, USA), an open-source software that makes it possible to manipulate and to perform the necessary editing of the triangular mesh with relative ease. In MeshMixer, the mesh was separated into two distinct parts in the foramen magnum, a large opening through the occipital bone located in the centre of the posterior fossa of the neurocranium as can be seen in Figure 38, in order to obtain one internal surface and one external surface of the skull.

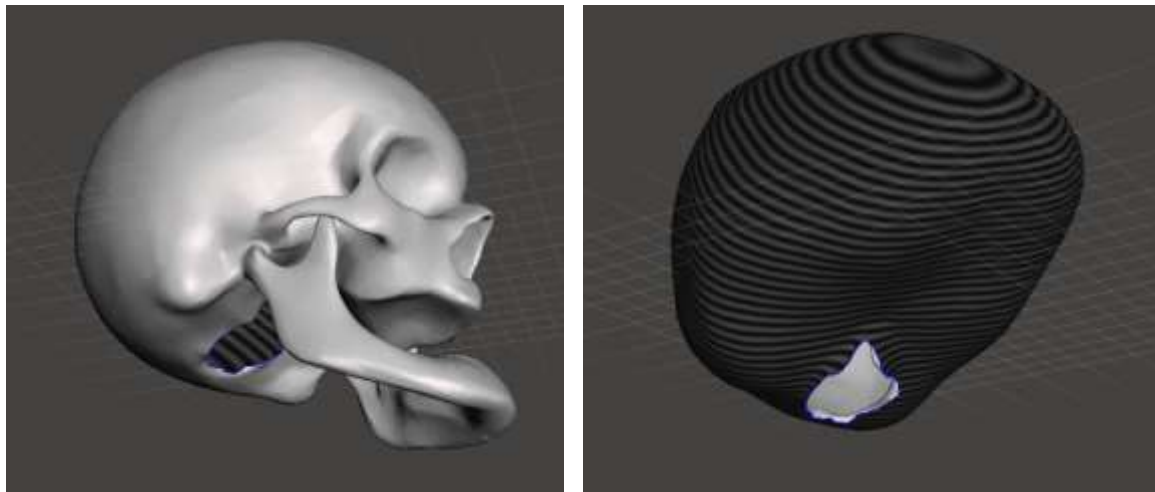


Figure 38. Separation of the original model into surfaces. On the left, the external surface of the skull and on the right, the internal surface of the skull.

Then, an inward thickness of 1 mm was attributed to each part. This thickness was chosen because, within the range of thicknesses studied by Chamrad et al. [36], this one resulted in a more realistic model compared to the thickness of 2 mm. After correcting some surface errors, such as holes and intersections, the two parts were exported to another open-source software called Meshlab.

Meshlab [106] is also used to work with surfaces in a 3D environment and has two useful tools for this work. One corrects intersections and the other simplifies the model's STL mesh. Although the intersections were corrected initially in MeshMixer, Meshlab can identify some new intersections, so this tool is used again. On the other hand, if the number of triangles to describe the generated surface is very high (which can lead to unnecessary computer overload) the part can be simplified,

so a simplification to make the model functional with the care to not diminish the geometric rigor of the model was made.

Then, it was necessary to transform the corrected meshes into solid parts (Figure 39) so that it could be used in Solidworks. For this purpose, FreeCAD software was used, a 3D parametric CAD modeler, multiplatform, and open source.

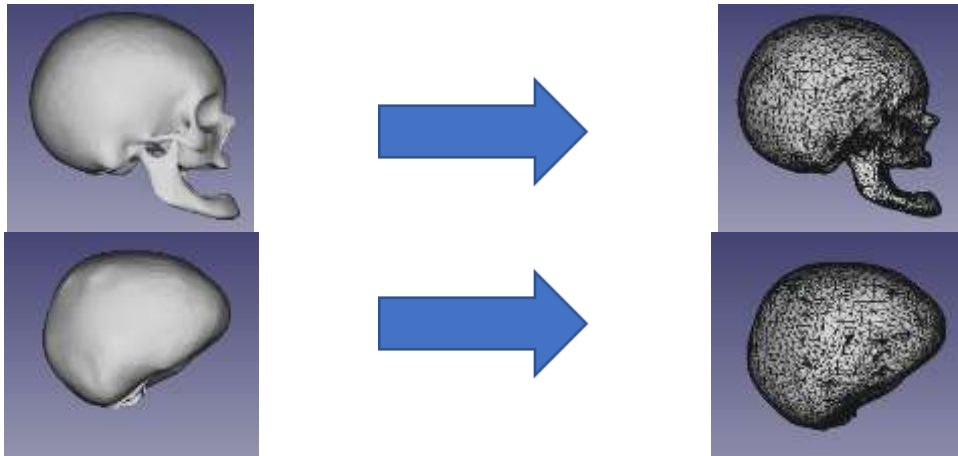


Figure 39. Transformation of the STL meshes into solid parts in FreeCAD software. On the left figures the meshes can be seen and on the right figures their respective solid parts.

The solids were transferred to SolidWorks, an assembly was opened with both 1 mm thick outer and inner parts of the skull and a solid cube was created that involved both parts. A tool called Cavity was used, which, as the name implies, creates a cavity in the shape of the design part in the base part of the mould. In this case, the base part of the mould will be the cube and the design parts will be both the internal and external parts of the skull, creating a part that contains the geometry of the trabecular bone, seen in Figure 40.

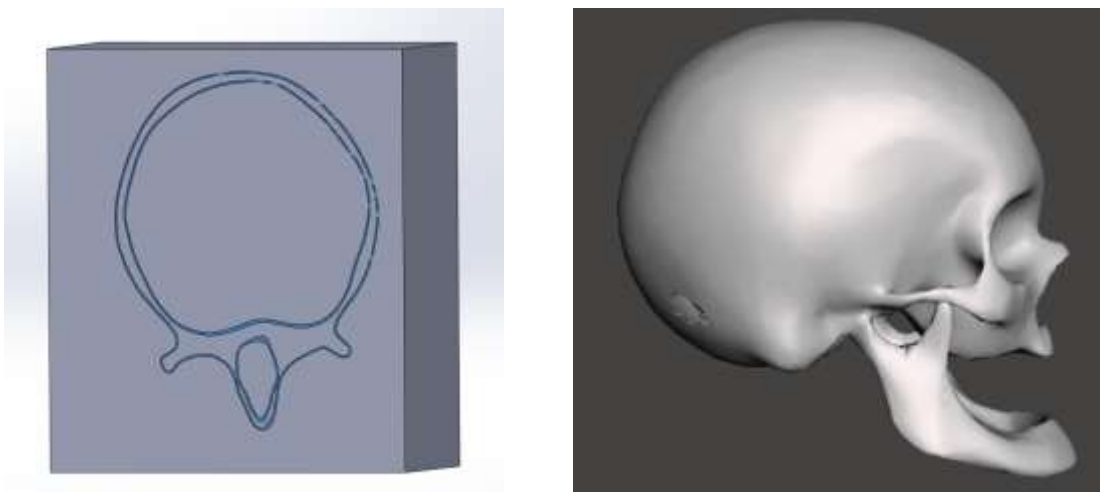


Figure 40. Obtaining the trabecular bone from Solidworks. On the left, an axial sectional view shows various parts of the assembly and on the right, the visualization of the trabecular bone.

Afterwards, the trabecular bone was transferred to Meshmixer (Autodesk, USA) and MeshLab (ISTI-CNR, Italy). Geometrical errors, such as holes and intersections, were identified and eliminated. FreeCAD (The FreeCAD Team, USA) was used to obtain the geometry of the final trabecular bone. Altogether, 6 holes of varying dimensions were filled, as shown in Figure 41. This step was necessary so that a uniform layer for the entire skull could be created and it was considered that this would not cause significant errors in the final results of the simulations because the location of the holes is in areas not interesting to investigate or in locations hard to hit thanks to the human anatomy. Additionally, the difference in volume before and after the correction is irrelevant (difference of 0.16%).

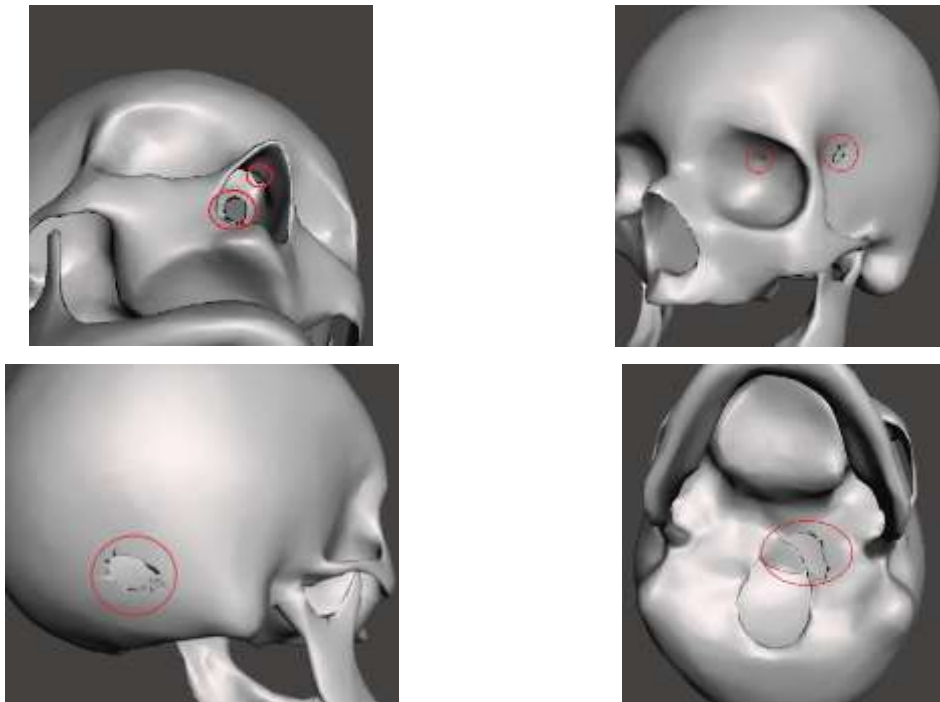


Figure 41. Visualization of all the filled holes to create the part of the final trabecular bone.

Given the fact the final goal is to create a skull model with hexahedral elements and Abaqus mesh algorithm is not capable to do so, thanks to the geometrical complexity of the model, the next step was the modelling of the trabecular component in HyperMesh (Altair, USA). This software is a finite element pre-processor with many tools for creation and edition of complex meshes, with powerful mesh generator algorithms. The aim is to create a hexahedral mesh in this software and then import it to Abaqus to run the model in its solver.

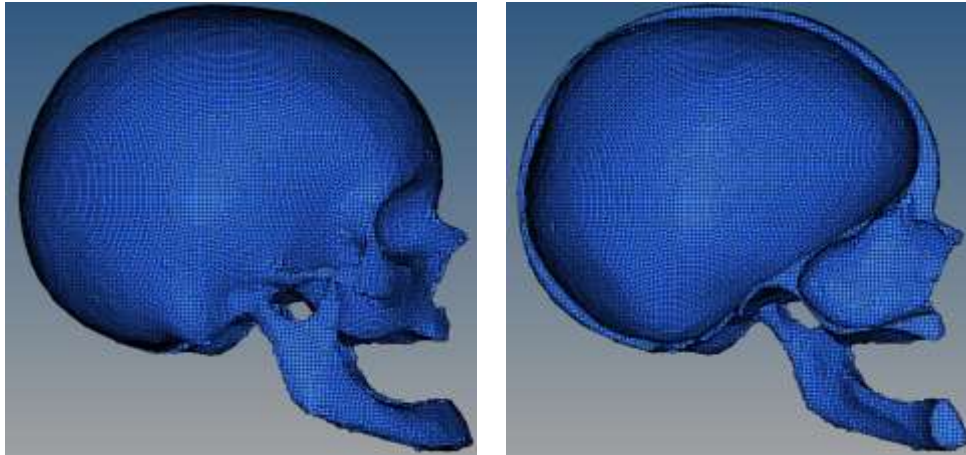
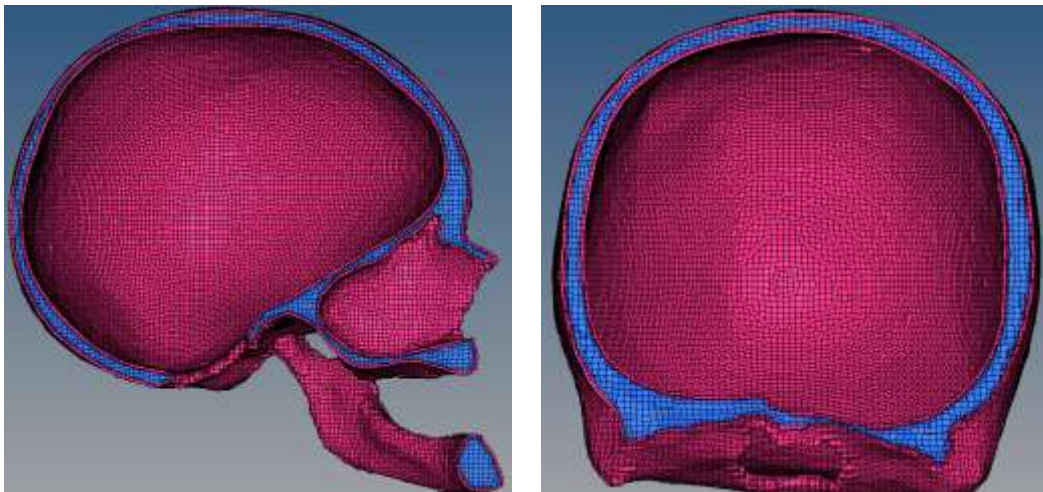


Figure 42. Visualization of the initial component created in HyperMesh for the trabecular bone.

First, a component constituted with hexahedral elements was created for the trabecular mesh, as seen in Figure 42. The mesh generation was controlled by setting two parameters, the desired element size of 2 mm [101] and a minimum Jacobian of 0.3 as parameters, to ensure acceptable elements aspect ratios. Those specific parameters were defined to guarantee convergence while diminishing the overall CPU cost on further simulations.

After that, to create the cortical section of the skull, a shell of the trabecular component was created, which acted as a base to create the 1 mm cortical solid component. One final note, after some simulations, it was found that the cortical part needed to be thicker considering realistic material properties (Figure 62). In the literature, it was possible to confirm that depending on the location, the cortical layers vary between 1 and 2 mm [28]. So, a thin superficial layer of the trabecular component was adjusted to the cortical one. Thus, the outer dimensions of the skull were kept and the final cortical component thickness averages around 1.5 mm (Figure 43).



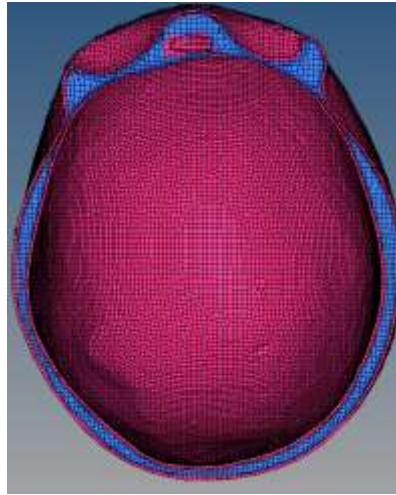


Figure 43. Sagittal, coronal and axial cross-sections of the model with 1.5 mm cortical layers and with a core of trabecular bone.

Overall, the mesh element quality is good and faithful to the geometry. However, around 245 elements were identified as bad quality elements (Jacobian inferior to 0.2) and 584 elements had intersection/penetration issues with other elements. Note that some of these elements had both problems as seen in Figure 44. These were manually edited and thus, those problems were corrected, obtaining a high-quality mesh that respects the aimed geometry. Additionally, given that only a small number of elements had problems (0.35%) and that those elements were for the most part situated in non-critical areas for cranial impact simulations, it was clear that these changes would not negatively affect the desired simulations.

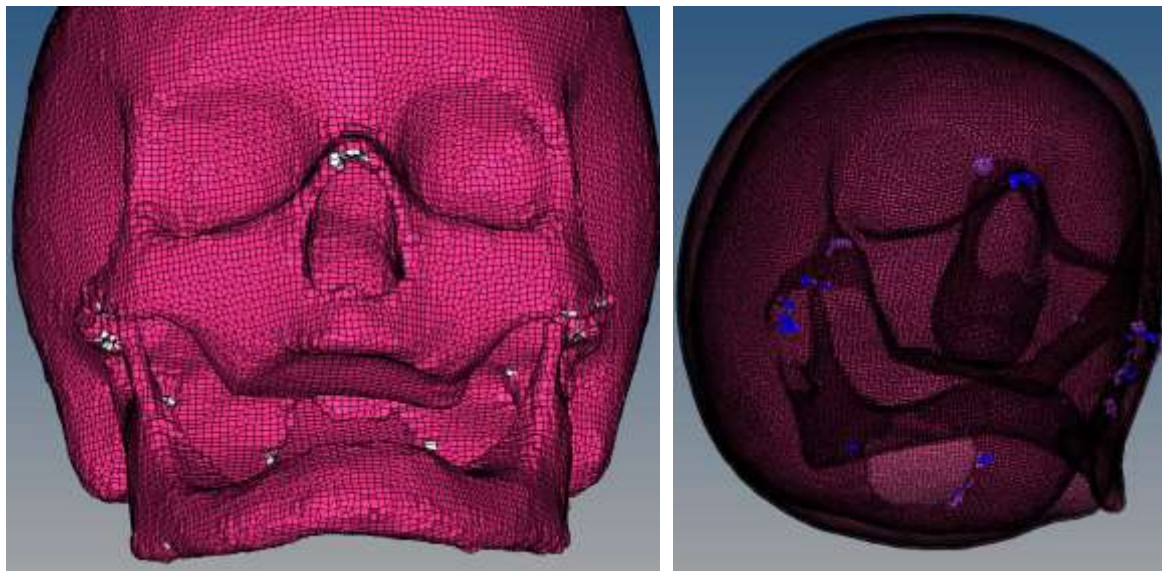


Figure 44. Problematic elements found. On the left, the elements with bad Jacobian highlighted in white and on the right, the elements with intersections highlighted in blue.

Lastly, the two components were segmented to create a component of cranial sutures, using reference images from a digital 3D atlas called “The Human Brain, Head and Neck in 2953 Pieces” [107], like the ones seen in Figure 45. The reason why only the cranial sutures were modelled is related to the focus of the investigations and the simulations. Additionally, the precision necessary to differentiate between all the facial bones is excessively time-consuming and thus, not worth it considering the overall gain. To each component was assigned a property so that when importing the part to Abaqus for further simulations, the final part would be sectioned with the 3 different components (trabecular, cortical and cranial sutures).

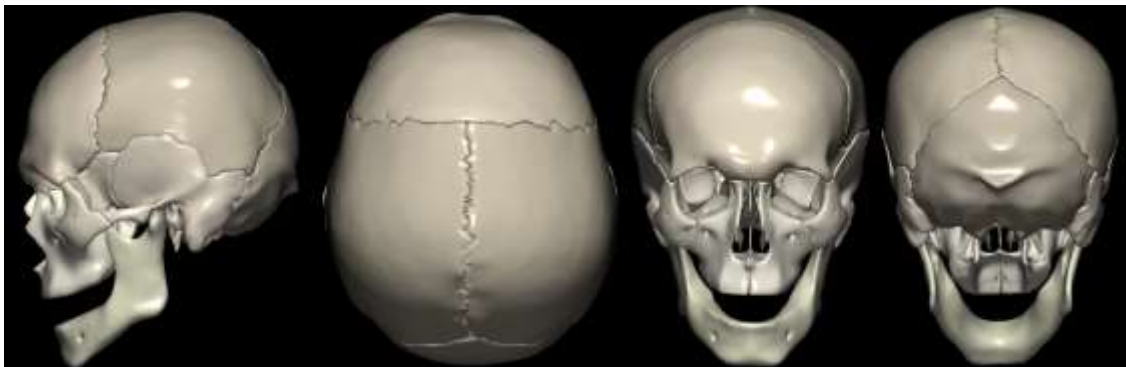
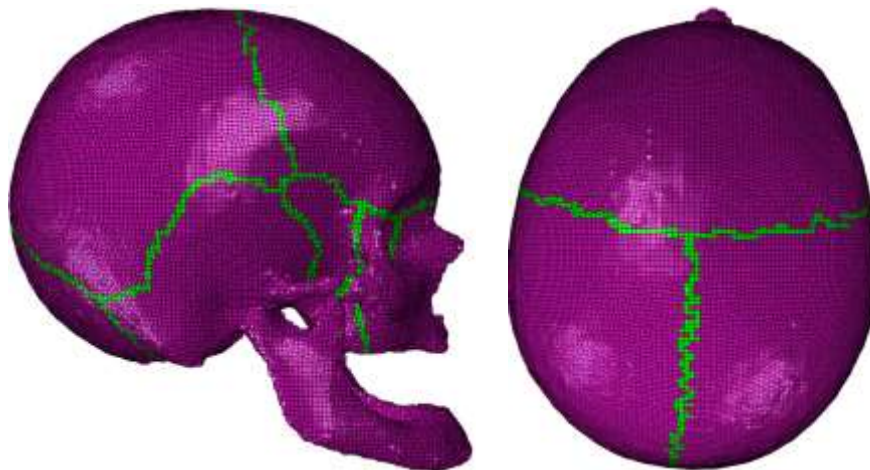


Figure 45. Reference images took from the 3D atlas utilized to create the cranial sutures [107].

At last, the model was imported to Abaqus for further modelling. The final model (Figure 46) is constituted of 3 components: a trabecular component with 92300 hexahedral elements, a cortical component with 133045 hexahedral elements and a cranial sutures component with 12271 hexahedral elements. Also, the interfaces between the components have shared nodes.



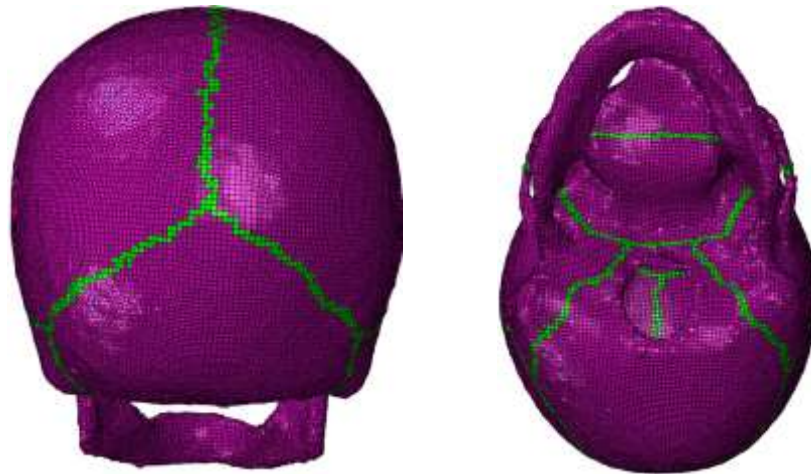


Figure 46. Visualization of the final complete model in Abaqus with trabecular bone, cortical bone (1.5 mm) and cranial sutures.

3.2 Material Modelling of the Skull

In this work, three different bony structures were modelled: cortical bone, trabecular bone and cranial sutures. They were modelled with material models available in Abaqus material library.

3.2.1 Trabecular bone material model

The trabecular or spongy bone was modelled as an elastic-plastic material since from all the bones, this type behaves more like, as the name indicates, sponge between the cortical bone tables and without exhibiting an S-shaped stress-strain curve, typical of crushable foams. This model is also the most used one on the FEHMs available in the literature, as shown in Table 8. The compression tests performed by Boruah et al. [108] were used to fit the model in Abaqus. Figure 47 shows the stress-strain curve obtained by [108] and used in this work to characterize the material behaviour. In addition, the material was considered isotropic with a density of 1500 kg/m^3 , a Poisson's ratio of 0.05 and a Young modulus of 1000 MPa, values found throughout the literature and used for example in the SUFHEM [93].

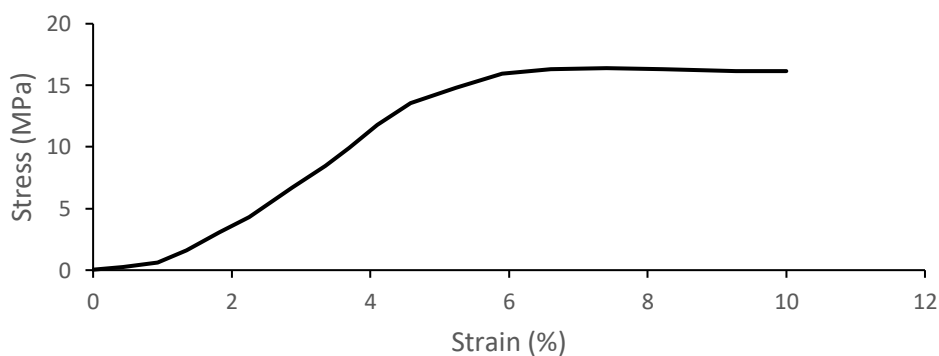


Figure 47. Stress-strain behaviour of trabecular bone under compression loading [108].

3.2.2 Quasi-brittle material model (cortical and sutures)

Based on the information found in the literature regarding the cortical bone and sutures, knowing that these types of tissues function as a quasi-brittle material, a material model capable of simulating brittle fracture is necessary. Abaqus provides a material law named brittle cracking to model the brittle behaviour of materials such as ceramics and concrete. The removal of elements based on a brittle failure criterion is also employed. The mechanical behaviour described by this model is driven by two stages: prior to and after cracking, as seen in Figure 48. Prior cracking, a linear elastic material model defines its mechanical behaviour, as described by Equations 1 and 2 in the particular case of isotropy (which was the used one on this work). The elastic behaviour values chosen to both cortical bone and cranial sutures can be seen in Table 19.

$$\sigma = D^{el}\epsilon^{el} \quad (1)$$

$$\begin{Bmatrix} \epsilon_{11} \\ \epsilon_{22} \\ \epsilon_{33} \\ \gamma_{12} \\ \gamma_{13} \\ \gamma_{23} \end{Bmatrix} = \begin{bmatrix} 1/E & -\nu/E & -\nu/E & 0 & 0 & 0 \\ -\nu/E & 1/E & -\nu/E & 0 & 0 & 0 \\ -\nu/E & -\nu/E & 1/E & 0 & 0 & 0 \\ 0 & 0 & 0 & 1/G & 0 & 0 \\ 0 & 0 & 0 & 0 & 1/G & 0 \\ 0 & 0 & 0 & 0 & 0 & 1/G \end{bmatrix} \begin{Bmatrix} \sigma_{11} \\ \sigma_{22} \\ \sigma_{33} \\ \sigma_{12} \\ \sigma_{13} \\ \sigma_{23} \end{Bmatrix} \quad (2)$$

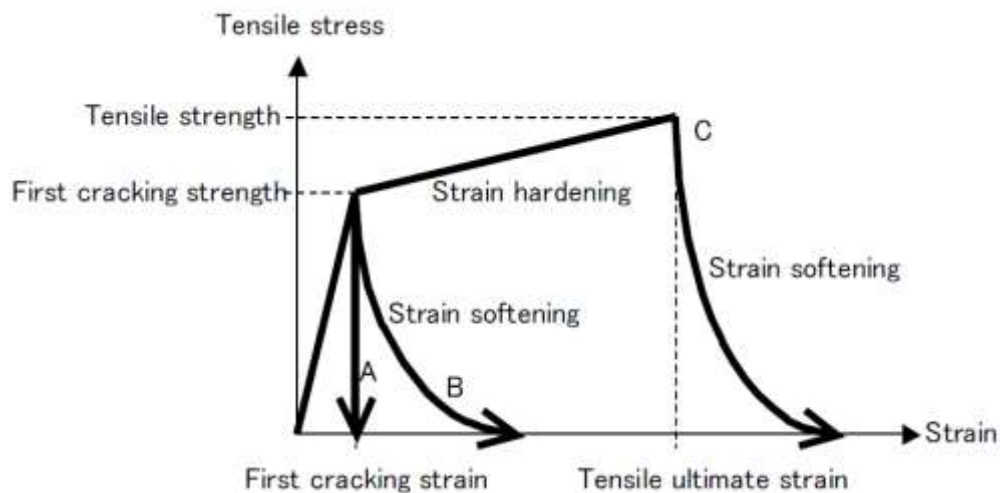


Figure 48. Definition of A: brittle, B: quasi-brittle, and C: ductile behaviour - strain softening and strain hardening under uniaxial tensile loading [29].

Tissue Type	Density (kg/m ³)	Young Modulus (MPa)	Poisson's Ratio
Cortical	1900	20000	0.21
Sutures	2100	15000	0.3

Table 19. The elastic behaviour values chosen to both cortical bone and cranial sutures.

To define crack initiation and the behaviour of bone tissue after cracking, three modules must be defined: a post-failure stress-strain relation, a shear retention model and a brittle failure criterion. The post-failure stress-strain relation defines the post-failure stress (σ_t^I) as a function of the strain across the crack (ε_{nn}^{ck}), modelling it after its initiation. Figure 49 shows the values used for both tissues.

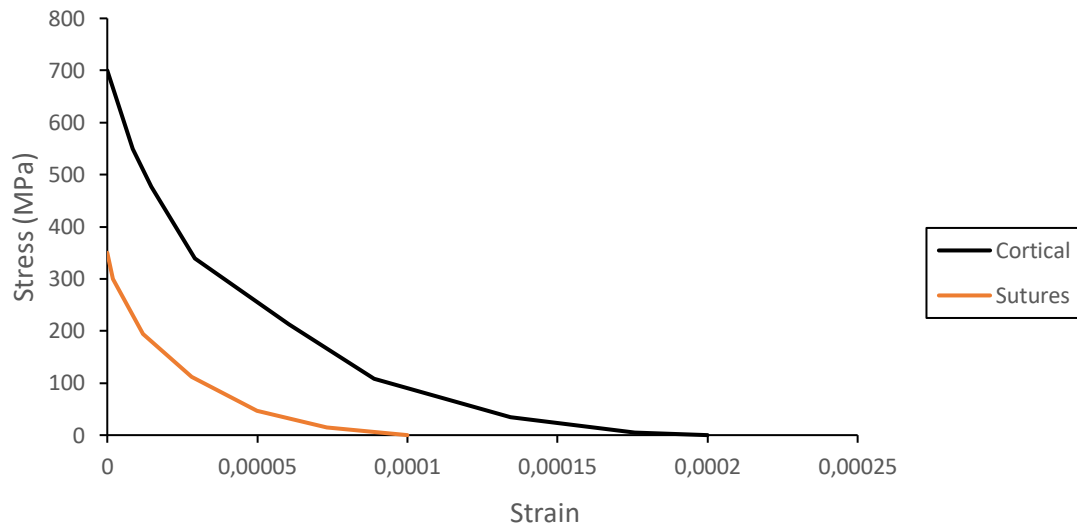


Figure 49. Post-failure stress-strain curve for both cortical and sutures tissues.

Regarding the shear retention model, it requires the definition of the post cracked shear stiffness as a function of the opening strain across the crack. This relation is defined by:

$$G_c = \omega (\varepsilon_{nn}^{ck}) G \quad (3)$$

where ε_{nn}^{ck} is the strain after cracking, ω is the shear retention factor and G_c is the cracked shear modulus. The last one reduces as the crack opens. Figure 50 shows the relation employed for the specific case both cortical and sutures tissues.

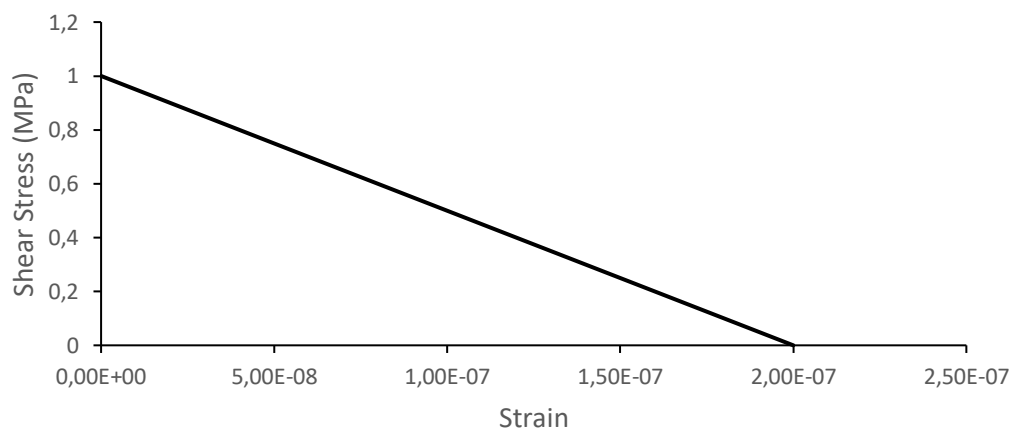


Figure 50. Shear retention model values for both cortical and sutures tissues.

The material cracking is defined by an often-used criterion to predict the failure of brittle materials, the Rankine criterion, which is based on the maximum normal stress and determines the crack initiation, deleting the corresponding element. The brittle failure criterion allows the definition of the number of local direct cracking strain components (maximum 3) at a material point and the failure strain to cause element failure. When the material point fails, all the stress components are set to zero. If all the material points in an element fail, the element is removed from the mesh. The number of material points required for element failure can be defined. In this case, for the cortical bone, one material point was set as the requirement for element failure with a direct cracking failure strain of 0.0006. Similarly, for the cranial sutures, one material point was set as the requirement for element failure but with a reduced direct cracking failure strain of 0.0004.

3.3 Validation methodology

3.3.1 Validation of the Trabecular Bone

For the validation of the trabecular bone, a uniaxial compression test conducted by Boruah et.al [108] was simulated. In this study, ten adult male post-mortem human surrogates were chosen to represent the 50th percentile adult male with an upper age limit of 70 years. All specimens were frozen post-mortem and unfrozen for use.

Skull clinical CT was used to identify ten anatomical locations on the right half of the calvarium for harvesting cores (Figure 51). The locations were chosen to avoid sutures. The locations of the harvested cores were precisely measured.

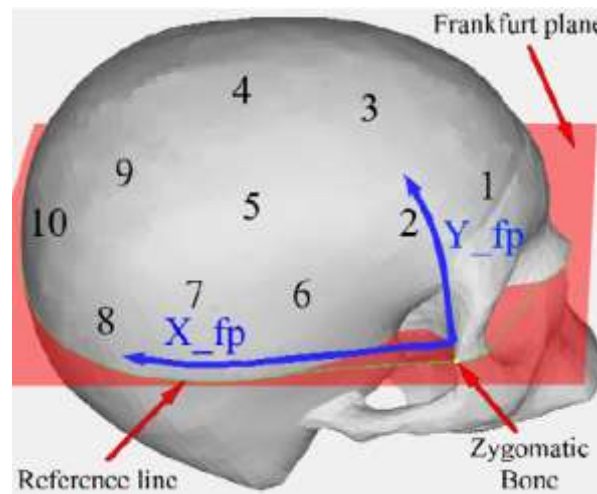


Figure 51. Harvest locations marked on the skull (1 up to 10). Also shown are the reference features and location measurement scheme [108].

After removal of the scalp, ten sites on the right side of the calvarium were identified and marked for harvesting cylindrical-shaped samples (Figure 52). This was guided by the rough designated locations identified from clinical CT and the avoidance of specific anomalies such as deformation and table curvature. The locations were then measured and recorded. Cores of through-the-thickness skull samples were obtained from the right half of the calvarium using a drill press (Figure 52). A

total of 98 cores with a diameter of 18.24 mm were obtained from the right calvaria of the ten subjects. Figure 53 shows a trabecular cored sample with the inner cortical table been seen on top.



Figure 52. Cores being drilled out of the calvarium using a vertical drill [108].

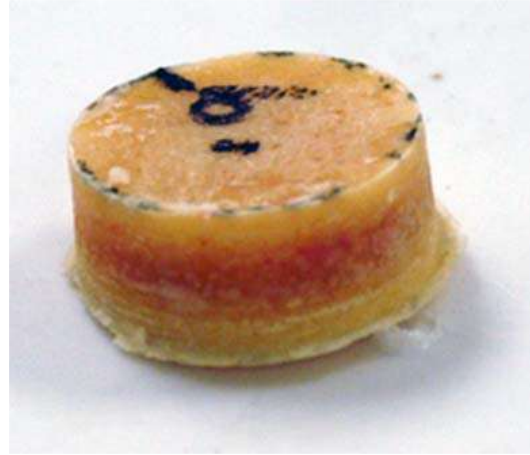


Figure 53. A cylindrical-shaped sandwich sample with trabecular bone in the core, and cortical bone in the tables (inner table on top) [108].

All the cores were imaged prior to testing using a scanner with an isotropic resolution of 30 μm . The thickness of the three layers of the cores was measured by observing the onset of trabecular pores at four fixed 15 x 15 pixel windows on the slice image. Table 20 shows a summary of the measurements found in terms of means and standard deviations. After completion of μCT and before testing, the skull cores were potted in a minimal amount of polyester resin in order to provide two flat parallel surfaces for mounting the specimen on the test rig. For this reason, for simulation, it was decided to recreate the sample using the mean values obtained the study, given that the final sample in the study was flat. Boruah et.al [108] while comparing cortical thickness with the literature and found that this values are atypical, but since the objective is validate the compression of the trabecular and the tables in the studies have a mix between cortical bone and polyester their thickness was irrelevant.

	Thickness (mm)	Deviation (mm)
Outer Table	0.76	± 0.29
Inner table	0.35	± 0.15
Trabeculae	5.08	± 2.01

Table 20. Micro CT study results from Boruah et.al [93].

The compressibility test setup (Figure 54) consisted of the Instron 8874 servo-hydraulic system pushing vertically down on the potted core sample. The core specimens were loaded in the setup with the outer table facing the actuator of the Instron machine. A ramp displacement was then applied to the core outer table at a target rate of 15 mm/s. The Instron control system was

programmed to unload the machine when a force of 6.5 kN was reached. This was done to prevent any damage to the test equipment. Both the simulation and study results can be seen this Chapter 4.

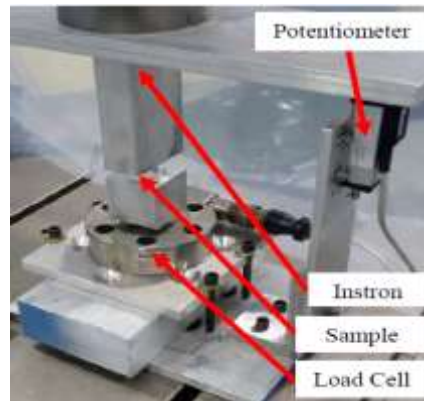


Figure 54. Skull core compression test setup [108].

3.3.2 Validation of Skull

For the validation of these two types of tissues, two experimental tests were simulated with direct hits on cortical and sutures structures. In the literature, no study was found addressing experimental testing solely on sutures without the influence of cortical, and vice-versa. Therefore, since the trabecular bone was validated following the experiment presented in the previous section, the remaining bony structures were validated by simulating skull blunt trauma and falls. Additionally, to validate the behaviour of the damage/failure models, another experimental study was simulated, comparing the fracture patterns.

3.3.2.1 Yoganandan et. al [67] Skull Vertex impact experiment

Yoganandan's [67] experiment, as shown in the literature review above, is an experiment where 21 specimens were loaded at quasi-static and at dynamic rates. From these tests, a specific test, specimen number 7, was chosen to be recreated on a simulation. This particular test consisted of a dynamic rate test where a projectile with 96 mm of diameter and a mass of 1,213 kg impacted on the vertex of the skull (on the sagittal sutures) at 7.2 m/s. This one was chosen because the impact location contained for the most part sutures and also because force-deflection curves were given for it in Yoganandan's et. al [67] paper. Results of the simulation can be seen the Chapter 4.

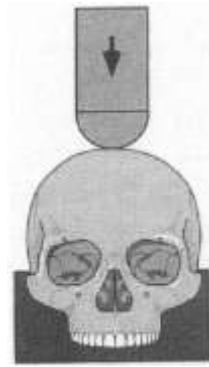


Figure 55. Schematics of the specimen orientation in the fixation device and the external load (shown by dark arrow) [67].

3.3.2.2 Yoganandan et.al [109] Lateral Head Impact experiment

In this study, post-mortem human subjects were used to impact the lateral side of the cranium. The unembalmed specimens were isolated at the level of the occipital condyles, maintaining the integrity of the entire cranial vault and brain.

Three linear accelerometers at each site/region were rigidly fixed onto a metal cube, that was then rigidly mounted to a contoured plate, and the plate was attached to the cranium using screws at each corner. The test matrix consisted of repeated tests on the same specimen.

The specimens were impacted using drop techniques with successively increasing input energies until fracture, a decrease in force occurred with increasing impact velocity, or the impact force was closer to the rated limit of the load cell. A 40-durometer padding (50 mm thickness) material served as the impacting boundary condition. The dynamic mode of loading was accomplished using free-fall (drop) techniques where the specimen was completely unconstrained. The schematic of the test setup is shown in Figure 56. Then, the FEHM can be validated by recording the accelerations at the three regions and comparing it to the results found in this study, it is to note that the resultant accelerations from the three accelerometers were filtered at 1000 Hz with the SAE recommended filtered so the results present in Chapter 4 regarding this study will also be filtered at 1000 Hz using Abaqus's `saeGeneralFilter (xyData= , cutoffFrequency=)` filter.

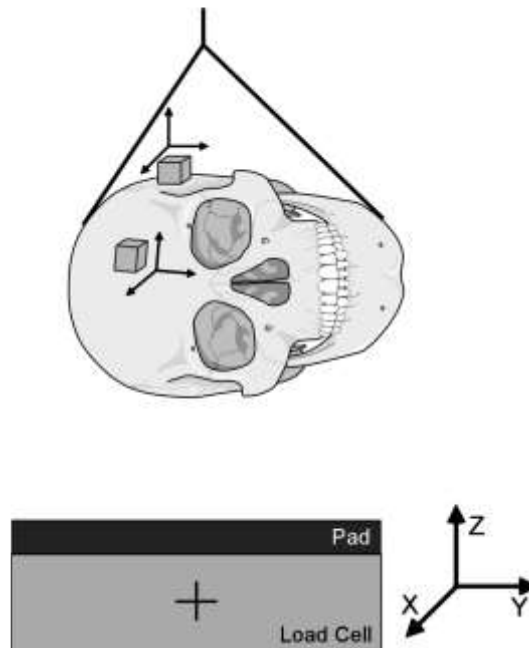


Figure 56. Schematic of Yoganandan's et.al [109] test setup.

3.3.2.3 Huang's et.al [101] Experiment

This experiment, similarly to Yoganandan's [67], was already described in the literature review. In summary, Huang et. al [101] performed two blunt ballistic temporoparietal head impacts carried out on a post-mortem human subject. A rigid, flat-faced 38.1 mm diameter projectile/impactor with a mass of 0.1 kg was used for all impacts. The impactor was aligned so the contact face struck the specimen normal to the skin surface. Two impact conditions were performed, one to each of the two bilateral temporoparietal regions. Condition A was performed at a target velocity target of 20 m/s to the right side while condition B was targeted for an impact velocity of 35 m/s to the left side. To validate the model, it will be simulated both conditions, and especially condition B since fractures patterns are provided for this case.

In the experiment the entire head of the specimen was used. Therefore, it was necessary to do the same in the simulation, assembling the intracranial components of YEAHM to the skull model developed in this work.

3.4 YEAHM model + New Skull model

After the creation of the skull model, the various parts previously made belonging to the YEAHM model were assembled in Abaqus, namely the brain, the CSF, the BVs and the SSS. For this purpose, during the creation of the skull, special care was taken to have the same coordinate system and origin for the new skull in order to be able to assemble the various components without additional problems like intersections between elements.

The Skull + Brain+ CSF + BVs & SSS system was assembled and can be seen in Figure 57. Overall, the model contains 1202015 elements, of which 20 % (237616) form the skull.



Figure 57. Representation of the Skull + Brain+ CSF + BVs & SSS final assembly. Cut views in the 3 main planes, from left to right: sagittal, frontal and transverse planes.

Chapter 4

Simulations and Results

All the simulations performed were dynamic explicit analysis. The explicit analysis cost rises only linearly with problem size, whereas the cost of solving the nonlinear equations associated with implicit integration rises more rapidly than linearly with problem size. With the explicit analysis, it is possible to solve complicated, three-dimensional contact problems with deformable bodies. However, since explicit analysis always converges to a solution even if that solution deviates from the correct one, the results need to be well analysed.

For all the simulations, the interaction between the parts was considered as frictionless general contact, this decision was made to reduce computation cost and because for most of the experiments, no friction coefficients are given and also because majority of the contacts are happening against metallic components with low rugosity and linear impacts, with no great place for tangential displacements.

To compare the various results from the simulations with the experiments available in the literature, the acquisition of the experimental data in form of curves was carried out with application WebPlotDigitizer [110], which can then be imported to Excel for further use.

4.1 Validation and discussion

4.1.1 Trabecular experiments – local material validation

To simulate the compression of trabecular bone and validate the constitutive strategy and material properties employed for trabecular bone, a cylindrical sample was developed based on the average measurements, for outer and inner tables and trabeculae, obtained in the Boruah et.al [108] study, reducing the probability of errors due to geometrical deviations. For this purpose, stress-strain curves were obtained to compare the results between simulations and experiments. From this validation the best trabeculae material model was composed of C3D8R elements with a mesh density of 2 mm without damage (Figure 59).

Similarly to the experiment, measurements of the skull numerical model, in what would be the same skull locations as in the experiment, were made to find out what parts of the skull have a higher degree of geometrical similarity with the computational model. Figure 58 shows the locations in the FEHM. The locations 1, 4 and 7 had the best fit regarding the samples average thickness of 6.19 mm, as can be seen in Table 21. Therefore, the stress-strain curves obtained for the three samples were the ones primarily used for the model validation.

Location	1	2	3	4	5	6	7	8	9	10
Skull Thickness (mm)	6.1	7.1	5.7	6.3	7.3	7.8	6.3	7.3	6.9	5
Difference from the average value of the study	0.1	0.9	0.5	0.1	1.1	1.6	0.1	1.1	0.7	1.2

Table 21. Model thickness measurements in different skull locations.

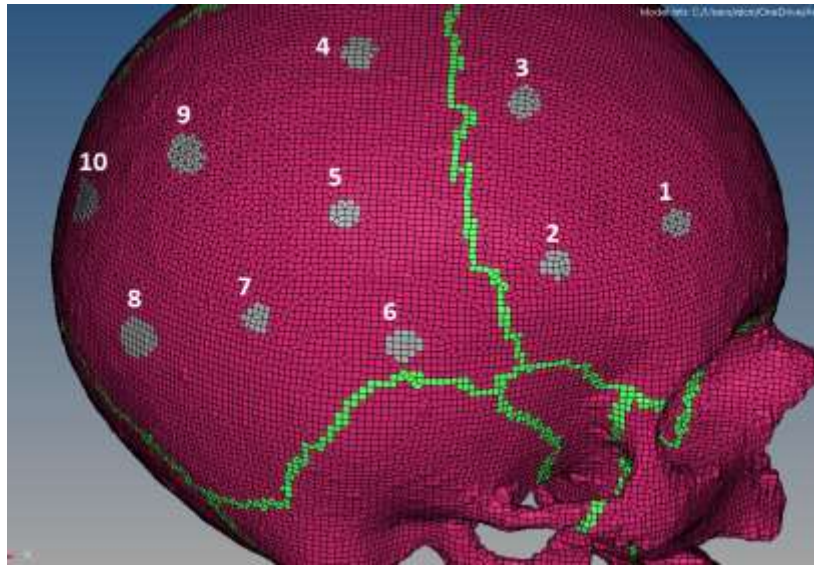


Figure 58. Locations of the samples in the FEHM, numbered and highlighted in grey.

An element type analysis was made to find the best formulation possible for the trabeculae between C3D8 reduced, complete and incomplete and it was found that the C3D8R prevailed with the best results. A mesh density analysis was made for each of the 3 elements types with 0.2, 0.5, 1 and 2 mm, to ensure that the average element size for the trabeculae in the model was a good fit with the experiment results. These results can be seen, altogether, in Figure 59.

Another analysis was made to compare between a trabeculae material with damage, without damage and with unloading for the 2 mm C3D8R model, for comparison to the experiment made in the study. The material properties were referred in the previous chapter except for the damage model. For that, it was used a ductile damage model with fracture strain of 0.1, strain rate of 1.17 [108] and a displacement at failure of 0.1, both fracture strain and displacement at failure were found through iteration. Results of this comparison can be seen in Figure 60.

With this, the compression behaviour of the trabeculae is deemed validated, and the material model (C3D8R) without damage will be the one used for the rest of the simulations.

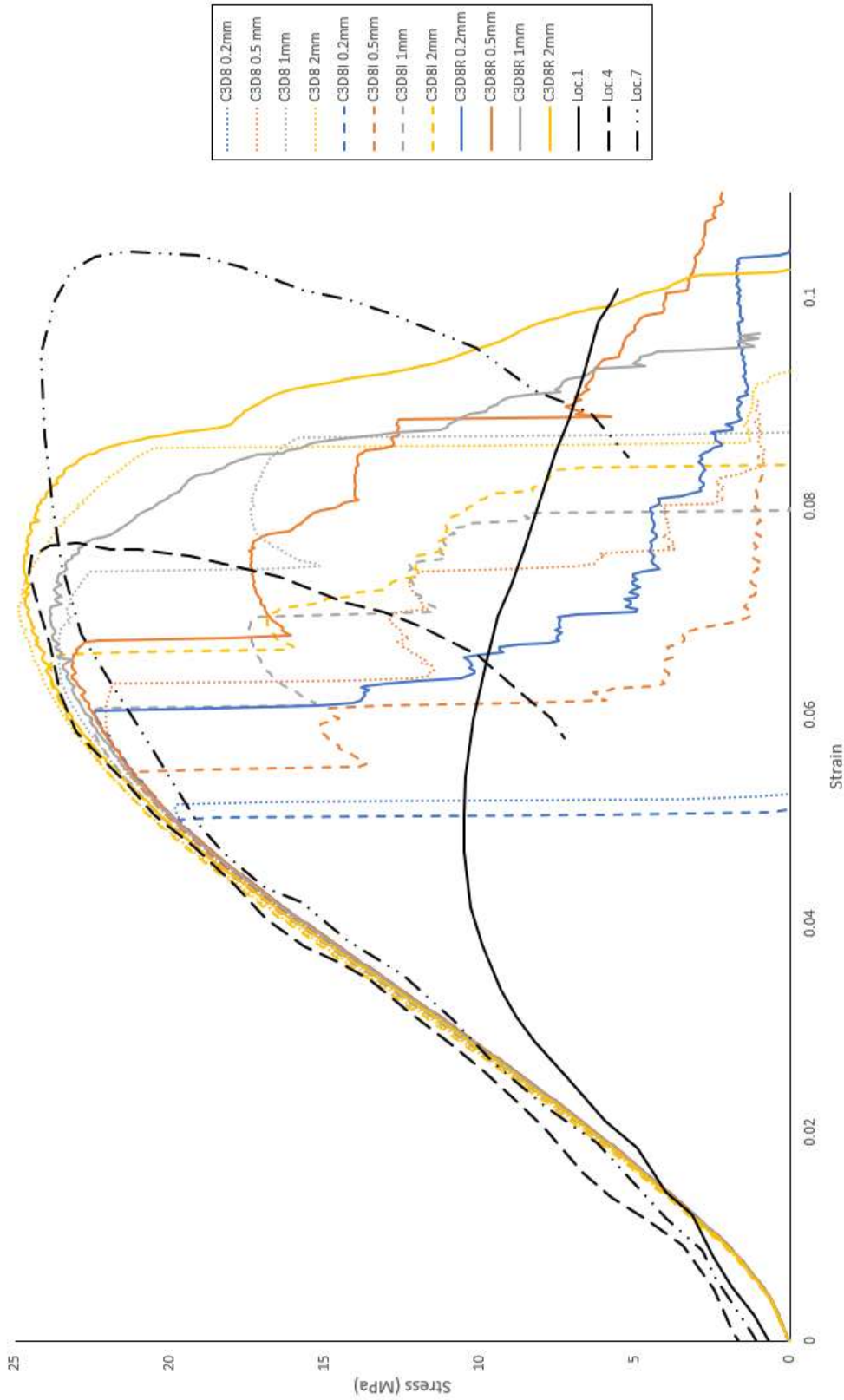


Figure 59. Element type and mesh density results with the 3 comparable location results.

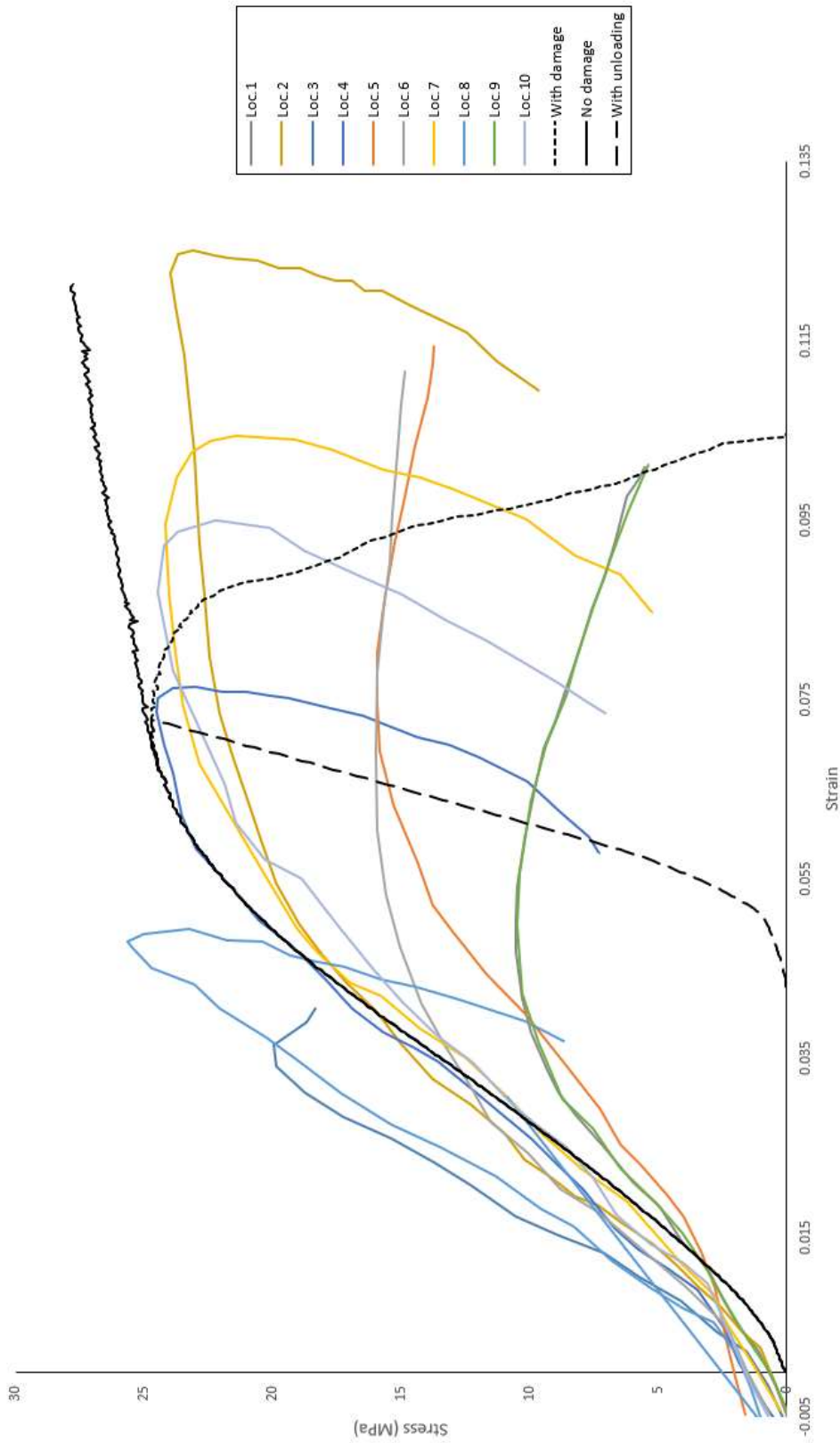


Figure 60. Differences between a model with damage, without damage and with unloading.

4.1.2 Skull Vertex impact simulation results

For this simulation, a rigid sphere with a diameter of 96 mm and 1.213 kg with an initial speed of 7.2 m/s was used as the impactor against the vertex of the skull. The bottom of the skull was fully constrained as referred in Yoganandan's [67] study, and its location in the model can be seen in Figure 61 as well as the impactor.

A preliminary analysis, with the same material model, was made to determine the proper element type for the cortical bone and the sutures. Figure 63 compares these simulations with the experiment. Overall, there is not a significant difference between the different types, concluding that the C3D8R would best suit the model since its behaviour at the end phase of the simulation better suited the experiment results. Figure 64 presents the results (force-deflection curve) of the simulation compared with the experiment.

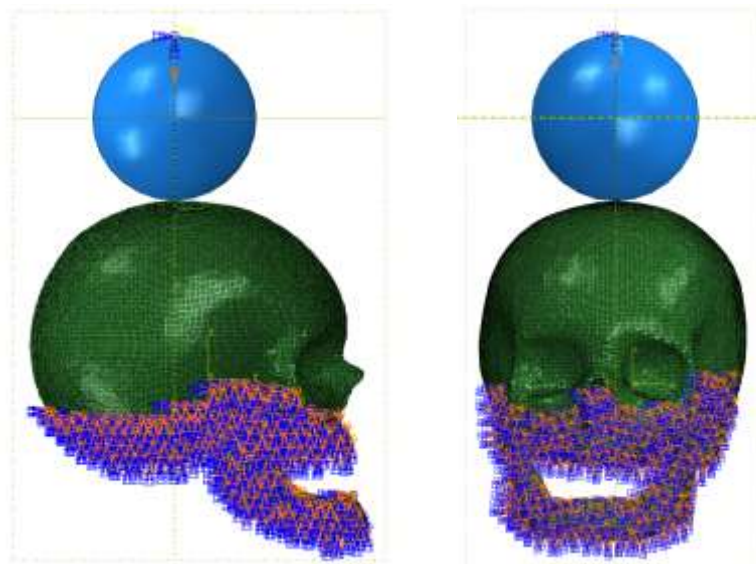


Figure 61. Visualization of the boundary conditions of the simulation from Yoganandan's [67] study. Left figure: sagittal view. Right figure: frontal view.

In the beginning, the intention was to create a model where the cortical bone had 1 mm of thickness because some of the literature [36] said that this value was the best when trying to create a cortical layer with the same thickness. It was in this simulation that it was found that a bigger thickness was needed and that is why the thickness was changed to approximately 1.5 mm. Actually, in the experimental literature, the average thickness was shown to be around 1 to 2 mm [28]. The reason behind this conclusion was that the only parameter that improved simulation results was the use of unrealistic Young modulus of both the cortical bone and the sutures, approximately 30 GPa for both. Thus, to have more realistic elastic material properties, the thickness of cortical bone was increases in half a millimetre per layer, which diminish these values to 20 GPa for the cortical bone and 15 GPa for the sutures. A comparison between these two different models with the final material model used can be seen in Figure 62.

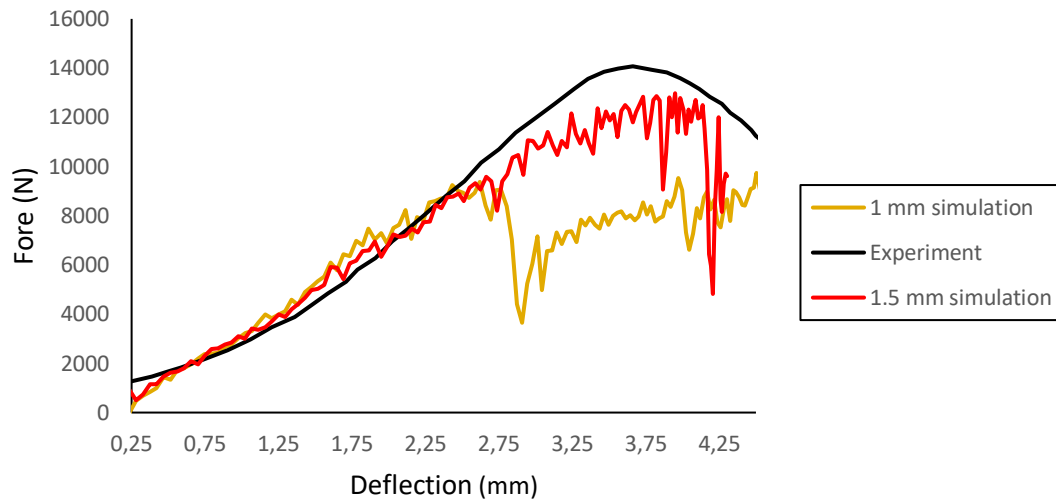


Figure 62. Comparison between the 1 mm and 1.5 mm cortical thickness results and the experiment, using the same material model.

The reasoning behind having to use a Young modulus of 15 GPa even though that on the literature the maximum value found was 3.6 GPa [22], it is related with the size of the elements. As was also found on the literature [19] that suture width averaged from 0.286 to 0.443 mm depending on the sutures, but the average width of the elements in the model is 2 mm with some places having more than one element width wise, knowing this the reason of having this big value is because the suture component in the model functions more like a combination of the 3 types of skull tissues (cortical, trabecular and sutures) than only as sutures.

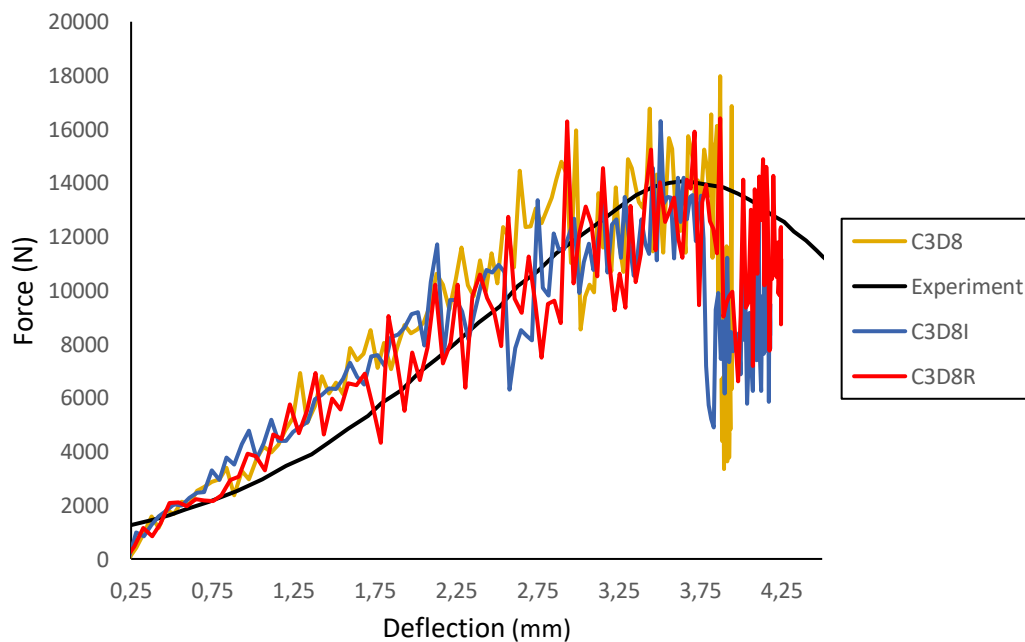


Figure 63. Comparison between element types for the cortical bone and sutures.

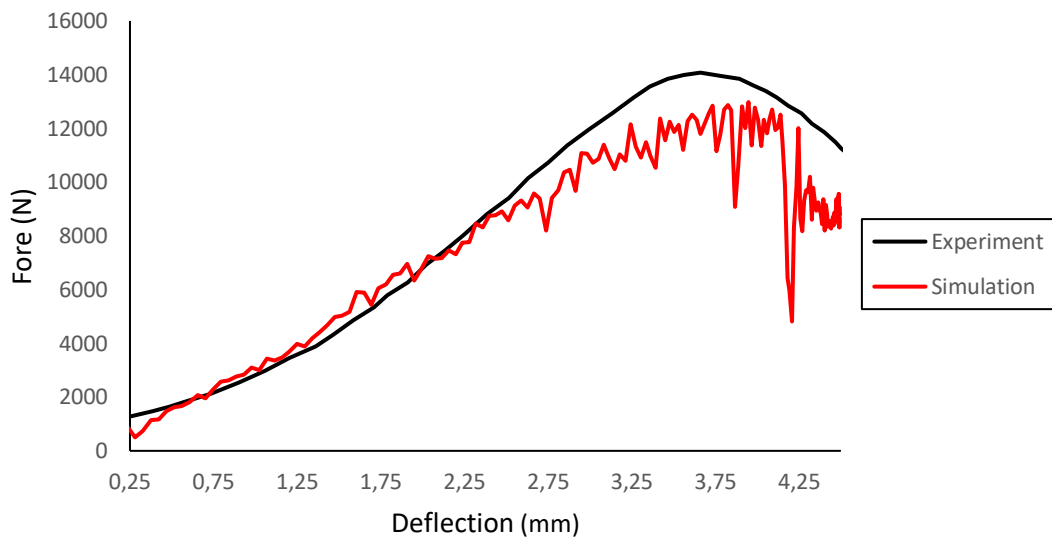


Figure 64. Results of the simulation compared with the experiment results.

4.1.3 Skull lateral impact simulation

Velocities of 6, 4.9 and 3.5 m/s were given to the head, so that it would be impacted against a 40-durometer neoprene [111] [109] padding (50 mm thickness) material laying on a rigid structure. For this reason, a material model for the pad was needed. Given that Yoganandan's et al. [109] study did not give any reference values of the material or its mechanical properties, only stating that it was a 40-durometer layer, data from ElGawady et. [112] and Sahoo et al. [113] were used. The first consists in a compression test performed on a 40 d neoprene pad and on the other study, Sahoo et al. [113] referred the density and Poisson's ratio used in the Yoganandan's [109] study. The pad was modelled as a Hyperfoam material with a density of 4320 kg/mm^3 , a Poisson's ratio of 0.43 and the uniaxial test curve shown in Figure 65. Comparisons between results will be done using acceleration curves of 3 different locations, by taking the average result of 10 nodes from each location (Anterior, Posterior and Contra-Lateral) in the skull using 3 different velocities said beforehand, these can be seen from Figure 66 to Figure 74 (the black continuous curves represents the mean value of the results, the dashed curves represent a one standard deviation from the mean results and the red curves represent simulation results).

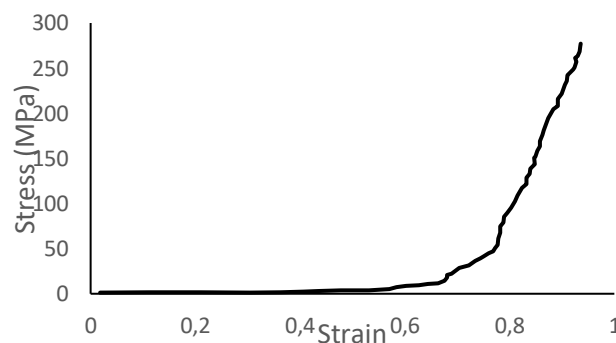


Figure 65. Stress-strain curve of the neoprene's compression uniaxial test [112].

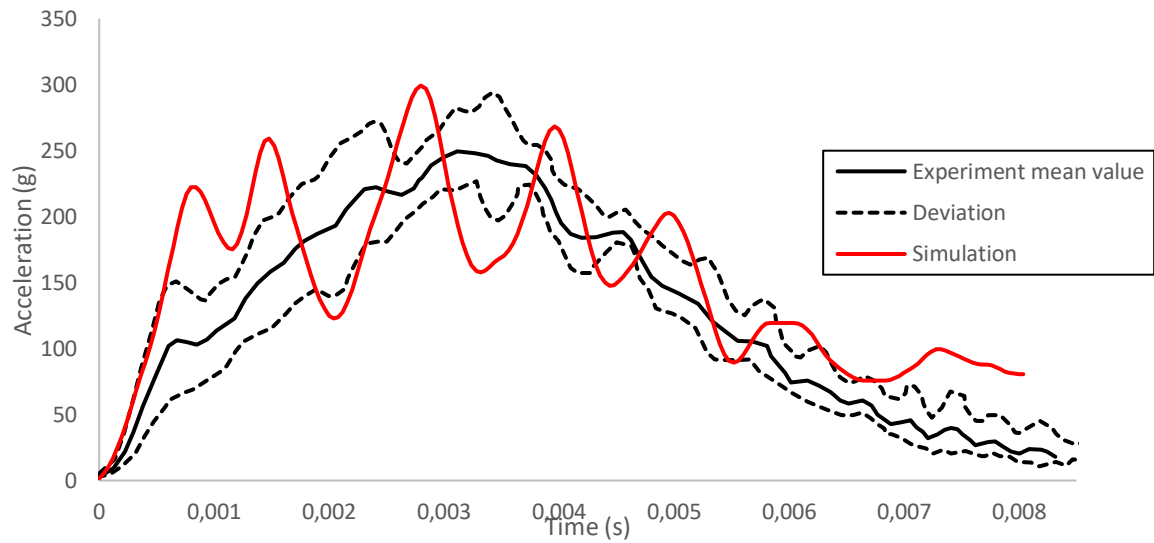


Figure 66. Contra-Lateral experiment acceleration response expressed as mean \pm one standard deviation at 6 m/s impact velocity with simulation results.

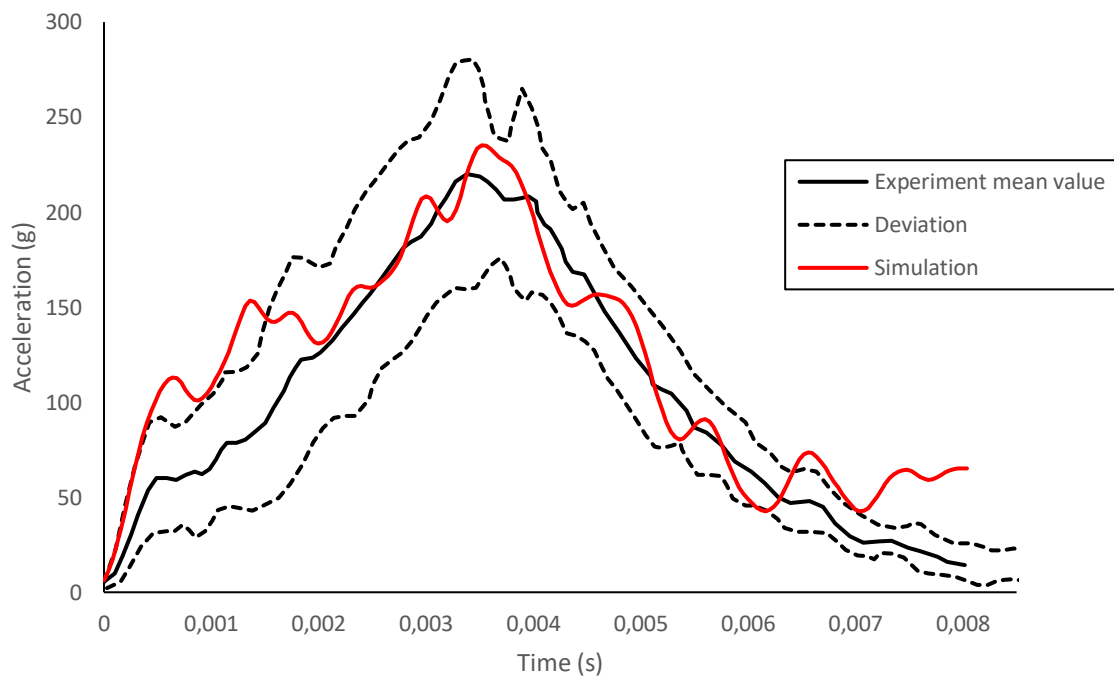


Figure 67. Anterior experiment acceleration response expressed as mean \pm one standard deviation at 6 m/s impact velocity with simulation results.

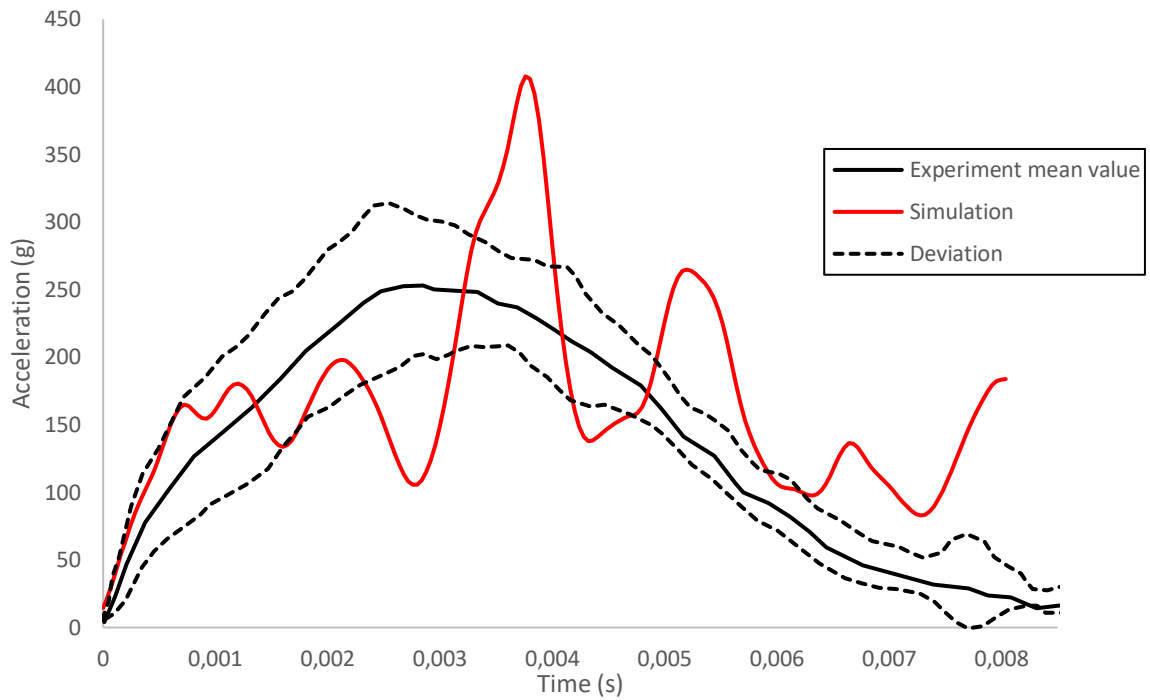


Figure 68. Posterior experiment acceleration response expressed as mean \pm one standard deviation at 6 m/s impact velocity with simulation results.

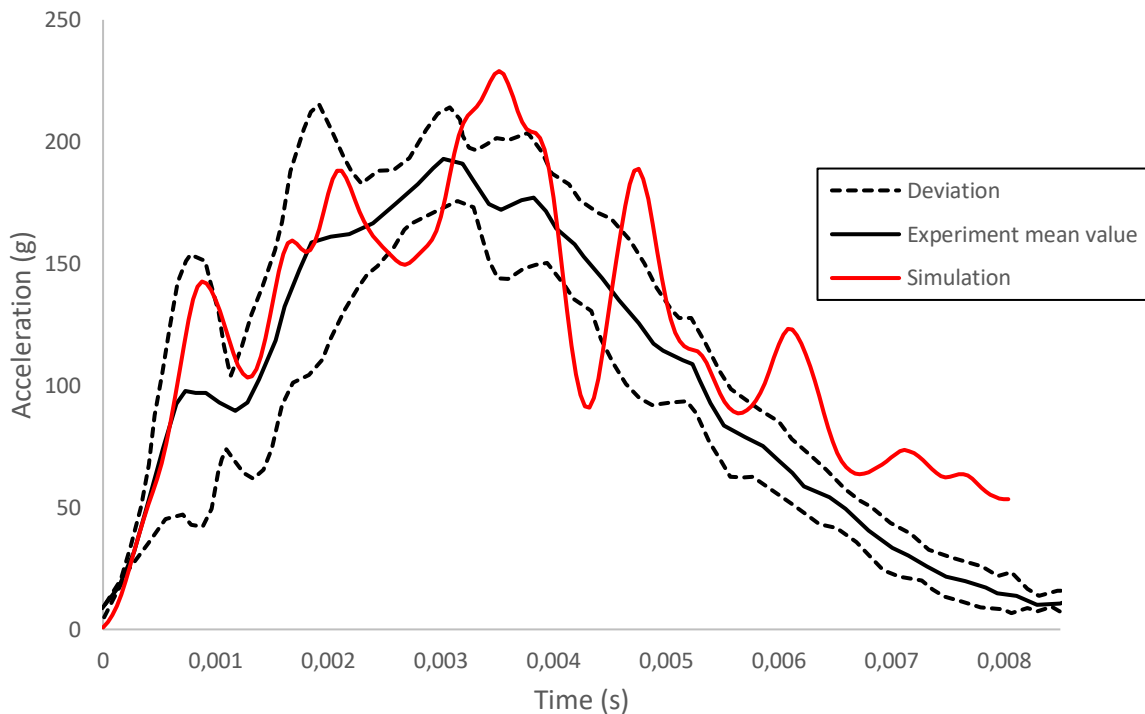


Figure 69. Contra-Lateral experiment acceleration response expressed as mean \pm one standard deviation at 4.9 m/s impact velocity with simulation results.

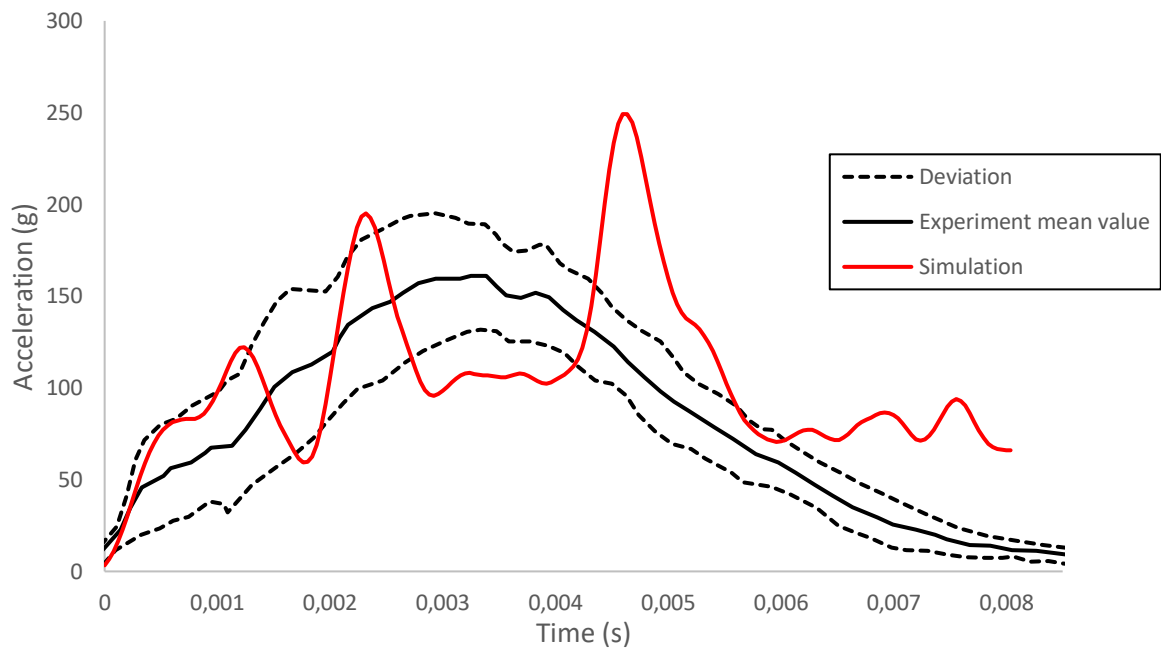


Figure 70. Anterior experiment acceleration response expressed as mean \pm one standard deviation at 4.9 m/s impact velocity with simulation results.

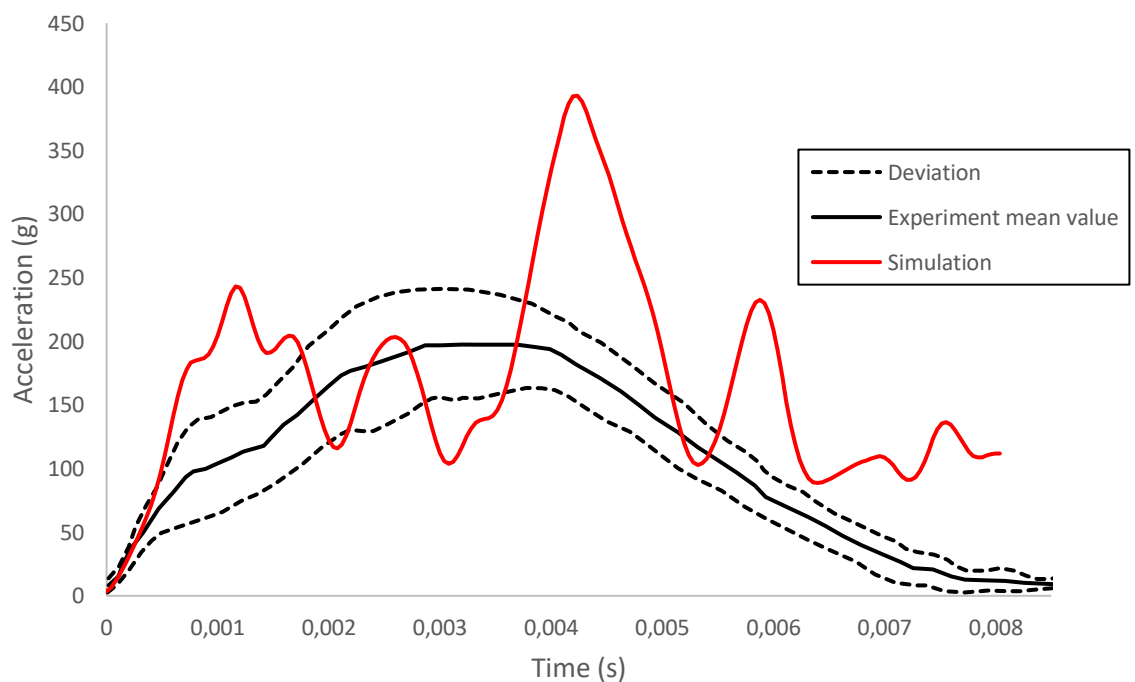


Figure 71. Posterior experiment acceleration response expressed as mean \pm one standard deviation at 4.9 m/s impact velocity with simulation results.

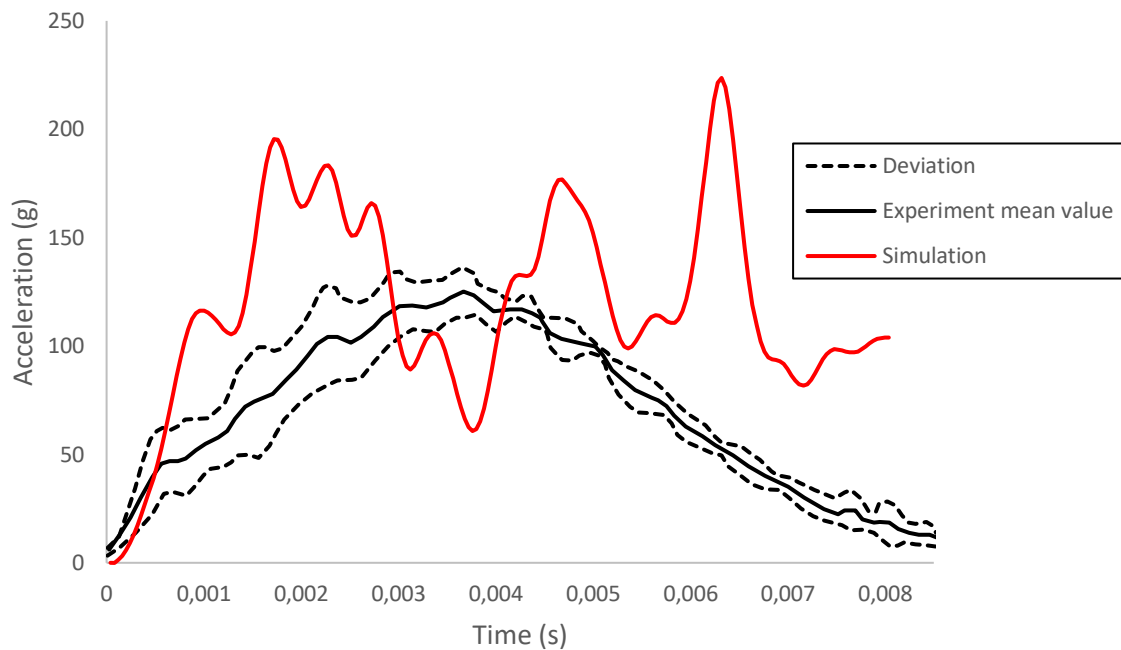


Figure 72. Contra-Lateral experiment acceleration response expressed as mean \pm one standard deviation at 3.5 m/s impact velocity with simulation results.

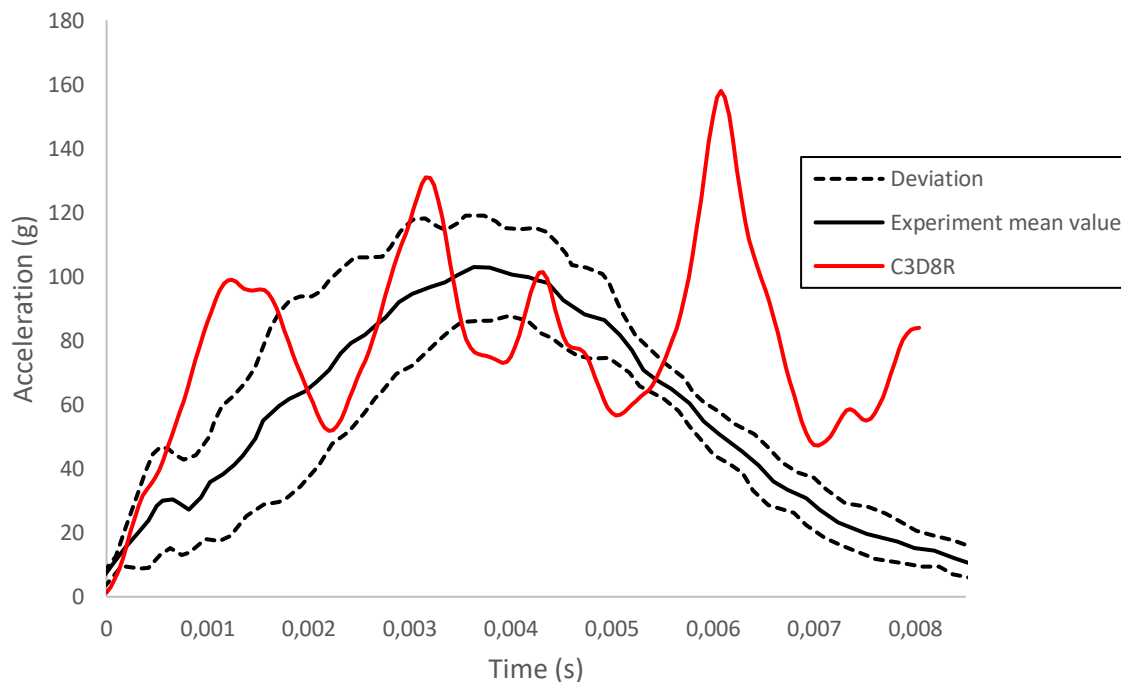


Figure 73. Anterior experiment acceleration response expressed as mean \pm one standard deviation at 3.5 m/s impact velocity with simulation results.

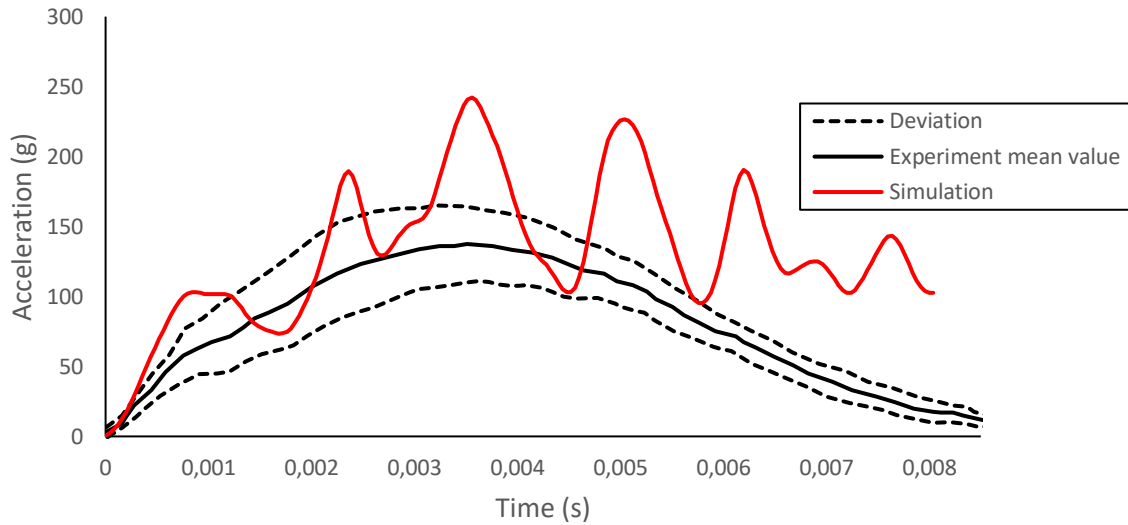


Figure 74. Posterior experiment acceleration response expressed as mean \pm one standard deviation at 3.5 m/s impact velocity with simulation results.

The results are excellent for the higher velocities but get worse with the reduction in speed. One of the reasons for this could be that even if the reduced formulation works well for higher velocities it might work bad for lower ones, for this reason a comparison between C3D8R and C3D8I can be seen in Figure 75 and Figure 76, which showed that this isn't the case. Another this might be because of the pad material model, which the material properties might be dependent of the strain rate, the properties that came from the literature may have been fine for the 6 m/s case but not appropriate for the 3.5 m/s case. Since there is not enough information in the literature regarding this point, it will be assumed that the material model of the pad is the major factor for the discrepancies between the simulations and the experiment results.

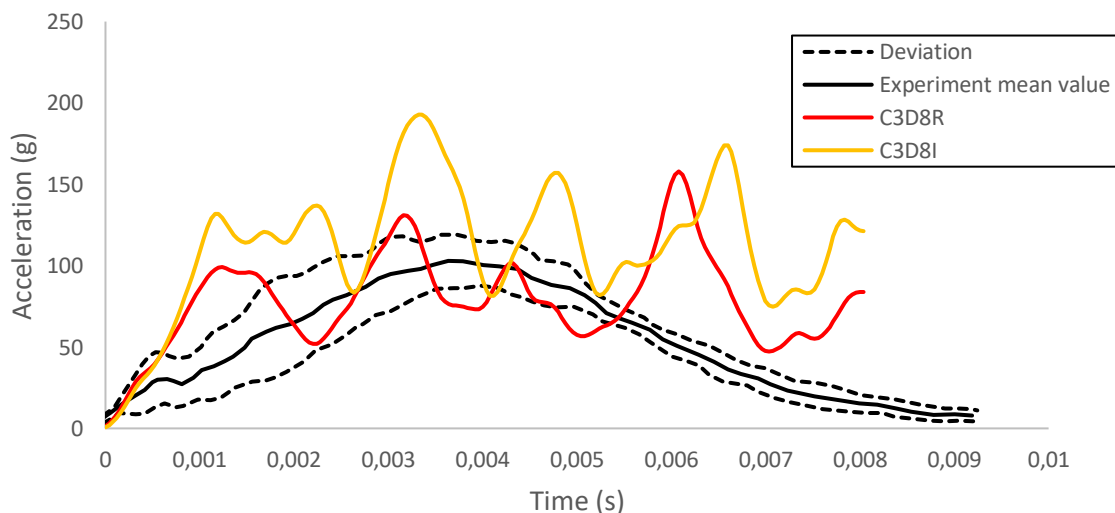


Figure 75. Comparison between the anterior experiment acceleration results, and the C3D8R and C3D8I results.

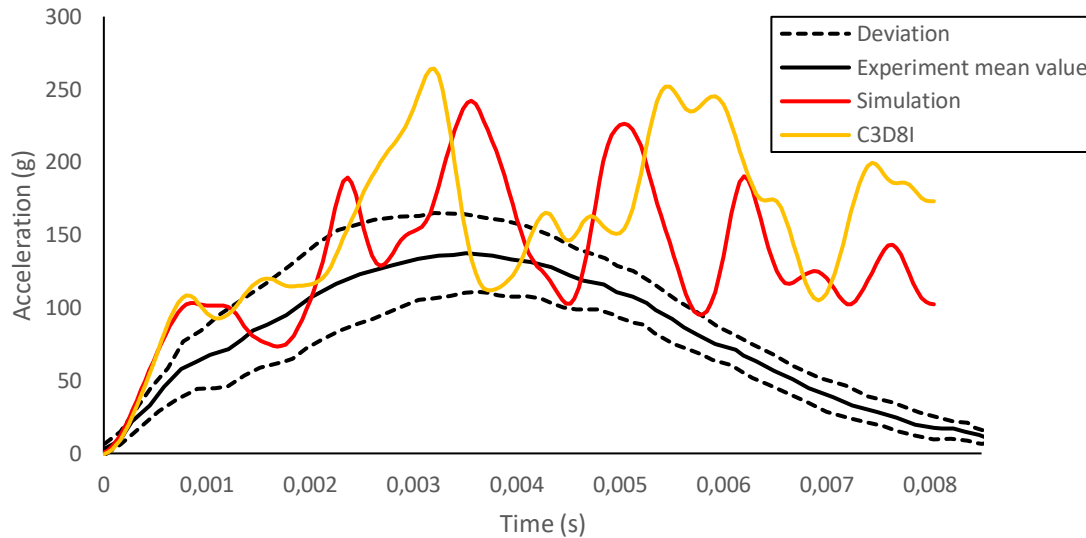


Figure 76. Comparison between the posterior experiment acceleration results, and the C3D8R and C3D8I results.

4.1.4 Huang's experiment - Fracture simulation

In this simulation, a cylindrical impactor with 38.1 mm of diameter and a mass of 0.1kg was modelled to recreate the impacts. Two impacts were performed, at 35 and 20 m/s, onto the temporo-parietal region, with a targeted impact point 25 mm anterior to the external acoustic meatus and 35 mm superior to the Frankfurt Plane, where the impact at 35 m/s caused a circular depressed fracture, contrary to the 20 m/s impact. Damage to the bone was only observed in the higher energy impact.

In the experiment, the entire head of the specimen was used, so in this simulation, the entire YEAHM model updated with the new skull model was used. The numerical setup can be seen in Figure 77. Just like the experiment, the head model was free to move, with no boundary conditions applied to it.

Figure 78 compares YEAHM's response and fracture pattern with both experimental and numerical results obtained by Huang et al. [101]. As can be seen, the results obtained using this model created a similar depressed fracture to Huang's study, with a diameter of 43 mm vertically and 48 mm horizontally. The results with this model were closer to the experiments than the numerical model of Huang et al. [101], fitting perfectly one of the dimensions of the depressed fractures, and achieving another dimension closer to reality. However, in this direction (horizontally), the difference was still significant.

One of the possible reasons for the discrepancy in horizontal measurement is that in the study Huang et al. [101], the impactor face struck the specimen normal to the skin surface. Since the model does not have skin, it is much harder to position the impactor accurately since the reference is the skull surface. Regarding the lower energy impact, a tiny fracture was predicted. A possible reason may be also related with the absence of scalp, so the impact is more concentrated on those

specific locations, and the first structure to absorb the impact energy and physically contact a striking object is the skull. This reason is very relevant since the study of Trotta et. al [114] showed that scalp tissue affects head impact biomechanics in a significant way, reducing the linear/rotational acceleration and in some cases causing an important change in the motion of the impact.

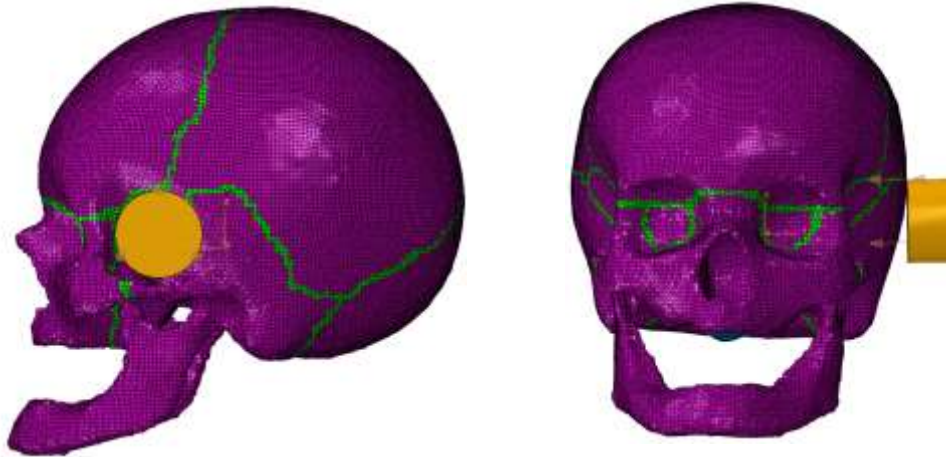
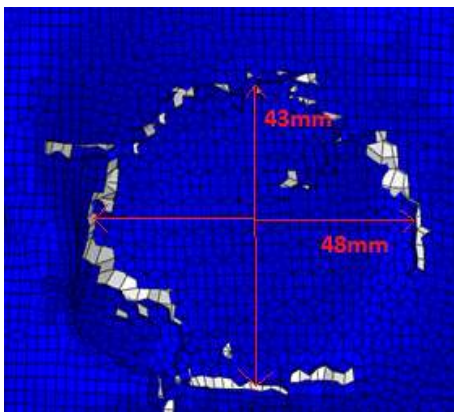
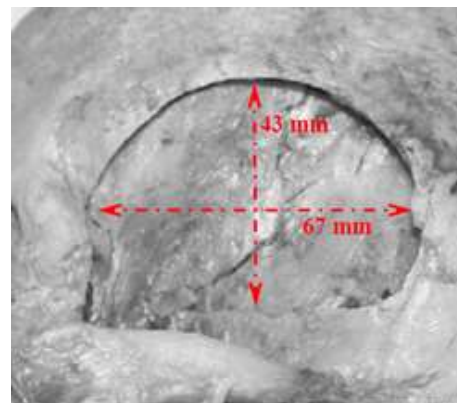


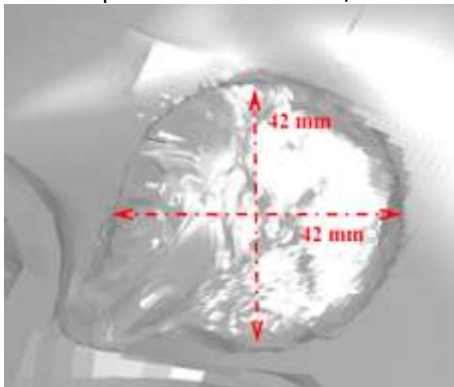
Figure 77. Huang's simulation assembly on Abaqus.



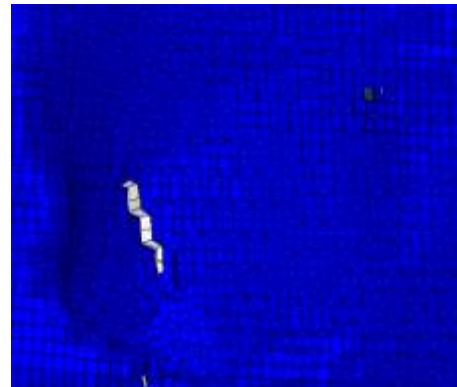
a) Fracture pattern from the 35 m/s simulation



b) Fracture pattern from Huang's 35m/s test



c) Fracture pattern from Huang's 35m/s simulation



d) Fracture pattern from the 20 m/s simulation

Figure 78. Comparisons of depressed skull fracture pattern obtained with YEAHM and in both Huang's experiment and simulation.

Chapter 5

Conclusions and Future Works

5.1 Conclusion

In this dissertation, a computational model of the skull of a 65-year-old human male was developed and incorporated in the YEAHM. Several stages of validation were performed, from local material validation to isolated skull blunt trauma and impacts at different velocities simulating falls. Accelerations, impact forces and fracture patterns are used to validate the skull model.

For this purpose, a study and understanding of the current literature regarding the properties of the head, but in more detail of the skull, was done. Which was observed that of the several geometric models already existing of the human skull, the one that best suited this dissertation would be a skull with differentiation between cortical, trabecular bone and cranial suture tissue, but more precisely, the creation of a model with the cortical bone tissue with a constant thickness of approximately 1.5 mm. It was also chosen to use C3D8R elements as the basis for the skull model since these elements benefit from achieving good simulation results without compromising too much the computation cost of those same simulations. In addition to the geometric model, a material model for cortical, trabecular bone and suture tissues was also developed and validated. From these 3 tissues, it was also created a damage model for both cortical bone and sutures.

5.1.1 Future Works

From the model developed in this dissertation and considering the conclusions described above, some suggestions for future work are here described. Firstly, in relation to works that would lead to the improvement of the version of the YEAHM improved in this work:

- Creation of the scalp to integrate in the YEAHM, since previously the scalp was shown to be an important part for head impact biomechanics.
- Subdivide the current CSF of the YEAHM model in all its constituent elements, mainly the meninges.

Secondly, since YEHAM represents the head of a 65-year-old man, it is suggested as future work:

- Creation of a model of a child's head, due to the occurrence of a great geometrical and material difference of the head according to age, that can predict impact-induced skull fracture in infants, just like the He's et al. [115] study.

References

- [1] WHO, "Road traffic injuries," 7 2 2020. [Online]. Available: <https://www.who.int/news-room/fact-sheets/detail/road-traffic-injuries>. [Accessed 12 6 2020].
- [2] eurostat, "Statistics Explained," 6 2018. [Online]. Available: https://ec.europa.eu/eurostat/statistics-explained/index.php?title=Accidents_at_work_statistics#Incidence_rates. [Accessed 2019 11 2].
- [3] F. Fernandes, D. Tchepel, R. Alves de Sousa and M. Ptak, "Development and validation of a new finite element human head model - YEt Another Head Model (YEAHM)," *Engineering Computations*, vol. 35, no. 1, pp. 477-496, 2018.
- [4] H. Mao, L. Zhang, B. Jiang, V. Genthikatti, X. Jin, F. Zhu, R. Makwana, A. Gill, G. Jandir, A. Singh and K. H. Yang, "Development of a Finite Element Human Head Model Partially Validated With Thirty Five Experimental Cases," *Journal of biomechanical engineering*, vol. 135, no. 11, pp. 111002.1-111002.15, 2013.
- [5] R. Drake, A. W. Vogl and A. W. Mitchell, *Gray's Anatomy for Students*, 2nd Edition, Philadelphia: Churchill Livingstone, 2010.
- [6] S. D. Team, "Meninges of the central nervous parts," 29 11 2015. [Online]. Available: <https://commons.wikimedia.org/wiki/File:Meninges-en.svg>. [Accessed 7 11 2019].
- [7] A. N. Bashkatov, E. A. Genina, Y. P. Sinichkin, V. I. Kochubey, N. A. Lakodina and V. V. Tuchin, "Glucose and Mannitol Diffusion in Human Dura Mater," *Biophysical Journal*, vol. 85, no. 5, p. 3310–3318, 2003.
- [8] K. Oka, A. L. Rhoton Jr, M. Barry and R. Rodriguez, "Microsurgical anatomy of the superficial veins of the cerebrum," *Neurosurgery*, vol. 17, no. 5, pp. 711-748, 1985.
- [9] C. Brockmann, S. Kunze and J. Scharf, "Computed tomographic angiography of the superior sagittal sinus and bridging veins," *Surgical and radiologic anatomy*, vol. 33, no. 2, pp. 129-134, 2011.
- [10] H. Han, W. Tao and M. Zhang, "The dural entrance of cerebral bridging veins into the superior sagittal sinus: an anatomical comparison between cadavers and digital subtraction angiography," *Neuroradiology*, vol. 49, no. 2, pp. 169-175, 2007.
- [11] J. G. Betts, K. A. Young, J. A. Wise, E. Johnson, B. Poe, D. H. Kruse, O. Korol, J. E. Johnson, M. Womble and P. DeSaix, *Anatomy and Physiology*, Houston, Texas: OpenStax, 2013.

- [12] K. S. Saladin, The brain and cranial nerves. In:Saladin, K. S. (Ed.) Human Anatomy. International Edition, New York: McGraw Hill Higher Education, 2007.
- [13] M. E. Bain, "Brain Anatomy and Function," 6 3 2019. [Online]. Available: <https://www.healthpages.org/anatomy-function/brain-anatomy/>. [Accessed 2019 11 7].
- [14] K. M. Tse, S. P. Lim, V. B. C. Tan and H. P. Lee, "A Review of Head Injury and Finite Element Head Models," *American Journal of Engineering, Technology and Society*, vol. 1, no. 5, pp. 28-52, 2014.
- [15] B. Endo, "A biomechanical study of the human facial skeleton by means of strain-sensitive lacquer," *Okajimas folia anatomica Japonica*, vol. 42, no. 4, pp. 205-217, 1966.
- [16] P. A. School, "The skull bones and features," [Online]. Available: <http://paletteartschool.com/tutorials/the-skull-bones-and-features/>. [Accessed 2019 11 7].
- [17] W. a. bee, "File:Facial skeleton - en.svg - Wikimedia Commons," 2 1 2015. [Online]. Available: https://commons.wikimedia.org/wiki/File:Facial_skeleton_-_en.svg. [Accessed 12 6 2020].
- [18] L. Zhang, K. Yang, R. Dwarampudi, K. Omori, T. Li, K. Chang, W. Hardy, T. Khalil and A. King, Recent Advances in Brain Injury Research: A New Human Head Model Development and Validation, San Antonio, Texas: SAE Technical Paper, 2001.
- [19] A. Maloul, Biomechanical Characterization of Complex Thin Bone structures in The Human Craniofacial Skeleton, Toronto: Institute of Biomaterials and Biomedical Engineering, University of Toronto, 2012, pp. 50-71.
- [20] B. w. site, "Human Anatomy and Physiology Lab (BSB 141)," [Online]. Available: <https://courses.lumenlearning.com/ap1x94x1/chapter/the-bones-of-the-skull/>. [Accessed 31 10 2019].
- [21] M. Ptak, M. Ratajczak, A. Kwiatkowski, M. Sawicki, J. Wilhelm, F. A. Fernandes and A. Druszcz, "Investigation of biomechanics of skull structures damages caused by dynamic loads," *Acta of bioengineering and biomechanics*, vol. 20, no. 4, pp. 143-150, 2018.
- [22] R. Delille, D. Lesueur, P. Potier, P. Drazetic and E. Markiewicz, "Experimental study of the bone behaviour of the human skull bone for the development of a physical head model," *International Journal of Crashworthiness*, vol. 12, no. 2, pp. 101-108, 2007.
- [23] M. T. Davis, A. M. Loyd, H.-y. H. Shen, M. H. Mulroy, R. W. Nightingale, B. S. Myers and C. D. Bass, "The mechanical and morphological properties of 6 year-old cranial bone," *Journal of biomechanics*, vol. 45, no. 15, pp. 2493-2498, 2012.

- [24] S. Herring and P. Ochareon, "Bone--special problems of the craniofacial region," *Orthodontics \& craniofacial research*, vol. 8, no. 3, pp. 174-182, 2005.
- [25] R. H. Khonsari, J. Olivier, P. Vigneaux, S. Sanchez, P. Tafforeau, P. E. Ahlberg, F. Di Rocco, D. Bresch, P. Corre, A. Ohazama and others, "A mathematical model for mechanotransduction at the early steps of suture formation," *Proceedings of the Royal Society B: Biological Sciences*, vol. 280, no. 1759, p. 20122670–20122670, 2013.
- [26] A. Malczyk, K. Bauer, C. Juhra and S. Schick, "Head injuries in bicyclists and associated crash characteristics," in *Internacional Research Council on Biomechanics of Injury* , 2014.
- [27] Z. Zhang and J. Yang, "Biomechanical dynamics of cranial sutures during simulated impulsive loading," *Applied bionics and biomechanics*, vol. 2015, no. 1, pp. 596843-596854, 2015.
- [28] J. E. Urban, S. Lynch, S. K. Lynch, A. A. Weaver and J. D. Stitzel, "Evaluation of skull cortical thickness changes with age and sex from computed tomography scans," *Journal of Bone and Mineral Research*, vol. 31, no. 2, pp. 299-307, 2016.
- [29] T. Matsumoto and H. Mihashi, "JCI-DFRCC summary report on DFRCC terminologies and application concepts," in *Proceedings of the JCI international workshop on ductile fiber reinforced cementitious composites*, Takayama, Citeseer, 2002, pp. 59-66.
- [30] J. A. Gould, *Fisioterapia na ortopedia e na medicina do esporte*, Manole, 1993.
- [31] G. Belingardi, G. Chiandussi and I. Gaviglio, "Development and validation of a new finite element model of human head," in *Proc. 19th International Technical Conference of the Enhanced Safety of Vehicle*, Washington DC, Politecnico di Torino, Dipartimento di Meccanica, 2005, pp. 441-450.
- [32] Z. Asgharpour, D. Baumgartner, R. Willinger, M. Graw and S. Peldschus, "The validation and application of a finite element human head model for frontal skull fracture analysis," *Journal of the mechanical behavior of biomedical materials*, vol. 33, no. 1, pp. 16-23, 2014.
- [33] R. Willinger and D. Baumgartner, "Human head tolerance limits to specific injury mechanisms," *International journal of crashworthiness*, vol. 8, no. 6, pp. 605-617, 2003.
- [34] Z. Cai, Y. Xia, Z. Bao and H. Mao, "Creating a human head finite element model using a multi-block approach for predicting skull response and brain pressure," *Computer methods in biomechanics and biomedical engineering*, vol. 22, no. 2, pp. 169-179, 2019.
- [35] C. Deck and R. Willinger, "Added Value of Tissue Level Brain Injury Criteria," *International Journal of Automotive Engineering*, vol. 10, no. 2, pp. 191-196, 2019.

- [36] J. Chamrad, P. Marcián and L. Borák, "On the level of computational model of a human skull: A comparative study," *Applied and Computational Mechanics*, vol. 12, no. 1, pp. 5-16, 2018.
- [37] N. Lynnerup, J. G. Astrup and B. Sejrsen, "Thickness of the human cranial diploe in relation to age, sex and general body build," *Head & Face Medicine*, vol. 1, no. 1, p. 13, 2005.
- [38] N. Fenton and M. Neil, Risk assessment and decision analysis with Bayesian networks, Boca Raton: Crc Press, 2012.
- [39] A. Post and T. B. Hoshizaki, "Mechanisms of brain impact injuries and their prediction: a review," *Trauma*, vol. 14, no. 4, pp. 327-349, 2012.
- [40] K. Schmitt, P. Niederer, M. Muser and F. Walz, Trauma Biomechanics - An Introduction to Injury Biomechanics, Zurich: Springer, 2007.
- [41] R. P. Granacher Jr, Traumatic brain injury: Methods for clinical and forensic neuropsychiatric assessment, Boca Raton: CRC Press, 2008.
- [42] A. Mendelow, G. Teasdale, B. Jennett, J. Bryden, C. Hessett and G. Murray, "Risks of intracranial haematoma in head injured adults," *British medical journal*, vol. 287, no. 6400, pp. 1173-1176, 1983.
- [43] "physio4fight," 25 Julho 2016. [Online]. Available: <https://physio4fight.wordpress.com/2016/07/25/skull-fractures-in-in-martial-arts-mma-cyborg-santos-fractured-skull-at-bellator-158/>. [Accessed 17 10 2019].
- [44] B. Chinn and D. Hynd, "Technical response to the unpublished paper Critical Evaluation of the SHARP Motorcycle Helmet Rating'by NJ Mills," TRL, UK, 2009.
- [45] M. Aare, "Prevention of Head Injuries-focusing Specifically on Oblique Impacts," Royal Institute of Technology, Stockholm, 2003.
- [46] D. Graham, J. H. Adams, J. Nicoll, W. Maxwell and T. Gennarelli, "The nature, distribution and causes of traumatic brain injury," *Brain Pathology*, vol. 5, no. 4, pp. 397-406, 1995.
- [47] N. Besenski, "Imaging of head injuries," *Emergency Radiology: Imaging and Intervention*, pp. 99-124, 2006.
- [48] T. A. Gennarelli, "The state of the art of head injury biomechanics: A review," in *Proceedings of 29th Conference of the Association for the Advancement of Automotive Medicine*, Philadelphia, Association for the Advancement of Automotive Medicine, 1985, pp. 447-463.

- [49] A. K. Ommaya and T. Gennarelli, "Cerebral concussion and traumatic unconsciousness: correlation of experimental and clinical observations on blunt head injuries," *Brain*, vol. 97, no. 4, pp. 633-654, 1974.
- [50] S. Kleiven, "Finite element modeling of the human head," Royal Institute of Technology, Stockholm, 2002.
- [51] J. G. Greenfield, *Greenfield's neuropathology*, Great Britain: Hodder Arnold, 2008.
- [52] C. Porth and G. Matfin, *Pathophysiology: concepts of altered health states*. Number 8, China: Wolters Kluwer Health, 2009.
- [53] S. Kleiven, P. M. Peloso and H. Holst, "The epidemiology of head injuries in Sweden from 1987 to 2000," *Injury control and safety promotion*, vol. 10, no. 3, pp. 173-180, 2003.
- [54] D. H. Smith and D. F. Meaney, "Axonal damage in traumatic brain injury," *The Neuroscientist*, vol. 6, no. 6, pp. 483-495, 2000.
- [55] M. Oehmichen, R. N. Auer and H. G. König, *Forensic neuropathology and associated neurology*, Germany: Springer Science, 2006.
- [56] C. W. Gadd, "Use of a weighted-impulse criterion for estimating injury hazard," in *Proceedings of 10th Stapp Car*, New York, SAE Technical Paper, 1966, pp. 164-174.
- [57] J. Versac, "A review of severity of index," in *Proceedings of 15th Stapp Car Crash Conference*, Warrendale, Society of Automotive, 1971, pp. 771-796.
- [58] W. Goldsmith, "Current controversies in the stipulation," *Journal of Biomechanics*, vol. 14, no. 12, pp. 883-884, 1981.
- [59] L. Zhang, K. .. Yang and A. I. King, "A proposed," *Journal of Biomechanical Engineering*, vol. 126, no. 2, pp. 226-236, 2004.
- [60] C. Simms and D. Wood, "Injury mechanisms and injury criteria," in *Pedestrian and Cyclist Impact Mechanics*, Netherlands, Springer, 2009, pp. 75-97.
- [61] J. A. Newman, "A generalized acceleration model for brain injury threshold (GAMBIT)," in *Proceedings of International IRCOBI Conference on the Biomechanics of Impacts*, Zurich, Switzerland, 1986, pp. 121-131.
- [62] J. A. Newman, N. Shewchenko and E. Welbourne, "A proposed new biomechanical head injury assessment function - the maximum power index," in *44th Stapp Car Crash Conference*, Atlanta, 2000.

- [63] J. McElhaney, J. Fogle, J. Melvin, R. Haynes, V. Roberts and N. Alem, "Mechanical properties of cranial bone," *Journal of biomechanics*, vol. 3, no. 5, pp. 495-511, 1970.
- [64] A. Schaller, C. Voigt, H. Humpfner-Hierl, A. Hemprich and T. Hierl, "Transient finite element analysis of a traumatic fracture of the zygomatic bone caused by a head collision," *International journal of oral and maxillofacial surgery*, vol. 41, no. 1, pp. 66-73, 2012.
- [65] C. Got, A. Patel, A. Fayon, C. Tarriere and G. Walfisch, "Results of experimental head impacts on cadavers: the various data obtained and their relations to some measured physical parameters," SAE, 1978.
- [66] E. Gurdjian and J. Webster, *Head injuries; mechanisms, diagnosis and management*, Little Brown, 1958.
- [67] N. Yoganandan, F. Pintar, A. Sances JR, P. Walsh, C. Ewing, D. Thomas and R. Snyder, "Biomechanics of skull fracture," *Journal of neurotrauma*, vol. 12, no. 4, pp. 659-668, 1995.
- [68] D. Baumgartner and R. Willinger, "Numerical Modeling of the Human Head under Impact: New Injury Mechanisms and Tolerance Limits," in *IUTAM Symposium on Impact Biomechanics: From Fundamental Insights to Applications*, Netherlands, Springer, 2005, pp. 195-203.
- [69] A. M. Nahum, J. D. Gatts, C. W. Gadd and J. Danforth, *Impact tolerance of the skull and face*, SAE Technical Paper, 1968.
- [70] V. Hodgson and L. Thomas, Hodgson, V. R., & Thomas, L. M. (1971). Comparison of head acceleration injury indices in cadaver skull fracture, SAE , 1971.
- [71] S. Advani, W. Powell, J. Huston and S. Ojala, "Human head impact response experimental data and analytical simulations," in *Proc. Intern. Conf. on Biomechanics of Serious Trauma*, West Virginia, Department of Mechanical Engineering and Mechanics, West Virginia University, 1975, pp. 153-162.
- [72] D. Allsop, C. Warner, M. Wille, D. Schneider and A. Nahum, *Facial impact response-a comparison of the Hybrid III dummy and human cadaver*, San Diego: Stapp, 1998.
- [73] D. Schneider and A. Nahum, "Impact studies of facial bones and skull," in *16th Stapp Car Crash Conference*, 1972.
- [74] D. Allsop, T. Perl and C. Warner, *Force/deflection and fracture characteristics of the temporo-parietal region of the human head*, SAE, 1991.
- [75] S. Advani, A. Ommaya and W. Yang, *Head injury mechanisms*, Oxford: Oxford University Press, 1882.

- [76] R. P. Hubbard, "Flexure of layered cranial bone," *Journal of Biomechanics*, vol. 4, no. 4, pp. 251-263, 1971.
- [77] Z. Li, X. Luo and J. Zhang, "Development/global validation of a 6-month-old pediatric head finite element model and application in investigation of drop-induced infant head injury," *Computer methods and programs in biomedicine*, vol. 112, no. 3, pp. 309-319, 2013.
- [78] C. H. Hardy and P. V. Marcal, "Elastic analysis of a skull," *Journal of Applied Mechanics*, vol. 40, no. 4, pp. 838-842, 1973.
- [79] T. Shugar, Transient structural response of the linear skull-brain system, SAE Technical Paper, 1975.
- [80] V. H. Kenner and W. Goldsmith, "Dynamic loading of a fluid-filled spherical shell," *International Journal of Mechanical Sciences*, vol. 14, no. 9, pp. 557-568, 1972.
- [81] T. B. Khalil and R. P. Hubbard, "Parametric study of head response by finite element modeling," *Journal of Biomechanics*, vol. 10, no. 2, pp. 119-132, 1977.
- [82] H. S. Chan, "Mathematical model for closed head impact," SAE Technical Paper, 1974.
- [83] R. Hosey, "A homeomorphic finite element model of the human head and neck," in *Finite elements in biomechanics*, John Wiley & Sons, 1982.
- [84] J. J. Yang, . J. Dai and Z. Zhuang, "Human head modeling and personal head protective equipment: A literature review," in *International Conference on Digital Human Modeling*, Berlin, Springer, 2009, pp. 661-670.
- [85] J. S. Ruan, T. B. Khalil and A. King, "Finite element modeling of direct head impact," in *Proceedings of 37th Stapp Car Crash Conference*, San Antonio, 1993.
- [86] C. Zhou, T. B. Khalil and A. King, "A new model comparing impact responses of the homogeneous and inhomogeneous human brain," in *Proceedings of 39th Stapp Car Crash Conference*, San Diego, 1995.
- [87] L. Zhang, K. H. Yang, R. Dwarampudi, K. Omori, T. Li, K. Chang, W. N. Hardy, T. B. Khalil and A. I. King, "Recent advances in brain injury research: a new human head model development and validation," in *Proceedings of 45th Stapp Car Crash Conference*, San Antonio, 2001.
- [88] A. I. King, K. H. Yang, L. Zhang, W. Hardy and D. C. Viano, "Is head injury caused by linear or angular acceleration?," in *Proceedings of International IRCOBI Conference on the Biomechanics of Impacts*, Lisbon, Portugal, 2003.

- [89] R. Willinger, H.-S. Kang and B. Diaw, "Three-dimensional human head finite-element model validation against two experimental impacts," *Annals of biomedical engineering*, vol. 27, no. 3, pp. 403-410, 1999.
- [90] A. M. Nahum, R. Smith and C. C. Ward, "Intracranial pressure dynamics during head impact," SAE Technical Paper, 1977.
- [91] X. Trosseille, C. Tarriere, F. Lavaste, F. Guillon and A. Domont, "Development of a FEM of the human head according to a specific test protocol," *36th Stapp Car Crash*, pp. 235-253, 1992.
- [92] P. Verschueren, H. Delye, B. Depreitere, C. Van Lierde, B. Haex, D. Berckmans, I. Verpoest, J. Goffin, J. Vander Sloten and G. Van der Perre, "A new test set-up for skull fracture characterisation," *Journal of biomechanics*, vol. 40, no. 15, pp. 3389-3396, 2007.
- [93] D. Marjoux, D. Baumgartner, C. Deck and R. Willinger, "Head injury prediction capability of the HIC, HIP, SIMon and ULP criteria," *Accident Analysis & Prevention*, vol. 40, no. 3, pp. 1135-1148, 2008.
- [94] S. Kleiven and W. N. Hardy, "Correlation of an FE model of the human head with local brain motion-consequences for injury prediction," in *Proceedings of 46th Stapp Car Crash Conference*, Ponte Vedra, USA, 2002.
- [95] K. Mendis, R. Stalnaker and S. Advani, "A constitutive relationship for large deformation finite element modeling of brain tissue," *Journal of Biomechanical Engineering*, vol. 117, no. 3, pp. 279-285, 1995.
- [96] E. G. Takhounts, R. H. Eppinger, J. Q. Campbell, R. E. Tannous, E. D. Power and L. S. Shook, "On the development of the SIMon finite element head model," in *Proceedings of 47th Stapp Car Crash Conference*, San Diego, USA, 2003.
- [97] T. J. Horgan and M. D. Gilchrist, "The creation of three-dimensional finite element models for simulating head impact biomechanics," *International Journal of Crashworthiness*, vol. 8, no. 4, pp. 353-366, 2003.
- [98] N. Yoganandan, D. J. Maiman, F. Pintar, G. Ray, J. B. Myklebust, A. Sances Jr and S. J. Larson, "Microtrauma in the lumbar spine: a cause of low back pain," *Neurosurgery*, vol. 23, no. 2, pp. 162-168, 1988.
- [99] E. Wang, T. Nelson and R. Rauch, "Back to elements-tetrahedra vs. hexahedra," in *Proceedings of the 2004 international ANSYS conference*, 2004.
- [100] S. Tadepalli, A. Erdemir and P. R. Cavanagh, "Comparison of hexahedral and tetrahedral elements in finite element analysis of the foot and footwear," *Journal of biomechanics*, vol. 44, no. 12, pp. 2337-2343, 2011.

- [101] J. Huang, D. Raymond, W. Shen, J. Stuhmiller, G. Crawford and C. Bir, "Development and Validation of a Subject-Specific Finite Element Model for Skull Fracture Assessment," in *ASME 2011 International Mechanical Engineering Congress and Exposition*, Colorado, American Society of Mechanical Engineers Digital Collection, 2011, pp. 31-40.
- [102] H. Delye, P. Verschuere, B. Depraetere, I. Verpoest, D. Berckmans, J. Vander Sloten, G. Van Der Perre and J. Goffin, "Biomechanics of frontal skull fracture," *Journal of Neurotrauma*, vol. 24, no. 10, pp. 1576-1586, 2007.
- [103] G. F. d. J. Migueis, *Simulação numérica da ocorrência de hematomas*, Aveiro: Universidade de Aveiro, Departamento de Mecânica, 2018.
- [104] J. M. C. Costa, *Desenvolvimento de um modelo pormenorizado*, Aveiro: Universidade de Aveiro, Departamento de Mecânica, 2019.
- [105] F. Fernandes, *Análise biomecânica de impactos com capacetes: Novos materiais e geometrias*. Tese de Doutoramento, Aveiro, Portugal: Universidade de Aveiro, 2017.
- [106] P. Cignoni, M. Callieri, M. Corsini, M. Dellepiane, F. Ganovelli and G. Ranzuglia, "MeshLab: an Open-Source Mesh Processing Tool," in *Eurographics Italian Chapter Conference*, The Eurographics Association, 2008, pp. 129-136.
- [107] W. Nowinski, B. Chua, T. Thaug and S. Wut Yi, "The human brain, head and neck in 2953 pieces," Thieme, New York, 2015.
- [108] S. Boruah, K. Henderson, D. Subit, R. S. Salzar, B. S. Shender and G. Paskoff, "Response of human skull bone to dynamic compressive loading," in *Proceedings of the IRCOBI Conference*, Internacional Research Council on Biomechanics of Injury, 2013, p. 497.
- [109] N. Yoganandan, J. Zhang and F. A. Pintar, "Force and acceleration corridors from lateral head impact," *Traffic injury prevention*, vol. 5, no. 4, pp. 368-373, 2004.
- [110] R. Ankit, "WebPlotDigitizer," Abril 2019. [Online]. Available: <https://automeris.io/WebPlotDigitizer>. [Accessed Agosto 2019].
- [111] M. Vander Vorst, P. Chan, J. Zhang, N. Yoganandan and F. Pintar, "A new biomechanically-based criterion for lateral skull fracture," in *Annual Proceedings/Association for the Advancement of Automotive Medicine*, Wisconsin, Association for the Advancement of Automotive Medicine, 2004, p. 181.
- [112] M. ElGawady, A. J. Booker and H. M. Dawood, "Seismic behavior of posttensioned concrete-filled fiber tubes," *Journal of Composites for Construction*, vol. 14, no. 5, pp. 616-628, 2010.

- [113] D. Sahoo, C. Deck, N. Yoganandan and R. Willinger, "Anisotropic composite human skull model and skull fracture validation against temporo-parietal skull fracture," *Journal of the mechanical behavior of biomedical materials*, vol. 28, no. 1, pp. 340-353, 2013.
- [114] A. Trotta, D. Zouzias, G. De Bruyne and A. N. Annaidh, "The importance of the scalp in head impact kinematics," *Annals of biomedical engineering*, vol. 46, no. 6, pp. 831-840, 2018.
- [115] J. He, J. Yan, S. Margulies, B. Coats and A. D. Spear, "An adaptive-remeshing framework to predict impact-induced skull fracture in infants," *Biomechanics and Modeling in Mechanobiology*, vol. 1, no. 1, pp. 1-11, 2020.